TESIS DE LA UNIVERSIDAD
DE ZARAGOZA

2015

7

Luca Bergamasco

Multi-scale modeling of complex fluids and deformable fibrous media for liquid composite molding

Departamento

Ciencia y Tecnología de Materiales y Fluidos

Director/es

Izquierdo Estallo, Salvador
Fueyo Díaz, Norberto

ISSN 2254-7606

Prensas de la Universidad
Universidad Zaragoza

Tesis Doctoral

MULTI-SCALE MODELING OF COMPLEX FLUIDS AND DEFORMABLE FIBROUS MEDIA FOR LIQUID COMPOSITE MOLDING

Autor

Luca Bergamasco

Director/es

Izquierdo Estallo, Salvador
Fueyo Díaz, Norberto

UNIVERSIDAD DE ZARAGOZA
Ciencia y Tecnología de Materiales y Fluidos

2014

MULTI-SCALE MODELING OF COMPLEX FLUIDS AND DEFORMABLE FIBROUS MEDIA FOR LIQUID COMPOSITE MOLDING

Luca Bergamasco
Department of Science and Technology of Materials and Fluids
University of Zaragoza

A thesis submitted in partial fulfillment for the degree of
Doctor of Philosophy
JUNE 2014

This work has been carried out at **ITA**INNOVA - Instituto Tecnológico de Aragón

ACKNOWLEDGMENTS

This work has been made possible thanks to the financial support provided by the European Social Fund, the Spanish Ministry of Economy and Competitiveness and the Government of Aragon. Part of the experimental data used in this thesis were obtained thanks to the collaboration of Aernnova and Aeroblade.

Author
Luca Bergamasco

Thesis title
Multi-scale modeling of complex fluids and deformable fibrous media
for liquid composite molding

Thesis advisor
Dr. Salvador Izquierdo
División de Materiales y Componentes
ITAINNOVA - Instituto Tecnológico de Aragón

Thesis co-advisor
Prof. Norberto Fueyo
Grupo de Fluidodinámica Numérica (GFN)
Dpto. de Ciencia y Tecnología de Materiales y Fluidos
Universidad de Zaragoza

Abstract

In the last few years, the interest of the aerial and terrestrial transport industry in the fabrication of textile-reinforced composite materials has sensibly grown. This is basically due to the remarkable properties of these materials, which combine high mechanical strength with reduced weight. The manufacturing techniques that provide better control on the final quality of the components rely on autoclave curing: heat and pressure are applied on vacuum bags to achieve high volume fractions of the reinforcement and low number of defects due to the presence of voids. Nevertheless, autoclave curing implies high costs for the acquisition of the vessel and the process is energy and time consuming.

To reduce the production costs, the industry has increased its interest in out-of-autoclave processing technologies, that is, *liquid composite molding* (LCM) techniques. In its most basic version, the technique consists in the injection of a catalyzed resin into a closed cavity, where a pre-placed fiber stack lies. When the resin has completely permeated the preform, the mold is subject to high temperatures to induce the curing of the resin to obtain the composite. The current challenge for this technology is to achieve the same quality standards for the final component as those achievable with in-autoclave processing.

In LCM processes, the final quality of the component depends on several factors, such as: the structure of the textile, the arrangement of the layers, the adaption to the mold, the compaction process, the operating conditions, the geometry of the component, the configuration of the injection points for the resin, the physical and chemical interactions between the resin and the textile. All these factors affect the correct saturation of the reinforcement, and therefore process parameters must be adequately controlled in order to guarantee the required quality standards for the composite.

In this sense, mold filling simulation software is a valuable tool for the process optimization; however the permeability of the reinforcement is required as an input parameter. An accurate evaluation of the permeability of the reinforcement however, represents a challenging task. Fibrous preforms for LCM generally present a hierarchical structure: the fibers are bunched in yarns, which in turn are bundled in a fabric. This structure, undergoes complex deformations during the production process: 1) during the compaction in the mold and 2) during the injection of the resin. This issue remarkably complicates an accurate evaluation of the permeability of the reinforcement and may be at the origin of the scatter observed in the experimental measurements.

From a modeling point of view, the different length scales to be taken into account (typically ranging between one and three orders of magnitude) hinders a proper simulation of the deformation of the textile. The typical diameter of the fibers ranges indeed in few micrometers, while the characteristic dimension of the yarns is in the order of the millimeter. This issue represents a constraint for standard numerical approaches due to computational limits. In order to account for the effect on the permeability of the deformation of the hierarchical structure of the preform, multi-scale modeling techniques must be adopted.

The objective of the thesis is the development of novel theoretical and numerical frameworks to account for the effect on the permeability of the multi-scale deformations that the textile undergoes during the two aforementioned stages of the process. The development focuses on the fiber-yarn level in 2D, where the yarn is always modeled as suspension of fibers by analogy with a complex fluid. The numerical implementations use computational fluid dynamic (CFD) tools.

In order to address the problem, the permeability of a textile preform for LCM is first analyzed by experimental means. A standard CFD approach is then adopted for the simulation of a representative elementary volume of the textile; it is shown that, by means of this approach, the experimental permeability cannot be recovered over the full range of porosities. An X-ray computed microtomography of the textile is then performed. The obtained data are used for the virtual reconstruction of the exact geometry of the textile after its use for LCM. The simulations with this latter geometry provide better results; however the uncertainties on permeability still hold, and the permeability is always overestimated. These uncertainties are discussed in detail and motivate the work described hereafter.

The first modeling block of the thesis concerns the analysis of the deformation that the textiles undergo during the compaction in the mold. A continuum model is first developed and validated for the squeeze flow of epoxy-based materials, the rheology of which is given by a viscoplastic constitutive law. The model is then applied to the compaction of yarns, where a viscoplastic behavior for the fiber bundle is assumed in the quasi-static regime of compression and by an analogy with flowing granular media. The rheological parameters are obtained from experimental data by a simplified analytical model for the deformation of the yarns under compaction. The commercial CFD code ANSYS Fluent is adopted for the numerical solution. The model yields information about the evolution of the fiber volume fraction during the compaction and is found to correctly recover the experimental force for high compression ratios.

The second modeling block of the thesis concerns the analysis of the deformation that the textiles undergo during the injection of the resin. A numerical framework is first developed and validated for the direct numerical simulation of dilute colloidal suspensions of polymeric molecules. The numerical method consists in a coupled finite-volume/lattice-Boltzmann solution: finite volume method for hydrodynamics and lattice Boltzmann method for the subgrid-scale physics. For computational efficiency, the lattice Boltzmann solution is accelerated on a graphic processing unit (GPGPU) with a tailored implementation and efficiently coupled with the macroscopic solver (ANSYS Fluent). The numerical method is then exploited for the solution of a mesoscopic model for the flow-induced fiber dynamics during the injection. A statistical model for the fiber dynamics is derived, based on analogy of the yarn with a non-Brownian suspension of particles with confining potentials. The fiber topology during the injection is recovered by a topological invariant and yields information about the change in permeability due to the clustering of fibers in steady-state, fully-saturated conditions. The results are presented in the form of phase diagrams, which show that in the deformable case the permeability can be up to one order of magnitude lower than in the rigid case.

On the basis of the results obtained, the following main conclusions can be drawn:

1. The model developed for the compaction in the mold showed to be appropriate for a phenomenological analysis of the deformation of the yarns under compression. The model allows to analyze quantitatively the evolution of the fiber volume fraction, which yields useful information for a better understanding of the distribution of the fibers before the injection.
2. The model developed for the fiber dynamics during the injection, allows to analyze their topology induced by the fluid flow. The clustering of fibers significantly reduces the permeability at the fiber level, which could explain the overestimation obtained with simplified numerical approaches. The phase diagrams obtained for the permeability, both at the yarn and fiber level, allow to identify the best operating conditions for the infiltration of the resin.

The proposed models have been developed using fluid dynamic techniques, which opens the possibility for a unified framework for the analysis, and ultimately, for a more precise estimation of the permeability. This work aims to represent a first tentative in this direction.

Resumen

En la industria aeronáutica, los materiales compuestos de matriz polimérica y refuerzo en fibra de vidrio se emplean cada vez más en aplicaciones estructurales debido a sus excepcionales propiedades, que combinan una alta resistencia mecánica con un peso reducido. Las técnicas de fabricación que permiten un mejor control de la calidad final de las piezas emplean curado dentro de autoclave: se aplica calor y presión en sacos a vacío, permitiendo la fabricación de componentes con altas fracciones volumétricas de fibra y bajo contenido de defectos por presencia de huecos de aire. Sin embargo, el uso de autoclave implica unos altos costes de adquisición, un uso intensivo de energía en operación y largos tiempos de proceso.

En un esfuerzo por reducir los costes de fabricación, la industria ha aumentado su interés en las tecnologías de procesado fuera de autoclave, es decir el *liquid composite molding* (LCM). En su versión más básica, estas técnicas consisten en la inyección de una resina catalizada en una cavidad cerrada, donde se encuentran las telas previamente situadas. En este proceso, una vez que la resina ha permeado completamente la tela, es elevada la temperatura del molde con el objetivo de inducir la solidificación de dicha resina y obtener el material compuesto. El reto actual para la aplicación de esta tecnología es conseguir el mismo nivel de calidad que se consigue en un proceso con autoclave.

En procesos LCM, la calidad final del componente depende de factores como: la estructura de la tela, la disposición de las capas de refuerzo, su adaptación al molde, el proceso de compactación, las condiciones operativas, la geometría del componente, la configuración de los puntos de inyección de la resina, las interacciones físicas y químicas entre la resina y la tela. Todos estos factores influyen sobre la correcta saturación del refuerzo, por lo que los parámetros del proceso deben ser adecuadamente controlados a fin de garantizar la calidad del producto final.

En este sentido, los programas de simulación constituyen herramientas valiosas para la optimización del proceso de llenado del molde, sin embargo, éstos requieren la permeabilidad del refuerzo como parámetro de entrada. Una evaluación precisa de la permeabilidad del refuerzo representa un reto no trivial. De hecho, las telas de refuerzo para LCM generalmente presentan una estructura jerárquica: las fibras se agrupan en hebras y estas a su vez se entrelazan en tejidos. Esta estructura experimenta dos tipos de deformaciones complejas durante del proceso productivo: 1) durante la compactación en el molde y 2) durante la inyección de la resina. Esto impide una evaluación precisa de la permeabilidad del refuerzo y puede ser el origen de la dispersión que se observa en las medidas experimentales.

Desde el punto de vista del modelado, las diferentes escalas de longitud que hay que tener en cuenta (típicamente varían entre uno y tres órdenes de magnitud) hacen difícil la simulación del proceso de deformación de la tela. De hecho, el diámetro típico de las fibras es generalmente de unas pocas micras, mientras que la dimensión característica de las hebras llega ser del orden de milímetros. Esta cuestión constituye un handicap para enfoques estándar de simulación debido a límites computacionales. Para analizar adecuadamente la influencia de la deformación de la estructura jerárquica de la tela sobre la permeabilidad, deben adoptarse técnicas de modelado multi-escala.

El objetivo de esta tesis es el desarrollo de nuevos modelos teóricos y numéricos que tengan en cuenta el efecto sobre la permeabilidad de las deformaciones multi-escala que las telas experimentan durante las dos fases del proceso previamente mencionadas. Para lograrlo, la metodología empleada se centra en secciones representativas 2D de las hebras, las cuales se modelan desde el punto de vista fenomenológico como una suspensión de fibras, por analogía a un fluido complejo. Para la implementación de las simulaciones se utilizan herramientas de fluidodinámica computacional.

Para desarrollar esta metodología, inicialmente se analiza la permeabilidad de una tela para LCM a través de medios experimentales. Posteriormente, se adopta un enfoque estándar para la simulación de un volumen representativo de la tela, el cual muestra que la permeabilidad experimental no se puede ajustar en todo el rango de porosidades. Se efectúa entonces una micro-tomografía de rayos X. Los datos proporcionados por la tomografía son utilizados para la reconstrucción virtual de la geometría exacta de la tela después de su uso en un proceso LCM. Las simulaciones con esta última geometría proporcionan mejores resultados, aunque permanecen incertidumbres sobre la permeabilidad, la cual siempre se sobrestima. Dichas incertidumbres se discuten en detalle y motivan el trabajo descrito a en el resto de la tesis.

En un primer bloque de modelado se analiza la deformación de las telas durante la compactación en el molde. Se desarrolla y valida un modelo continuo para la compactación de materiales epoxy, cuya reología se describe a través de una ley constitutiva viscoplástica. Este modelo se aplica luego al estudio de la compactación de las hebras, donde se asume un comportamiento de tipo viscoplástico para las hebras en el régimen quasi-estático, por analogía con medios granulares. Los parámetros reológicos se obtienen a partir de los datos experimentales a través de un modelo analítico simplificado para la deformación de las hebras durante la compactación. Para las soluciones numéricas, se adopta el código comercial de fluidodinámica computacional ANSYS Fluent. El modelo proporciona información cuantitativa sobre la evolución de la fracción de volumen de fibra durante la compactación y se demuestra capaz de recuperar correctamente la fuerza experimental en el régimen de altos ratios de compresión.

En el segundo bloque se analiza la deformación de las telas durante la inyección de resina. En este bloque inicialmente se desarrolla y valida un método numérico para la simulación directa de suspensiones coloidales diluidas de moléculas poliméricas. Dicho método numérico consiste en una solución acoplada de volúmenes-finitos/lattice-Boltzmann: el método de volmenes finitos para la hidrodinámica y el método de lattice Boltzmann para la física de sub-malla. Por eficiencia computacional, la solución de lattice Boltzmann se acelera en tarjeta grafica (GPGPU) a través de una implementación adaptada y se acopla eficientemente con el solver macroscópico (ANSYS Fluent). Posteriormente, el método numérico desarrollado se aplica a la solución de un modelo mesoscópico para la dinámica de las fibras inducida por el flujo fluido durante la inyección. Se deriva un modelo estadístico para la dinámica de las fibras, basado en la analogía entre la hebra y una suspensión no Browniana de partículas con potenciales de confinamiento. La topología de las fibras durante de la inyección se recupera a través de un invariante topológico y proporciona informaciones sobre la variación de la permeabilidad debido al agrupamiento de las fibras en condiciones estacionarias y completamente saturadas. Los resultados se presentan en forma de diagramas de fase, los cuales muestran que la permeabilidad puede llegar a ser en el caso deformable hasta un orden de magnitud menor con respecto al caso rígido.

Como conclusiones principales del trabajo se plantea que:

1. el modelo desarrollado para la compactación en el molde resulta apto para un estudio fenomenológico de la deformación de las hebras bajo compactación. Dicho modelo permite analizar cuantitativamente la evolución de la fracción de fibra, lo cual proporciona información útil para la mejora de la comprensión de la distribución de las fibras antes de la inyección de la resina.
2. el modelo desarrollado para la dinámica de las fibras durante la inyección, permite analizar la topología de las mismas inducida por el flujo. El agrupamiento de fibras reduce significativamente la permeabilidad a nivel de hebra, y esto podría explicar la sobrestimación que se obtiene con modelos numericos simplificados. Los diagramas de fase obtenidos para la permeabilidad, tanto a nivel de fibra como de hebra, permiten identificar las mejores condiciones operativas para la infiltración de la resina.

Los modelos propuestos han sido desarrollados usando técnicas de fluidodinámica computacional, lo cual permitiría en un futuro utilizar entornos unificados para el análisis del proceso y finalmente, una estimación más precisa de la permeabilidad. El actual trabajo constituye así una primera aproximación en esta dirección.

Acknowledgements

A popular quote on life states that we should enjoy the journey, more than the arrival. Only now I realize that sometimes we are just too focused on our goal, to enjoy the journey, and that the end of a chapter is just the beginning of a new one. As Sydney J. Harris said, "happiness is a direction, not a place". However, here is my arrival, and I feel indebted with a number of persons who made this result possible.

First of all, I would like to acknowledge ITAINNOVA and in particular Dr. Miguel Ángel Jimenéz, for giving me the possibility of this experience in Spain. Similarly, I sincerely thank my thesis advisors, Dr. Salvador Izquierdo and Prof. Norberto Fueyo, for their guidance and for encouraging this work. I am sincerely grateful to Prof. Ignacio Pagonabarraga (Universitat de Barcelona) and Prof. Amine Ammar (Arts et Métiers ParisTech Angers), for fruitful discussions. Thanks to Prof. Pietro Asinari (Politecnico di Torino), for encouraging me to go for a PhD. Now I am definitely convinced I made the right choice.

During these years, several persons contributed to enrich this experience, to them I am particularly grateful. Thanks to Juan José, my historical flat mate, for sharing with me pros and cons of the PhD and everyday life. Thanks to Pedro, for his willingness in rigorously teaching me Spanish and the basics of philosophy. Thanks to María, Eduardo, Luis, Andrea and Alba. Finally, of course, thanks to my longtime friends, in particular Paolo and Marco, who have always been with me, despite the physical distance.

Lastly, yet more importantly, I would like to acknowledge my family: my father Francesco, my mother Patrizia and my sister Greta. They unconditionally supported and encouraged me in every choice, always. Finally, thanks to Margherita, for being part of my life.

Thank you all,
Luca

"Limits exist only in the minds of those who are short of dreams"
Philippe Petit - Traité du funambulisme, 1997

To my sister,
Greta

Contents

Abstract iii

Resumen (Español) vii

List of Figures xvii

List of Tables xxi

Nomenclature xxvi

1 Introduction 1
- 1.1 Motivation . . . 1
- 1.2 Objectives . . . 5
- 1.3 Methodology . . . 6
- 1.4 Thesis overview . . . 9

2 Permeability of textile reinforcements 10
- 2.1 Introduction . . . 10
- 2.2 Experimental data . . . 11
  - 2.2.1 Permeabilities . . . 11
  - 2.2.2 SEM image analysis . . . 12
  - 2.2.3 CMT data analysis . . . 14
- 2.3 Standard CFD approach . . . 15
  - 2.3.1 Representative geometry . . . 15
  - 2.3.2 CMT reconstructed geometry . . . 15
  - 2.3.3 Numerical solution . . . 16
  - 2.3.4 Results and discussion . . . 18
- 2.4 Summary and outlook . . . 22

3 Compression of viscoplastic soft solids 23
3.1 Introduction . . . 23
3.2 Experimental characterization . . . 24
3.3 Generalized analytical solution . . . 25
3.4 Viscoplastic rheological model . . . 28
3.5 Numerical fluid-dynamic model . . . 29
3.6 Results and discussion . . . 32
3.7 Summary and outlook . . . 34

4 Compaction of fiber bundles 35
4.1 Introduction . . . 35
4.2 Experimental characterization . . . 37
4.3 Theoretical model . . . 38
4.4 Fit of the rheological law . . . 40
4.5 Numerical fluid-dynamic model . . . 41
4.6 Results and discussion . . . 43
4.7 Summary and outlook . . . 44

5 Dilute viscoelastic suspensions 45
5.1 Introduction . . . 45
5.2 Theoretical model . . . 47
    5.2.1 Hydrodynamic system . . . 47
    5.2.2 Viscoelastic model . . . 48
    5.2.3 Solution strategy . . . 49
5.3 Numerical methods . . . 52
    5.3.1 Finite Volume Method . . . 52
    5.3.2 Lattice Boltzmann Method . . . 52
    5.3.3 Coupled algorithm . . . 56
5.4 Model analysis . . . 58
    5.4.1 Sub-grid solution . . . 58
    5.4.2 Validation . . . 61
    5.4.3 Optimization . . . 67
5.5 Summary and outlook . . . 69

6 Deformable fibrous media 70
6.1 Introduction . . . 70
6.2 Theoretical model . . . 73
6.2.1 Volume-averaged equations . . . 74
6.2.2 Microscopic dynamics . . . 77
6.2.3 Model parameters . . . 78
6.2.4 Nondimensionalization . . . 79
6.2.5 Fiber clustering . . . 82
6.3 Numerical methods . . . 83
6.3.1 Fluid flow equations . . . 83
6.3.2 Fiber dynamics model . . . 84
6.3.3 Multi-scale system . . . 84
6.4 Results and discussion . . . 85
6.4.1 Micro-scale model . . . 85
6.4.2 Model assessment . . . 88
6.4.3 Multi-scale model . . . 90
6.5 Summary and outlook . . . 92

7 Conclusions 93
7.1 Conclusions and further work . . . 93
7.2 Conclusiones y trabajo futuro (Español) . . . 97

A GPU implementations 100
A.1 *Sailfish* implementation . . . 101
A.2 Texture memory implementation . . . 101
A.3 Shared memory implementation . . . 103

B Thesis contributions 105

References 107

List of Figures

1.1 Scheme of the resin transfer molding (RTM) process for textile-reinforced composite manufacturing. 2
1.2 Scanning electron micrographies (SEM) of the textile after its use for resin transfer molding process. (a) 200x zoom and (b) 4500x zoom. 4
1.3 Modeling approaches and modeling range of the thesis. 7

2.1 Experimental permeability (K_1 triangles, K_2 circles). As a guide for visualization, a power-law fit of the data for K_1 and K_2 is shown. 11
2.2 Convex hulls for the image segmentation over the original gray scale image (a) and discrete distribution of the micro- and macroscopic volume fractions. The number of bins in the histograms is 35. 12
2.3 (a) Surface extraction from X-ray computed microtomography (CMT) data in the open-source software MicroView [1]. (b) Extracted .stl triangulated surfaces. 14
2.4 (a) Pressure field obtained with the standard CFD approach and simplified geometry (impermeable textile, $\varepsilon_M = 0.5$). Pressure field obtained with the standard CFD approach and reconstructed real geometry. 16
2.5 Comparison of the numerically predicted permeabilities for the simplified geometry (impermeable and permeable cases) and for the CMT-reconstructed geometry with the power law fit of the experimental data (K_1 triangles, K_2 circles). 19

3.1 Experimental system used for the characterization and the squeeze-flow tests. . 24
3.2 Schemes for the analytical solution: cylindrical (a) and wedge-shaped (b) geometries. The dimensions are: H ranges from 10 to 25 mm, L_{max} is 160 mm, R ranges from 15 to 30 mm and D ranges from 100 to 400 mm. 25
3.3 Computational mesh and time evolution of the fluid-dynamic solution for the squeeze-flow of the wedge-shaped specimen with $V = 50$ mm/min. 30

3.4 Comparison of analytical and numerical solutions with experimental data for the squeeze-flow test at constant velocity. The experimental data and numerical solutions are least-square fitted. 31

3.5 Comparison of the dimensionless analytical and numerical solutions with experimental data for $V_1 = 50$ mm/min, $V_2 = 100$ mm/min and $V_3 = 250$ mm/min . Inset: decomposition of the analytical solution F^* for $V_2 = 100$ mm/min (red) in its contributions. For $L/H \gg 1$ the flow regime is shear-dominated, while for $L/H \ll 1$, the flow regime is dominated by $O(L/H)^2$-order forces. In the transition region normal forces prevail. 32

3.6 Comparison of the analytical solution with experimental data for the squeeze-flow test at constant force. 33

4.1 (a) Experimental set-up for the textile compaction test. (b) Obtained experimental compression curve compared with the dry compression of a 5H weave (20 plies) [2]. 37

4.2 (a) Representative elementary volume (REV) extracted from a SEM image and schematic of the compaction model. (b) Compaction force at the yarn level as a function of the yarn height and fit of Eq. (4.4). In the inset, comparison of the evolution of the contact length as a function of the yarn height obtained with the CFD model with that from Eq. (4.5). 38

4.3 (a) Evolution of the fiber volume fraction during the compression according to the numerical model. (b) Comparison of the compaction force obtained with the CFD model with experimental data. In the inset, evolution of the fiber volume fraction ϕ_m according to the analytical model of Eq. (4.7). 43

5.1 Overview of the proposed approach. λ_P and λ_F are the time-scales associated respectively with the polymer molecules and the viscosity of the solvent. . . . 47

5.2 Lattices and relative discrete distribution functions: five links for D2Q5 (black color) and four additional links for D2Q9 (gray diagonals). 53

5.3 Shaded surface of the analytical equilibrium PDF (Eq. 5.35) on a 1,681 DoF lattice (a) and ℓ_2-*norm* convergence of ψ with $\tau = 0.55$ (b). 56

5.4 Start-up plane Couette flow: shaded surface of the equilibrium PDF for Wi_m = 5 on a 1,681 DoF lattice (a) and dimensionless shear stress evolution $\hat{\sigma}_{p_{xy}}$ for different Wi_m on a D2Q9 lattice with 3,721 DoF and $\tau = 0.55$ (b). 57

5.5 Error convergence for $Wi_m = 1$ and 5 on the two lattices (a) and stability map for D2Q9 and D2Q5 lattices (b). 58

5.6 Mesh layout close to the cylinder surface (2 m length and 1,770 cells displayed). 61

5.7 Profiles of the dimensionless viscoelastic stresses on the symmetry plane and on the cylinder surface for $Wi_M = 0.6$. The results for the two tested FVM meshes (M1, M2 and M3) are compared with ref. [3]: (a) $\hat{\sigma}_{p_{xx}}$ (b) $\hat{\sigma}_{p_{xy}}$ (c) $\hat{\sigma}_{p_{yy}}$. 63

5.8 Contours of dimensionless molecular elongations (configuration tensor) for $Wi_M = 0.6$: (a) $\langle\langle\hat{\xi}_x\hat{\xi}_x\rangle\rangle$ (b) $\langle\langle\hat{\xi}_x\hat{\xi}_y\rangle\rangle$ (c) $\langle\langle\hat{\xi}_y\hat{\xi}_y\rangle\rangle$. 64

5.9 Contours of dimensionless viscoelastic stresses for $Wi_M = 0.6$: (a) $\hat{\boldsymbol{\sigma}}_{p_{xx}}$ (b) $\hat{\boldsymbol{\sigma}}_{p_{xy}}$ (c) $\hat{\boldsymbol{\sigma}}_{p_{yy}}$. 65

5.10 Contours of dimensionless viscoelastic stresses for $Wi_M = 0.9$: (a) $\hat{\boldsymbol{\sigma}}_{p_{xx}}$ (b) $\hat{\boldsymbol{\sigma}}_{p_{xy}}$ (c) $\hat{\boldsymbol{\sigma}}_{p_{yy}}$. 66

5.11 Discrete distribution of Wi_m in the physical domain (mesh M1, number of bins 50, $Wi_M = 0.6$). 67

6.1 Schematics of the scales considered and relative representative elementary volumes (REV): yarn macro-scale (a) and fiber micro-scale (b). Fiber configurations (c) and correspondent cluster density Ω, which is defined as the number of single or connected components per fiber. 73

6.2 (a) Numerical data obtained for Ω as a function of the viscous number I_m. The main figure shows the collapse of the data in the inset with the relaxation time θ ($\hat{\xi}_{max} = 10$, $\hat{\xi}_c/\hat{\xi}_{max} = 0.5$). (b) Cluster density Ω as a function of the contact/bending ratio $\hat{\xi}_c/\hat{\xi}_{max}$ for $\hat{\xi}_{max} = 10$ and of the maximum extensibility $\hat{\xi}_{max}$ for $\hat{\xi}_c/\hat{\xi}_{max} = 0.3$ (inset). Figures (c), (d) and (e) show an example configuration of the probability densities at the corresponding points in Fig. 6.2(b). 80

6.3 Micro-scale phase diagram for deformable fibrous media (a). The diagram shows the iso-colors of the cluster density Ω as a function of the microscopic viscous number I_m, the normalized microscopic porosity $\tilde{\varepsilon}_m$ and the maximum extensibility $\hat{\xi}_{max}$ ($\hat{\xi}_c/\hat{\xi}_{max} = 0 \div 1$ and $D = 10^{-12}$ m^2/s). The numerical data are best fitted and a reduced number of points per dimension are shown to allow a proper visualization. Figure (b) shows the iso-Ω contours on the plane $\hat{\xi}_{max} = 10$ in (a). 82

6.4 Comparison of the reduced viscosity of the proposed model with that of wet granular media. Dimensionless viscosity as a function of the normalized volume fraction $\tilde{\phi}_m$ (a) and of the viscous number I_m (b). The maximum extensibility is $\hat{\xi}_{max} = 10$, the diffusion coefficient $D = 10^{-10}$ m^2/s and the constant $A = 0.1r^2$ (Eq. (6.37)). 85
6.5 (a) Comparison of the numerically predicted effective permeability with the analytical solution of Eq. (6.2) for rigid porous media. In the inset, comparison of the microscopic permeability given by Eq. (6.1) and Eq. (6.33). (b) Multi-scale phase diagram for fibrous media. In the blue area, the microscopic porosity has a negligible effect on permeability; in the green area, the effects of fiber deformations are negligible; in the red area, the effect of fiber deformation significantly modifies the effective permeability. In the inset, flow field configuration at point (p). The model parameters for the simulation are: $\hat{\xi}_{max} = 10$, $\varepsilon_M = 0.36$, $\varepsilon_m = 0.8$, $I_M = 0.6$, $\hat{\xi}_c/\hat{\xi}_{max} = 0.36$, $D = 10^{-11}$ m^2/s and $z = L_z/2$. The colorbar shows the Ω scale for the contours and the velocity magnitude (within parentheses) for the pathlines. 87
6.6 (Color online) Multi-scale permeability of deformable fibrous media: $\Omega = 0.1$ (a) and $\Omega = 0.5$ (b). The colorbars show the ratio between the effective permeabilities in the deformable and rigid cases. 89

A.1 Comparison of the computational time for compiled a compiled C code and SAILFISH (D2Q9 lattice with $\tau = 0.55$) on the available hardware (a) and GPU profiling for the coupling (normalized quantities). 100
A.2 Scheme of the CUDA implementation using shared memory (a) and comparison of the computational time for compiled C and the CUDA implementation using shared memory (D2Q9 and D2Q5 lattices with $\tau = 0.55$) (b). 102

List of Tables

1.1 Overview of the modeling work in this thesis. 8

2.1 Comparison of the numerically predicted permeabilities for the simplified geometry (impermeable (I) and permeable (P) cases) and for the CMT-reconstructed geometry with the experimental data (K [m^2] and θ [°]). 18

3.1 Fitting of the parameters for the Herschel-Bulkley model. V is the squeeze velocity [m/s], n the power-law index $[-]$ and K the consistency index $[Pas^n]$. 27

5.1 Comparison of the computational time [s] and relative numerical error [%] for the two lattices for $\tau = 0.55$ and $\tau = \tau_{max}$ (start-up plane Couette flow at $Wi_m = 5$). 59

5.2 Comparison of the calculated drag factor with the results obtained by Chauvière and Lozinski [3] for different Weissenberg number. 62

5.3 Summary table of the three sub-grid solution approaches: ME (minimize error), SA (strain-adaptive) and MS (maximize speed). The comparison of the computational speed-up per FVM iteration refers to different approaches on the same stencil (results for mesh M1). 68

6.1 Geometrical parameters and physical properties of the glass fibers considered. 76

6.2 Summary table of the model parameters. 78

A.1 Comparison of the computational time [s] for a compiled C code and the CUDA code (shared memory implementation). 103

Nomenclature

Due to the large number of symbols, only the most common are reported with their use (unless otherwise stated in the text). Specific uses are explained in each chapter.

Roman Symbols

A	Area $[m^2]$
x, y, z	Cartesian coordinates $[m]$
K	consistency index $[Pas^n]$ or permeability component $[m^2]$
$\mathbf{u}$	convection vector in phase space $[-]$
D	diffusion coefficient $[m^2/s]$ (Ch. 6)
b	finite dimensionless extensibility parameter $[-]$
f	single particle distribution function $[s^3m^{-6}]$
$\mathbf{F}$	force vector $[N]$
C	geometrical constant $[-]$ (Ch. 2)
H	height $[m]$ or connector force law $[N/m]$
$\mathbf{I}$	unit tensor $[-]$
c	lattice speed $[lu/lt]$
L	length $[m]$
m	mass $[kg]$, reciprocal of cluster dimension $[-]$ (Ch. 6)
N	number of nodes $[-]$ (Ch. 5), number of fibers [-] (Ch. 6)
$\mathbf{K}$	permeability tensor $[m^2]$
n	non-Newtonian power-law index $[-]$

R, r	radius $[m]$
$\mathbf{R}$	rotation matrix $[-]$ (Ch. 2)
p	static pressure $[Pa]$
T	absolute temperature $[K]$
d	thickness $[m]$
$\mathbf{v}$	physical velocity vector $[m/s]$
V	squeeze velocity [m/s] (Ch. 3,4), volume $[m^3]$ (Ch. 5,6)
$\mathbf{W}$	Wiener process (or standard Brownian motion) $[-]$
E	Young modulus $[Pa]$

Greek Symbols

ϑ	polar angle $[rad]$
η	apparent viscosity $[Pas]$
Λ	blockage ratio $[-]$
Ω	collision operator $[s^2m^{-6}]$ (Ch. 5), cluster density [-] (Ch. 6)
ρ	density $[kg/m^3]$
σ	normal stress component [Pa] (Ch. 3), diffusion coefficient $[m^2/s]$ (Ch. 5)
ζ	drag factor $[-]$
μ	dynamic viscosity $[Pas]$
χ	Euler characteristic $[-]$
φ	generic scalar quantity $[-]$
ν	kinematic viscosity $[m^2/s]$
τ	shear stress component [Pa] (Ch. 3,4), lattice relaxation time $[-]$ (Ch. 5,6)
ω	lattice weights $[-]$
$\boldsymbol{\xi}$	phase space vector $[m]$
ε	porosity $[-]$
ψ	probability density function $[-]$

θ	rotation angle $[rad]$ (Ch. 2), physical relaxation time $[s]$ (Ch. 5,6)
γ	strain $[-]$
$\boldsymbol{\sigma}$	stress tensor $[Pa]$
$\boldsymbol{\kappa}$	transpose of velocity gradient tensor $(\nabla\mathbf{v})^\dagger$ $[s^{-1}]$
β	viscosity ratio $[-]$ (Ch. 4), conductivity exponent [-] (Ch. 5)
ϕ	volume fraction $[-]$

Superscripts

c	connector or percolation (threshold)
d	drag (Ch. 6)
eq	equilibrium
h	hydrodynamic (Ch. 6)
$*$	dimensionless quantity (Ch. 3), intermediate quantity (Ch. 5)
ν	intrinsic quantity (Ch. 6)
neq	non-equilibrium
n	quantity at time step n

Subscripts

c	contact (Ch. 6)
cr	critical
eff	effective
f	fiber
ν	fluid phase
i, j	index
M	macro
m	micro
o	open space
p	polymeric

ξ	operator in phase space
x	operator in physical space
ref	reference
σ	solid phase
s	solvent
0	yield condition (Ch. 3,4), initial condition (Ch. 6)

Other Symbols

k_B	Boltzmann constant $[m^2kgs^{-2}K^{-1}]$
$*$	convolution operator
$\mathbf{x}^1 \otimes \mathbf{x}^2$	diadic product $(\mathbf{x}^1 \otimes \mathbf{x}^2)_{ij} = x_i^1 x_j^2$
$\hat{x}, \hat{\mathbf{x}}$	dimensionless scalar or vector (or tensor)
$\delta\xi$	lattice spacing $[lu]$
δt	lattice time step $[lt]$
Δx	discrete increment of the quantity x
$\nabla \cdot (x)$	divergence operator
C_D	drag coefficient $[-]$
$\langle\langle x \rangle\rangle$	ensemble averaging
$\nabla\,(x)$	gradient operator
δ_{ij}	Kronecker delta funtion (1 if i = j and 0 otherwise)
$\nabla^2(x)$	Laplacian operator $\nabla \cdot (\nabla(x))$
c_s	lattice speed of sound $[lu/lt]$
$\overline{x}$	mean of quantity x
$\tilde{x}$	normalized quantity
S	Plasticity number $[-]$
$\dot{x}$	(flow) rate of the quantity x
Re	Reynolds number $[-]$

$\mathbf{x}^1 : \mathbf{x}^2$	saturation product $\mathbf{x}^1 : \mathbf{x}^2 = \sum_i \sum_j x^1_{ij} x^2_{ji}$
$\mathbf{x}^1 \cdot \mathbf{x}^2$	scalar (dot) product
$\mathrm{II}_{\mathbf{x}}$	second invariant of tensor $\mathbf{x}$
St	Stokes number [-]
$\mathbf{x}^\dagger$	transposed of vector or matrix
$\langle x \rangle$	volume averaging
Wi	Weissenberg number $[-]$

Acronyms

BGK	Bhatnagar-Gross-Krook
CFD	computational fluid dynamics
CAD	computer aided design
DoF	degrees of freedom
FENE	finitely extensible non-linear elastic
FVM	finite volume method
FSI	fluid-structure interaction
GPU	graphic processing unit
LBM	lattice Boltzmann Method
LCM	liquid composite molding
CMT	computed X-ray microtomography
ODE	ordinary differential equation
PDE	partial differential equation
PDF	probability density function
REV	representative elementary volume
RTM	resin transfer molding
SEM	scanning electron microscopy

Chapter 1

Introduction

1.1 Motivation

In the last few years, the interest of the aeronautical and terrestrial transport industry in the production and utilization of textile-reinforced composites has grown sensibly. This is basically due to the remarkable mechanical properties of these materials compared to their reduced weight. Currently, the most employed manufacturing processes for their fabrication rely on autoclave curing: heat and pressure are applied on vacuum bags to achieve high volume fractions of the reinforcement and low number of defects due to the presence of voids. This technique provides high quality standards of the final components, however it also implies high acquisition and production costs. For this reason, the interest of the industry in out-of-autoclave processes such as those using injection or infusion is currently increasing.

Out-of-autoclave manufacturing processes go under the name of Liquid Composite Molding (LCM), a term that encompasses, among others, the Resin Transfer Molding (RTM), the Resin Infusion (RI) and their relative vacuum assisted versions (VARTM and VARI) [4]. Perhaps, one of the most employed is RTM [5], due to its capacity to handle complex geometries, its cost-effectiveness and high throughputs. The basic isothermal technique consists in the injection of a catalyzed resin into a closed cavity, where a pre-placed fiber stack lies (see Fig. 1.1). Once the resin has completely permeated the preform, the walls of the mold are subjected to high temperatures in order to induce the curing of the resin and therefore the hard final composite. The current challenge for LCM is to achieve the same quality standards as those achievable with in-autoclave processing.

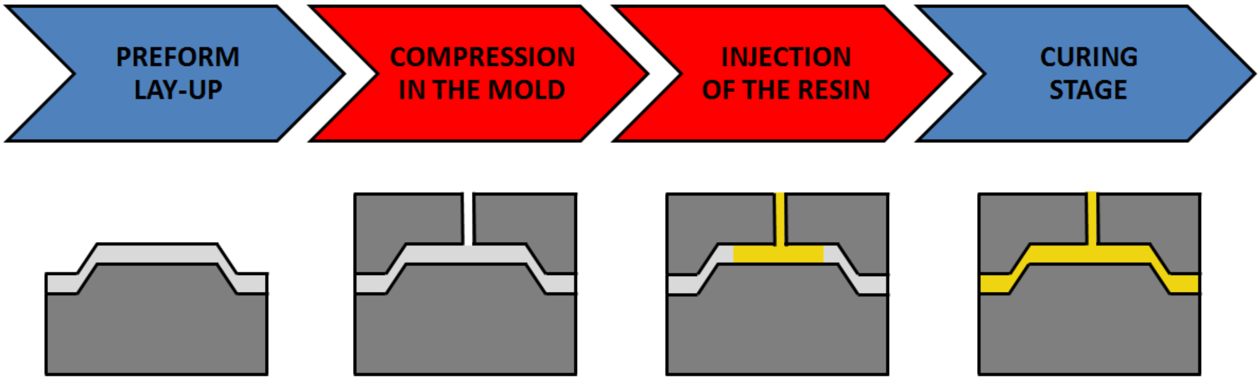

Figure 1.1: Scheme of the resin transfer molding (RTM) process for textile-reinforced composite manufacturing.

The complexity of the physics and that of the non-linear interactions among the governing phenomena of the process makes it difficult to develop efficient predictive models. Nonetheless, a thorough understanding of the physics is of fundamental importance, since the final quality of the output depends mostly on the process parameters [6]. The dominant physical phenomena involved are the fluid mechanics of the resin permeating the fiber reinforcement, the heat transfer and the chemical reactions due to curing. The final goal of a reliable model would hence be to accurately describe the dynamics of the resin percolating the textile and predict the fiber stack saturation. Mold filling simulation software such as PAM-RTM [7], RTM-Worx [8] or LIMS [9], are valuable tools for process optimization. However, the mold filling simulation requires the permeability of the textile as an input parameter; therefore its accurate evaluation is remarkably important. Mostly due to the hierarchical structure of the fibrous preforms, an accurate evaluation of the permeability is a challenging task, both from the experimental and numerical point of view.

In a first experimental benchmark published in 2011 [10], the permeability data from twelve institutions from six countries were compiled and compared for two different fabrics. The test conditions and procedures were not regulated (e.g. linear or radial injection, saturated or unsaturated flow, constant pressure or flow rate, test fluids and fiber volume fraction). The result was a significant scatter on permeability, up to one order of magnitude, among all participants for both reinforcements tested. The numerous differences between experimental procedures could not be associated to the observed permeability scatter; consequently it was difficult to point out the influence of a specific parameter on the permeability. Only recently, a second permeability benchmark in 2014 [11] showed that with a stricter regulation of the procedures and of the experimental conditions, a better comparison of the results can be achieved. The scatter among the data obtained while respecting the guidelines was below 20-25% (either among all participants and among the various tests from each single participating institution). The causes of the uncertainties on permeability measurements and low reproducibility of the experiments have not yet been identified.

The permeability of the reinforcement depends on several factors, such as: the structure of the textile, the arrangement of the layers, the adaption to the mold, the operating conditions, the geometry of the component and the interaction between the fluid and the textile. All these issues are at the origin of the uncertainty and low reproducibility of the experimental measurements. Furthermore, experimental procedures are expensive and time consuming, which motivates the interest in the development of alternative strategies for the prediction of permeability.

From a modeling point of view, the problem is complicated by the hierarchical structure of the textile. The commonly used preforms for these applications are made up of fibers, which are bunched in yarns, which in turn are bundled in a fabric. This results in multiple scales to be considered, typically ranging between one and three orders of magnitude. As a consequence, analytical approaches can be adopted only under strict simplifying assumptions, whilst the main issue concerned with numerical approaches is the computational cost, which is a constraint on the fidelity of the virtual geometrical reconstruction.

For these reasons, the most commonly adopted practice consists in the numerical simulation of the fluid flow in a representative elementary volume (REV) of the textile, where the intra-yarn permeability is computed by the so called “constitutive” relations [12], that is, analytical solutions or experimental correlations which serve as auxiliary means for the numerical simulations [13, 14]. The effective permeability is then recovered by Darcy’s law.

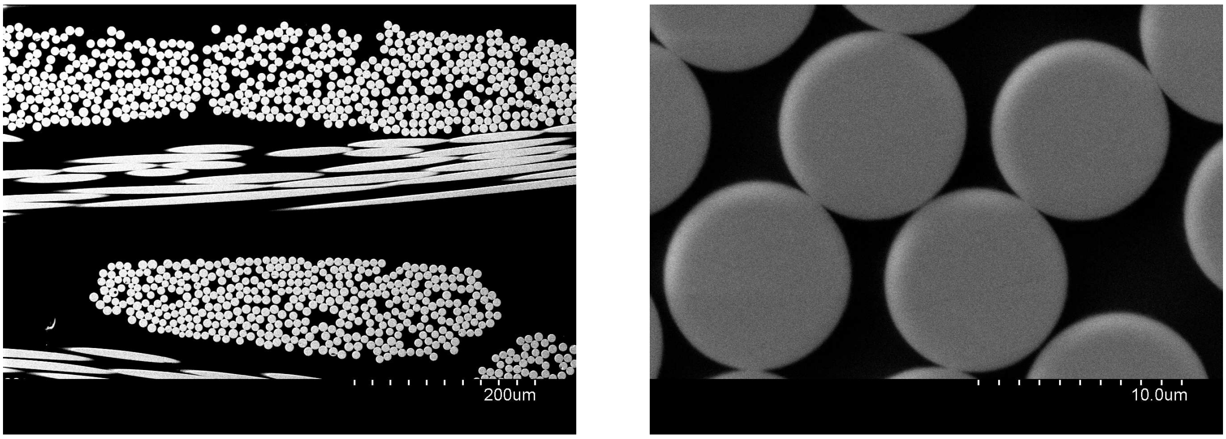

(a) (b)

Figure 1.2: Scanning electron micrographies (SEM) of the textile after its use for resin transfer molding process. (a) 200x zoom and (b) 4500x zoom.

Despite its simplicity, this approach often results in unacceptable loss of accuracy on the permeability estimation with respect to the experimental data, due to:

- The geometrical reproduction of the textile. Several tools are already available for this purpose, as for example the open-source software TexGen [15]. These tools generally embed predefined mathematics for the most common textiles; however the simplified geometry obtained does not accurately reproduce the real one.
- The assumptions on the intra-yarn topology. The empirical expressions for the intra-yarn permeability requires simplifying geometrical assumptions, which are not representative of the real topology and result in a loss of important information, as for example anisotropy.
- The interaction between the fluid flow and the mat. Considering the textile as a rigid body can be a limiting assumption, since its deformation induced by the fluid flow can sensibly affect the overall permeability.

All these issues are strictly related to the deformation that the textile undergoes during the composite production process, that is: (i) the compaction in the mold and (ii) the injection of the resin. Both processes cause, via different mechanisms, a complex deformation of the hierarchical structure of the textile, which affects its hydraulic conductivity. Figures 1.2(a) and 1.2(b) show two images obtained by scanning electron microscopy (SEM) of the textile after its use for resin transfer molding. The irregular shape of the yarns yield by the fiber deformation is mainly result of the compression in the mold, since the deformation due to the injection of the resin is (partially) reversible and cannot be visually analyzed. The effective permeability is then affected by the porosity distribution resulting from the compression and the fiber dynamics during the injection [16].

A unified framework for this kind of analysis has been largely studied and is currently under investigation by the textile research community [17]. However, the currently available numerical models predict the permeability with an error between 20 and 50% with respect to the experimental data [18, 19], which motivates further efforts.

1.2 Objectives

The objective of the thesis is the analysis of the deformation that the textile undergoes during the production process (Fig. 1.1), that is, the compaction in the mold and the injection of the resin. The two stages are addressed using non-conventional modeling techniques, fully based on computational fluid dynamics. The developed models must be able to account for the multi-scale nature of the problem, in order to understand how the topology of the fibers affects the bulk hydraulic conductivity during the two aforementioned stages of the production process. The objectives can be summarized as follows:

1. COMPACTION IN THE MOLD
    - development and validation of a numerical framework for the squeeze flow of viscoplastic soft solids using computational fluid dynamics;
    - development of a theoretical framework for the analysis of the compaction of textiles using the developed numerical model.
2. INJECTION OF THE RESIN
    - development and validation of a coupled numerical method for the efficient simulation of multi-scale suspensions;
    - development of a theoretical framework for the analysis of the fiber dynamics during the injection stage, to be solved with the developed numerical method.

Finally, the acquired knowledge and the models proposed will allow for a better understanding of the causes of the discrepancy between predictive models and experimental data.

1.3 Methodology

The flow regimes encountered in fibrous porous media are basically three: (i) steady Stokes flow; (ii) steady laminar (inertial) flow and (iii) unsteady turbulent flow. In this work we focus on the Stokes flow (i), which is the characteristic regime of infiltration for liquid composite molding. For Stokes flow, the stream-wise pressure drop Δp is linearly related to the flow rate through the permeability of the medium K, by the well known Darcy's law:

$$\Delta p = -\frac{\mu}{K}v; \tag{1.1}$$

where μ is the viscosity of the fluid and v the superficial flow velocity. In this simple relationship, the proportionality constant K represents the hydraulic conductivity of the porous material, which depends mainly on its pore structure.

In hierarchically-structured fibrous materials such as those for liquid composite molding, the effective permeability depends both on the macroscopic structure (yarn weaving) and on the pore-level structure (fiber topology), being the former affected by the latter. Therefore macroscopic "bulk" properties, such as permeability, ultimately depend on the physics at the smallest scale, that is, the fiber scale. A reliable evaluation of the effective permeability K should then include all the physics, all the way down to the fiber scale. However, the difference between the length scales to be considered in these materials, generally up to three orders of magnitude, poses a major computational challenge.

In order to account for the underlying microscopic physics on "bulk" properties, a macroscopic description should be provided with averaged quantities obtained from micro-scale models. This involves the so called up-scaling or closure problem. However, micro-scale models are often limited to very few applications, due to the computational resources available to solve them. Alternatively, an improved macroscopic description can be obtained with mesoscopic approaches. As the word itself says, these latter modeling approaches lie in between micro- and macroscopic modeling techniques (Fig. 1.3) and are meant to provide a link between micro- and macroscopic physics. The advantage of meso-scale modeling techniques is their ability to preserve essential information of the microscopic physics with reduced computational cost, which remarkably improves the phenomenological description. For these reasons these approaches are rapidly gaining popularity in material science (see, for example, [20, 21]).

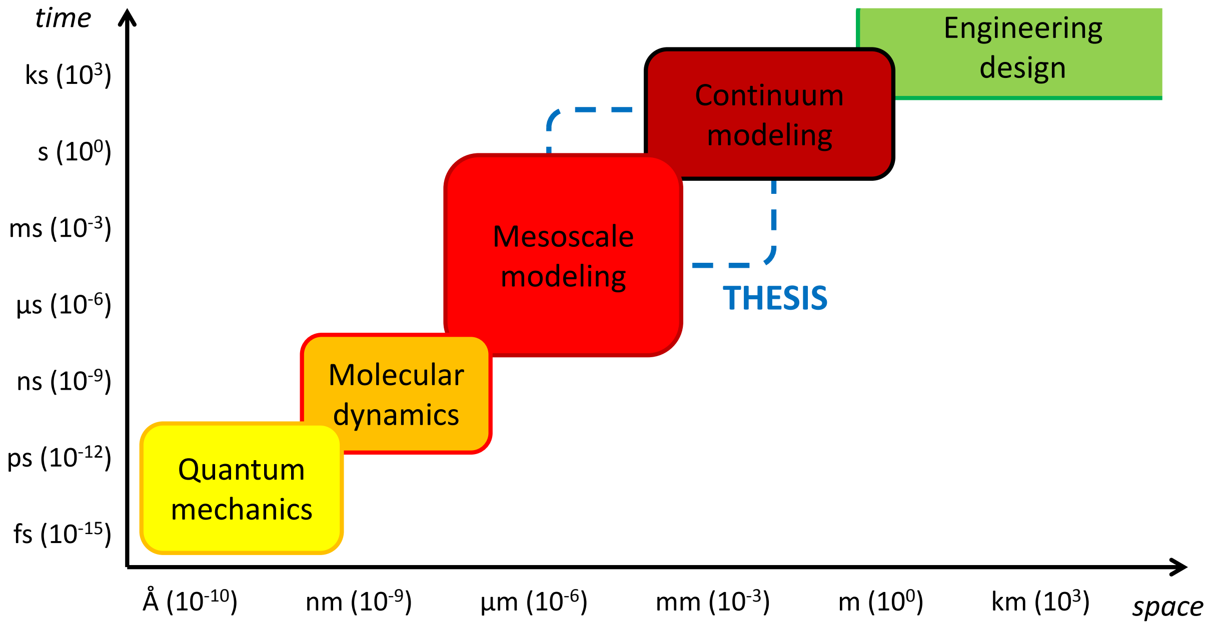

Figure 1.3: Modeling approaches and modeling range of the thesis.

As explained in the previous section, the objective of the thesis is the analysis of the deformation that the fibrous preforms undergo during the manufacturing processing (Fig. 1.1) and how the resulting structure affects the hydraulic conductivity. Considering that the diameter of the fibers in these textiles is typically lower than 10 μm, while the characteristic dimension of the yarn is typically around 1 mm, mesoscopic an continuum modeling techniques are employed (Fig. 1.3).

From a phenomenological point of view, in this work the textile behavior is always modeled by analogy with a complex fluid. During the compaction in the mold, the yarn is modeled as a flowing granular material. During the injection stage, the yarn is modeled as a non-Brownian suspension of fibers. Complex fluids can be considered homogeneous at the macroscopic (or bulk) scale, but are disordered at the microscopic scale and possess structure at an intermediate scale. That is, the macroscopic flow behavior (rheology), is a strong function of the fluid micro-structure. In this sense, the analogy yields information on how the structure of the fibers affects the bulk behavior (e.g. the permeability).

Table 1.1: Overview of the modeling work in this thesis.

	Compaction in the mold	**Injection of the resin**
Approach	*Continuum modeling*	*Mesoscopic modeling*
Development	Viscoplastic soft solids CHAPTER 3	Dilute colloidal suspensions CHAPTER 5
Application	Entangled fibrous materials CHAPTER 4	Deformable fibrous media CHAPTER 6

The first modeling block of the thesis concerns the analysis of the deformation that the textiles undergo during the compaction in the mold (Fig. 1.1). A continuum model is firstly developed and validated for the squeeze flow of epoxy-based materials, whose rheology is well represented by a viscoplastic constitutive law. The model is then applied to the compaction of textiles, where information about the fiber behavior is inferred from the macroscopic "bulk" behavior of the yarns using a simplified analytical model for the deformation of the yarns. In this case, the continuum description is enriched by meso-scale information, extracted from the rheology using a top-down approach (see Tab. 1.1).

The second modeling block of the thesis concerns the analysis of the deformation that the textiles undergo during the injection of the resin (Fig. 1.1). A theoretical and numerical framework is first developed and validated for the direct numerical simulation of dilute colloidal suspensions of polymeric molecules. The model is then tailored and applied to the analysis of the flow-induced fiber deformation in hierarchical fibrous media. In this case the yarn is modeled as a non-Brownian suspension of fibers with confining potentials. Here, modeling proceeds from a fully mesoscopic coarse-grained approach for polymer molecules to a statistical model for the fiber dynamics, following a bottom-up approach (see Tab. 1.1).

1.4 Thesis overview

The thesis is organized in seven chapters (including the present one). The structure of the document follows the two steps of the manufacturing process (Fig. 1.1) and the modeling framework shown in Tab. 1.1. The outline of each chapter is as follows.

2 In this chapter, the permeability of a textile reinforcement for liquid composite molding is analyzed by experimental and numerical means. It is shown that by simplified numerical approaches the experimental data cannot be accurately reproduced over the whole range of porosities. The causes of the uncertainties are discussed.

3 This chapter concerns the development of the fluid-dynamic model for the compression of viscoplastic soft solids. The model is validated against experimental data for an epoxy-based material and an analytical solution for the compressive forces is generalized for arbitrary shapes of the specimen.

4 The model developed in the previous chapter is applied to the analysis of the compression of the yarns. To this end, the mechanical response of the textile under compression is first analyzed experimentally. The compression curve together with a simplified analytical model allows to model the yarn as a flowing granular material and to extract information on the dynamics of the fibers.

5 In this chapter the mesoscopic model for viscoelastic suspensions is developed. Special emphasis is given to the coupling of the numerical methods and to the efficient implementation of the solution for the meso-scale equation by lattice Boltzmann method (LBM) on graphic processing units. The details of the implementations and of the related issues are reported in Appendix A.

6 The model developed in the previous chapter is tailored for the analysis of the fiber deformation. In this chapter, particular emphasis is given to the interpretation of the model and to the theoretical framework. The results obtained are presented in the form of phase diagrams for the permeability of deformable fibrous media.

7 Finally, the conclusions from the work done are drawn, together with a discussion of the possible improvements of the proposed models as an indication for further development of this work. A unified framework fully based on computational fluid dynamics is proposed for the analysis of the permeability of textiles during the manufacturing process.

Chapter 2

Permeability of textile reinforcements

2.1 Introduction

In this chapter, the permeability of an 8H Satin weave textile is analyzed. A complete experimental analysis of the textile object of this study is first presented, namely: effective permeability, compression curve of the textile, analysis by scanning electron microscopy (SEM) and computed X-ray microtomography (CMT). The micrographies are processed using image-analysis techniques, which allows to extract informations on micro- and macroscopic porosities. Similarly, the microtomographic data is also processed in order to extract the real geometry of the textile after its use for liquid composite molding. We then perform a numerical evaluation of the permeability adopting a standard CFD approach, and show that the experimental permeability cannot be recovered over the full range of porosities. The causes of this discrepancy and the related uncertainties in the numerical prediction of the permeability of textiles are presented and discussed.

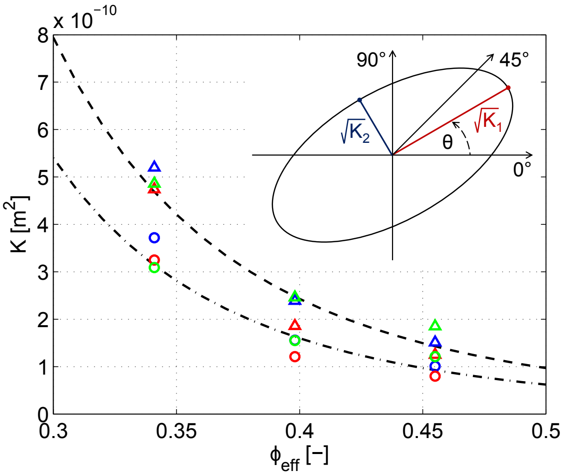

Figure 2.1: Experimental permeability (K_1 triangles, K_2 circles). As a guide for visualization, a power-law fit of the data for K_1 and K_2 is shown.

2.2 Experimental data

2.2.1 Permeabilities

In the eight-harness satin (8H Satin) weave, one warp yarn floats over seven perpendicular weft yarns and under one (0/90° weave). It is a very pliable weave, which is why it is used for forming over curved surfaces. In this work, the permeability of the textile is evaluated by radial injection technique [22] in unsaturated conditions using a specifically-designed test bench. Three tests have been performed for three different volume fractions: $\phi = 0.341$, $\phi = 0.3981$ and $\phi = 0.455$. The volume fraction has been changed increasing the number of textile layers inside the mold cavity. The principal permeability components and orientation of the ellipse are computed from an analytical solution for radial flow [22]; the values obtained for the three cases are shown in Fig. 2.1. As a guide for visualization a power-law fit of the data for K_1 and K_2 is also shown. The mean orientation angle θ of the ellipse for the three tested volume fractions is respectively 54.60°, 48.72° and 45.51°.

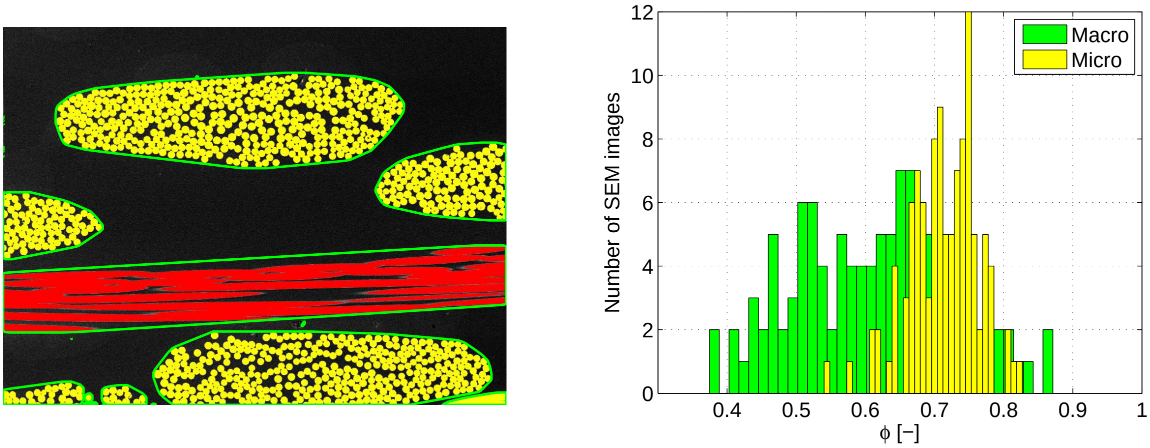

(a)

(b)

Figure 2.2: Convex hulls for the image segmentation over the original gray scale image (a) and discrete distribution of the micro- and macroscopic volume fractions. The number of bins in the histograms is 35.

2.2.2 SEM image analysis

In order to understand the structure of the textile after its compression, a set of 110 scanning electron microscopies are realized on a 15 mm square specimen of the textile (seven layers). The specimen is prepared for the analysis using a standard metallographic procedure, therefore it is polished using successively finer abrasive particles. The images obtained are in gray scale uncompressed .TIF format, which is a raster format for graphic representation. The resolution of the images is 1024x768, and the dimension of the pixel is approximately 0.5 μm. The images show that the mean diameter of the fibers is around 8 μm, while the major axis of the yarns is around 500 μm. The image analysis is performed in Matlab®. The images are loaded as 8 bit unsigned integer matrices and converted to binaries (black and white) using the mean value of the gray scale as threshold. The effective volume fraction can be easily calculated by the sum of the white pixels over the total number of pixels of the image, but more information can be extracted from the images, such as the macro- and microscopic volume fractions. For this purpose, the edges of the yarns in the images must be identified. In order to extract the edges, the connected components in the black and white images (i.e. the continuous white regions) are first identified and labeled. Then a convex hull, that is the smallest convex polygon enclosing all points, is built for each continuous region. All the pixels within the hulls are sequentially set to 1 (white) and the procedure is repeated until no changes occur. This procedure successively fills the continuous regions, that is the fibers that are in contact with other(s). The edges of the yarns are finally obtained (see Fig. 2.2(a)). Transversal yarns (in red) are identified by regions which horizontally span the whole picture. The macroscopic volume fraction can be straightforwardly obtained from the final mask, as the sum of the pixels in the filled regions to the total number of pixels in the image. Similarly, the microscopic volume fraction of each yarn is obtained by the sum of the white pixels to the total number of pixels in each hull. The results of the analysis for the whole set of images are shown in Fig. 2.2(b). A mean value of the micro and macroscopic volume fractions is finally obtained for the specimen ($\phi_m = 0.73$ and $\phi_M = 0.6$), while the distributions provide a qualitative indication of the degree of compactness of the fibers with respect to the yarns.

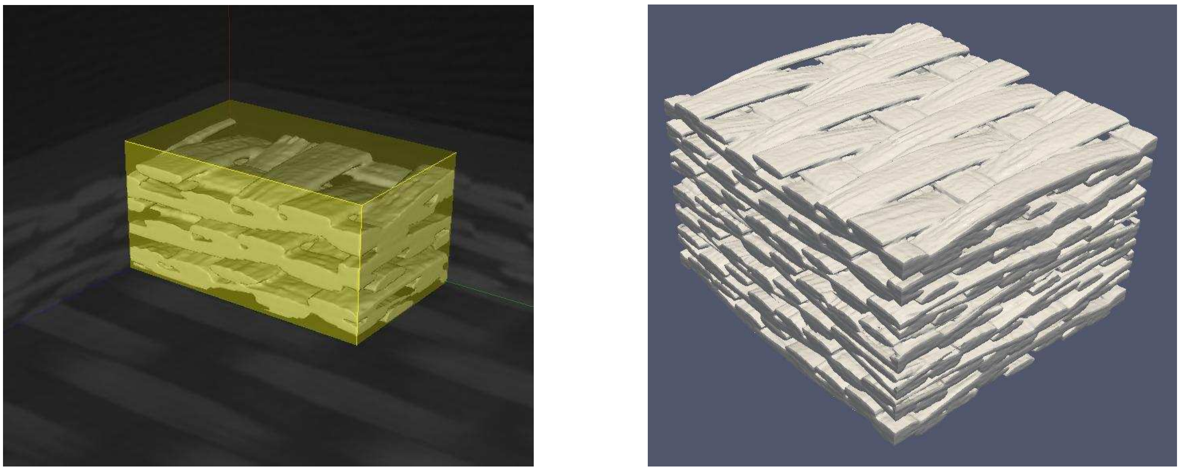

(a) (b)

Figure 2.3: (a) Surface extraction from X-ray computed microtomography (CMT) data in the open-source software MicroView [1]. (b) Extracted .stl triangulated surfaces.

2.2.3 CMT data analysis

The X-ray computed microtomography (CMT) is a powerful, non-destructive method to obtain spatially resolved information about porous materials. In this case we use this technique to analyze a 15x15 mm specimen of the textile extracted from the composite after the production process. The specimen is sampled by a microtomographic scanner, which acquires two-dimensional images of the object in a regular three-dimensional pattern. The 3D volume can then be rendered using the produced images and their associated information about the reference system. In this work we use the open-source software MicroView [1] for the analysis of the data. The software provides several tools for the analysis of the images, such as the gray-scale statistics. The surface of the object can be extracted as an iso-color surface, whose threshold value is chosen on the basis of the gray-scale distribution of the images (Fig. 2.3(a)). Typically the best choice lies close to a minimum in the distribution. The extracted surface is saved in stereo lithography file format (.stl), that is a triangulated surface (Fig. 2.3(b)).

2.3 Standard CFD approach

2.3.1 Representative geometry

In this section we adopt a standard technique for the numerical evaluation of the permeability in textile preforms. A simplified geometry of a representative elementary volume (REV) of the textile is modeled by computer aided design (CAD). For the sake of completeness, we remark that open-source software is also available for the generation of the geometry, such as TexGen [15] or WiseTex [17]. The REV is chosen so that geometrical periodicity yields along the three principal directions (see Fig. 2.4(a)). Two geometries for two macroscopic porosities $\varepsilon_M = 0.36$ and $\varepsilon_M = 0.50$ are generated. The different porosities are obtained by changing the ratio between the major and minor axes of the elliptical section of the yarns. The geometries are enclosed by complementary domains, that is the smallest fitting parallelepiped, and cut by Boolean operations. The resulting domains are meshed using 2M ca. mixed hexahedral and tetrahedral elements for the fluid-flow simulation in ANSYS Fluent®.

2.3.2 CMT reconstructed geometry

The CMT data allows for the exact geometry, eventually down to the fiber scale if the resolution of the micro-tomographic data is smaller than the fiber diameter. In this work we do not dispose of such resolution, since the fiber diameter is around 8 μm, while the resolution is around 15 μm. Notice that even if the data were available, the geometry reconstruction and the simulations would not be computationally affordable.

The extraction of the geometry from the .stl file format is not straightforward for complex parts such as ours; therefore manual operations would be needed for the reconstruction. In order not to loose important features of the geometry, we decided to avoid geometrical reconstruction and directly use the triangulated surface for the discretization. Using a fine triangulation, this procedure allows for the exact geometry (see Fig. 2.4(b)), as given by the CMT data. The resulting domains consist in 6M ca. tetrahedral elements.

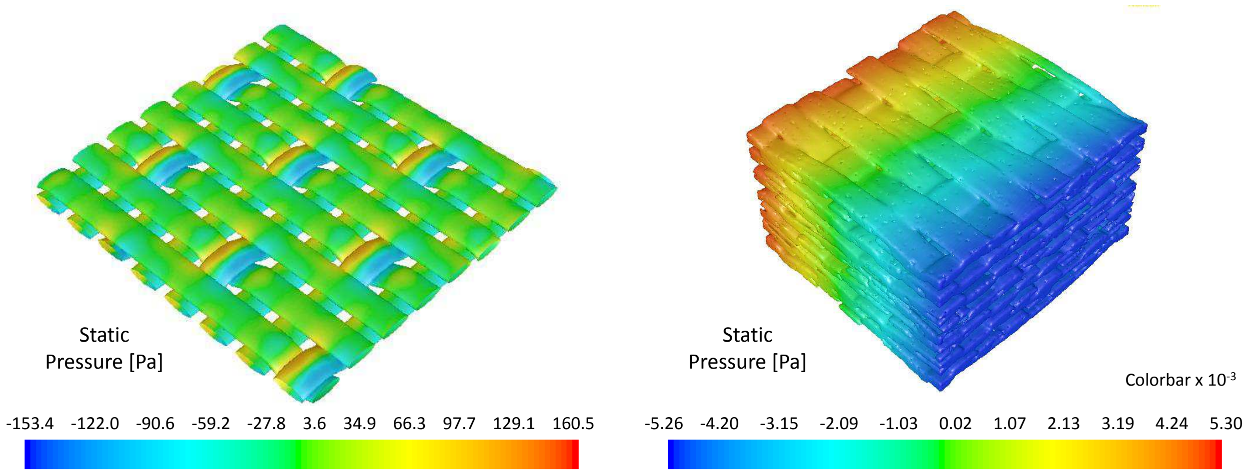

(a) (b)

Figure 2.4: (a) Pressure field obtained with the standard CFD approach and simplified geometry (impermeable textile, $\varepsilon_M = 0.5$). Pressure field obtained with the standard CFD approach and reconstructed real geometry.

2.3.3 Numerical solution

Two cases are considered: impermeable and permeable yarns. In the former case the governing equations are solved only in the complementary domain (i.e. outside the textile), while in the latter over the whole domain. The governing equations are the incompressible Navier-Stokes equations with an additional loss term in the second case:

$$\nabla \cdot \mathbf{v} = 0; \tag{2.1}$$

$$\rho \mathbf{v} \cdot \nabla \mathbf{v} = -\nabla p + \mu \nabla^2 \mathbf{v} + \mathbf{F}; \tag{2.2}$$

where ρ is the density, p the pressure, $\mathbf{v}$ the velocity vector, μ the dynamic viscosity of the fluid and $\mathbf{F}$ is the friction loss in the porous medium. The equations are solved by finite volume method using a second order upwind scheme for velocity and a second order interpolation scheme for pressure. The Semi-Implicit Method for Pressure-Linked Equations (SIMPLE) is adopted for the pressure-velocity coupling.

The viscous loss term **F** is given by well-established correlations for the transverse permeability of aligned fibers. Here we use one of the most employed, which was proposed by Gebart [23]:

$$\frac{K}{r^2} = C\left[\sqrt{\frac{1-\varepsilon_c}{1-\varepsilon}}-1\right]^{5/2}; \tag{2.3}$$

where r is the radius of the fiber, C a geometrical factor depending on the arrangement and ε_c the critical porosity (or percolation threshold). The author calculated $C = 16/9\pi\sqrt{2}$, $\varepsilon_c = 1 - \pi/4$ for square arrangements and $C = 16/9\pi\sqrt{6}$, $\varepsilon_c = 1 - \pi/2\sqrt{3}$ for hexagonal ones.

The effective permeability is then recovered by Darcy's law as:

$$\langle \mathbf{v} \rangle = -\frac{1}{\mu}\mathbf{K}\cdot\langle \nabla p \rangle\,; \tag{2.4}$$

where **K** is the permeability tensor. The principal values and orientation angle of the permeability tensor can be found considering the Darcy's law in matrix form:

$$\begin{Bmatrix} \langle v_x \rangle \\ \langle v_y \rangle \end{Bmatrix} = -\frac{1}{\mu}\begin{bmatrix} K_{xx} & K_{xy} \\ K_{yx} & K_{yy} \end{bmatrix}\begin{Bmatrix} \langle \partial_x p \rangle \\ \langle \partial_y p \rangle \end{Bmatrix}; \tag{2.5}$$

and defining a counter-clockwise rotation matrix around the angle θ as:

$$\mathbf{R} = \begin{bmatrix} cos(\theta) & -sin(\theta) \\ sin(\theta) & cos(\theta) \end{bmatrix}. \tag{2.6}$$

The permeability tensor for any angle θ can be written as:

$$\mathbf{K}_\theta = \begin{bmatrix} K_{xx} & K_{xy} \\ K_{yx} & K_{yy} \end{bmatrix} = \mathbf{R}^T\begin{bmatrix} K_1 & 0 \\ 0 & K_2 \end{bmatrix}\mathbf{R}; \tag{2.7}$$

where K_1 and K_2 are the principal values of permeability. Notice that $K_1 = K_2$ recovers the isotropic case. Here we adopt unidirectional injection technique [24]; therefore three simulations for each test case are necessary to recover the in-plane permeability ellipse, that is along the three directions $\theta = 0°$, $\theta = 45°$ and $\theta = 90°$.

Table 2.1: Comparison of the numerically predicted permeabilities for the simplified geometry (impermeable (I) and permeable (P) cases) and for the CMT-reconstructed geometry with the experimental data (K [m^2] and θ [°]).

Case	ε_M	ε_m	ϕ_{eff}	K_0	K_{45}	K_{90}	K_1	K_2	θ
Simpl. (I)	0.36	ε_m^c	0.60	1.57e-10	1.57e-10	1.56e-10	1.57e-10	1.55e-10	25.52
	0.50	ε_m^c	0.50	4.64e-10	4.63e-10	4.62e-10	4.64e-10	4.60e-10	11.60
Simpl. (P)	0.36	0.30	0.45	2.25e-10	2.25e-10	2.24e-10	2.26e-10	2.22e-10	27.78
	0.50	0.30	0.35	5.93e-10	5.93e-10	5.92e-10	5.93e-10	5.91e-10	22.50
CMT geom.	0.44	0.34	0.37	6.50e-10	7.20e-10	5.80e-10	7.29e-10	4.72e-10	34.48
Experim.	-	-	0.45	-	-	-	1.53e-10	1.01e-10	45.51
	-	-	0.39	-	-	-	2.24e-10	1.44e-10	48.72
	-	-	0.34	-	-	-	4.93e-10	3.35e-10	54.60

The principal components of the permeability tensor can then be computed from the permeabilities obtained along the three directions K_0, K_{45} and K_{90} as [24]:

$$K_1 = K_0 \frac{\alpha_1 - \alpha_2}{\alpha_1 - \frac{\alpha_2}{\cos(2\theta)}}; \tag{2.8}$$

$$K_2 = K_{90} \frac{\alpha_1 - \alpha_2}{\alpha_1 + \frac{\alpha_2}{\cos(2\theta)}}; \tag{2.9}$$

where $\alpha_1 = (K_0 + K_{90})/2$ and $\alpha_2 = (K_0 - K_{90})/2$. The orientation angle of the ellipse is computed as:

$$\theta = \frac{1}{2} \tan^{-1} \left(\frac{\alpha_1}{\alpha_2} - \frac{\alpha_1^2 - \alpha_2^2}{\alpha_2 K_{45}} \right). \tag{2.10}$$

2.3.4 Results and discussion

Let us first focus on the representative geometry (Fig. 2.4(a)). In order to guarantee creeping flow conditions, a Reynolds number based on the hydraulic diameter of the yarn $Re = \rho v d_h/\mu$ is fixed to 10^{-3}. Non-conformal periodic boundary conditions are imposed along the three principal directions, so that fully developed flow conditions are simulated. This choice is typical for the analysis of simplified representative elementary volumes. The pressure field over the textile for the impermeable case and $\varepsilon_M = 0.5$ is shown in Fig. 2.4(a) and the analysis is reported in Tab. 2.1.

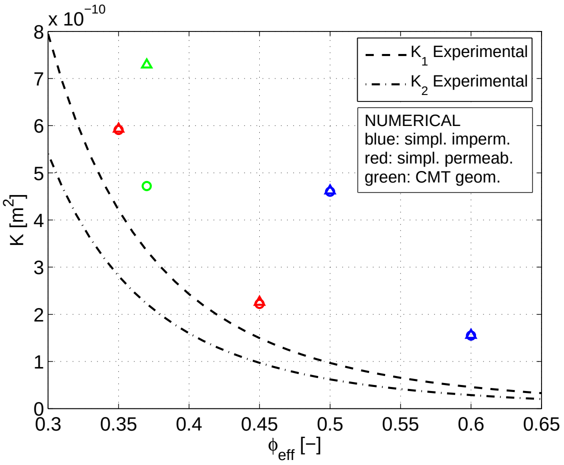

Figure 2.5: Comparison of the numerically predicted permeabilities for the simplified geometry (impermeable and permeable cases) and for the CMT-reconstructed geometry with the power law fit of the experimental data (K_1 triangles, K_2 circles).

The numerical results obtained for K_1 and K_2 in each case are compared with the power law fit of the experimental permeabilities in Fig. 2.5. The effective volume fraction ϕ_{eff} is computed as:

$$\phi_{\text{eff}} = 1 - (1 - \varepsilon_m)(1 - \varepsilon_M), \tag{2.11}$$

where in the impermeable case the microscopic porosity corresponds to the percolation threshold $\varepsilon_m^c = 1 - \pi/4$ (for square fiber arrangement). The comparison shows that the principal permeabilities are overestimated in all cases, while the permeable case provides better results. The anisotropy of the permeability tensor cannot be recovered, since we obtain $K_1 \cong K_2$, and therefore the experimental angle of the ellipse (between 45° and 55°) cannot be recovered.

The reasons can be found in the following uncertainties:

(a) the simplified geometry, which does not account for the real structure of the textile;

(b) saturated/unsaturated conditions for the experimental measurements;

(c) the lack of information on the micro- and macroscopic porosity ratio;

(d) the assumptions on the intra-yarn viscous resistance coefficients;

(e) the REV, which does not correctly account for experimental conditions;

(f) the deformation of the structure of the textile during the injection.

As regards the first issue (a), we run the simulations with the CMT-reconstructed REV (Fig. 2.4(b)). The effective volume fraction of the REV is $\phi_{\text{eff}} = 0.37$ (see Eq. (4.2)), while the macroscopic one is $\phi_M = 0.56$ (computed with the CAD software); thus the microscopic one is $\phi_m = 0.66$ (according to Eq. (2.11)). Notice that in this case the geometry is not periodic; therefore an inlet velocity is imposed to guarantee creeping flow conditions and no-slip conditions are imposed on the walls confining the seven layers. Symmetry conditions are imposed on the lateral boundaries. Three simulations are run to obtain K_0, K_{45} and K_{90}. The streamwise pressure drop is computed as the difference of the area-weighted mean static pressure between the inlet and outlet section for each case. For K_{45}, it is computed with the same strategy over the diagonal of the computational domain. The principal permeabilities and the angle of the ellipse obtained are: $K_1 = 7.29\text{e-}10\ \text{m}^2$, $K_2 = 4.72\text{e-}10\ \text{m}^2$ (Fig. 2.5) and $\theta = 34.50°$. The reconstructed geometry provides the possibility to recover the anisotropy of the principal permeability tensor and a better result for the orientation angle; however the permeabilities are still overestimated.

As regards issue (b), it has been shown that saturated or unsaturated conditions in the experimental measurements yield a significant scatter on the permeability data [10, 11]. Some authors found that saturated permeability is higher than the unsaturated one, other works report the opposite, while other authors report almost equal values (see [25] and references therein). These discrepancies are not fully understood and are usually attributed to experimental issues that could modify the saturated and unsaturated permeability ratio, such as mold deflection, capillary effect, microscopic flow, fiber channeling, and air bubbles [26]. The unsaturated permeability has been also found to be slightly affected by the test fluid [27].

With regards to issue (c), the estimation of micro- and macroscopic porosities for the modeling is not possible without an analysis of the structure such as that presented in this work by scanning electron microscopy or computed micro-tomography. Simplified relations may be considered or characteristic values assumed; however this information is required for any analyzed case. The porosity of the yarns and their structure results from the compression stage, thus simulation of the compression stage would be needed.

In order to address issue (d), transverse [23] and parallel [28, 29] permeability laws can be used to account for the anisotropy of the yarns. However, the anisotropy of fibers is of minor importance when the porosity of the yarns is very low, as in this case. Furthermore, if information on fiber topology is not available, correlations for aligned or disordered arrangements should be arbitrarily chosen and would not be representative of the real structure.

As regards issue (e), it is worth to point out that even if using the smallest representative elementary volume is the most employed approach, it does not allow to recover experimental conditions. Using a fully-periodic domain, fully-developed flow conditions are retrieved. However, by means of this approach the permeability is overestimated, also due to the fact that the viscous pressure loss at the walls is not accounted for. This latter issue is addressed with the CMT-reconstructed geometry; however the uncertainties remains, as shown. Experimental guidelines, indeed, foresee a minimum number of textile layers and a minimum size of the REV to be representative of the textile [11].

With regards to issue (f), the fiber dynamics is known to play a significant role in compaction and infiltration of fibrous media [16]. However, the problem is rarely addressed because the hierarchical structure of the textile requires non-standard modeling techniques, thus it is often neglected.

2.4 Summary and outlook

In this chapter, the permeability of an 8H Satin weave textile has been analyzed. A standard CFD approach has been adopted for the numerical prediction of the permeability. It has been found that using a simplified representative elementary volume allows to estimate the permeability in the same order of magnitude of the experimental one, however, the numerical predictions always overestimate experimental data. With this approach, the anisotropy of the principal permeability tensor obtained experimentally, cannot be recovered. As regards this latter issue, better results have been achieved using a virtually-reconstructed geometry, obtained by microtomographic data. Anisotropy in the principal permeabilities has been found; however the experimental angle of the ellipse cannot be recovered and the permeabilities are still overestimated.

The issues related to the uncertainties in the numerical prediction of the permeability of textiles have been discussed. The conclusion is that experimental data, such as an analysis by scanning electron microscopy of the textile or computed microtomography add valuable information on the structure of the textile, that can be used to tailor numerical simulations for a specific case. However, such an experimental analysis is not always available and anyway lacks of real predictive capabilities. Furthermore, the predictions obtained with the virtually-reconstructed geometry of the textile overestimated the experimental permeabilities. This suggests that the physics at the fiber scale plays an important role on the effective permeability of the textile and needs a better understanding.

Chapter 3

Compression of viscoplastic soft solids

3.1 Introduction

In this chapter, a numerical framework based on computational fluid dynamics for the squeeze flow of viscoplastic soft solids is developed. In order to validate the model, an epoxy-based material (i.e. an adhesive) is considered as test fluid. This material has been chosen because its rheological behavior is known to be well accounted by a viscoplastic constitutive model. Furthermore, the compaction of adhesives is of practical importance in a wide range of engineering situation where adhesive-bonding techniques are preferred to mechanical fastening.

The compressive forces resulting from the squeeze flow of a specimen of the material are analyzed by experimental, analytical and numerical means. The rheology is modeled according to a viscoplastic constitutive law (Herschel-Bulkley model), whose parameters are fitted with experimental data available from a characterization (on cylindrical specimens). An analytical solution is then generalized to be valid for any initial shape of the specimen (wedge-shaped in this chapter). A two-phase numerical model for the simulation of the squeeze flow is then proposed using the commercial CFD solver ANSYS Fluent. The numerical model is intended as an auxiliary tool, whose utilization in conjunction with the analytical law allows to correctly predict compressive forces for complex geometries of the specimen. In particular, the aim of this crossed analysis is to provide valuable information about the limits of each technique and about how to combine them to accurately predict compaction forces.

Figure 3.1: Experimental system used for the characterization and the squeeze-flow tests.

3.2 Experimental characterization

The squeeze tests were performed using the experimental set-up shown in Fig. 3.1. A squeeze tool, internally designed, was mounted in a MTS Universal Testing Machine (model Alliance RF100) [30]. The tests were conducted with two load cells: a 1 kN load cell for the tests on the cylindrical specimens and a 100 kN one for those on the wedge-shaped specimens. The tests were performed with a crossbeam velocity between 50 mm/min and 250 mm/min. The squeeze tool is based on guided parallel plates. The four vertical columns ensure a uniform distribution of pressure over the specimen. The lower aluminum plate is fixed to the frame plane, whilst the upper one is assembled to the mobile crossbeam of the universal machine. For the squeeze, a wooden block covered by kraftliner paper was mounted on the upper plate using bolts. In order to contain the lateral overflow of the material, for the wedge-shaped specimen additional aluminum profiles were added to the lower plate. The gap between these profiles and the wooden block was adjusted to guarantee a friction-free vertical movement. The adhesive samples were previously prepared on separate plates. The shape of the specimens (cylindrical or wedge-shaped) was obtained by firstly using a palette for a preliminary modeling and then accurately finished with a laser-cut steel. Each specimen was tested on its individual plane used for the preparation, which was correctly positioned and fixed to the universal machine. Force values were instantaneously recorded by TestWorks$^{\circledR}$4 [31].

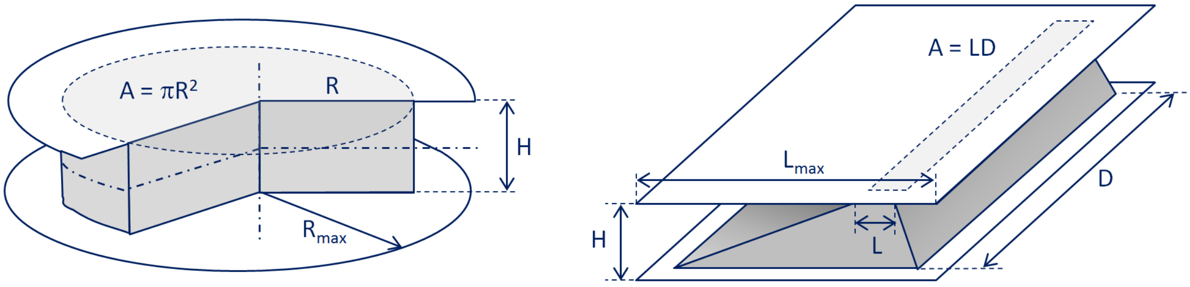

(a)

(b)

Figure 3.2: Schemes for the analytical solution: cylindrical (a) and wedge-shaped (b) geometries. The dimensions are: H ranges from 10 to 25 mm, L_{max} is 160 mm, R ranges from 15 to 30 mm and D ranges from 100 to 400 mm.

3.3 Generalized analytical solution

Analytical solutions for squeeze-flow are typically derived for cylindrical samples [32] as shown in Fig. 3.2 (a). For this case, the following conditions are considered: a constant velocity $V = -dH/dt$; an inter-plate volume $\pi R_{max}^2 H$, which is assumed to be always full of material and thus the contribution to the force of the overflow (when squeezing beyond R_{max}) is neglected; a rheology given according to the Herschel-Bulkley model, which in scalar form reads:

$$\tau = \tau_0 + K\dot{\gamma}^n; \tag{3.1}$$

being τ_0 the yield shear-stress threshold, K the consistency index and n the power-law index. This configuration has been previously studied [33, 34], particularly, Adams et al. [35] demonstrated that for no-slip boundary conditions at the walls and a plasticity number defined as $S = (RVK^{1/n})/(H^2\tau_0^{1/n})$, in the ranges $0 < S < 100$ and $0.1 < n < 1$ the mean pressure has the following form:

$$\bar{p} = \frac{F}{\pi R^2} = \sigma_0 + \frac{R\tau_0}{H}\left[\frac{2}{3} + \frac{2}{n+3}\left(\frac{2n+1}{n}\right)^n S^n\right]; \tag{3.2}$$

being σ_0 the uniaxial yield stress. It is typically assumed that $R/H >> 1$ and that the contribution of σ_0 is negligible as compared with $R\tau_0/H$, therefore the compressive force takes the following form:

$$F = \frac{2\pi R^3}{3H}\tau_0 + \frac{2\pi R^3 K}{(n+3)H}\left(\frac{2n+1}{n}\right)^n \left(\frac{RV}{H^2}\right)^n ; \tag{3.3}$$

However, these two simplifications must be avoided for generalizing the solution to arbitrary shapes of the sample, see for example Fig. 3.2 (b). For the generalization, the contact area must be a function of the contact length L. Thus, for cylindrical samples $L = R$ and the contact area is computed as $A = \pi L^2$. For wedge-shaped samples this contact area is $A = LD$. The definition of the generalized plasticity number S is then:

$$S = \frac{LV}{H^2}\left(\frac{K}{\tau_0}\right)^{1/n} ; \tag{3.4}$$

and the generalized expression for the compressive force follows from Eq. (3.2):

$$F = \sigma_0 A + \frac{2LA}{3H}\tau_0 + \frac{2LAK}{(n+3)H}\left(\frac{2n+1}{n}\right)^n \left(\frac{LV}{H^2}\right)^n + O\left(\frac{H}{L}\right)^2 . \tag{3.5}$$

The yield stress threshold is straightforwardly defined from the above equation in the limit of $V \to 0$ and neglecting σ_0 as:

$$\tau_0 = \frac{3HF}{2LA} . \tag{3.6}$$

When working at constant force, an expression for the velocity as a function of the force can be obtained from Eq. (3.5) and can be used to compute the separation height as a function of time as $H(t_n) = H(t_{n-1}) - V\delta t$, where the explicit expression for the squeeze velocity is (neglecting $O(H/L)^2$-terms):

$$V = \frac{H^2}{L}\left(\frac{n}{2n+1}\right)\left[\left(F - A\sigma_0 - \frac{2LA}{3H}\tau_0\right)\frac{(n+3)H}{2LAK}\right]^{1/n} . \tag{3.7}$$

Table 3.1: Fitting of the parameters for the Herschel-Bulkley model. V is the squeeze velocity [m/s], n the power-law index $[-]$ and K the consistency index $[Pas^n]$.

V	0.05	0.05	0.10	0.10	0.25	0.25	Mean	Std. Dev.
n	0.30	0.22	0.31	0.35	0.34	0.40	0.32	0.18
K	232.37	251.80	230.73	219.46	325.41	284.03	257.30	0.16

Making dimensionless the force F with the yield-stress force $(2LA\tau_0)/(3H)$ the dimensionless compressive force F^* is obtained, which is the result of three contributions:

$$F^* = F_s^* + F_n^* + F_h^*. \tag{3.8}$$

F_s^* is the dimensionless shear force:

$$F_s^* = 1 + \left(\frac{3}{n+3}\right)\left(\frac{2n+1}{n}\right)^n S^n; \tag{3.9}$$

which dominates at large S (and large L/H). F_n^* is a normal force arising from the uniaxial yield stress σ_0. Considering a Von Mises solid [34], $\sigma_0 = \sqrt{3}\tau_0$ and this force reads:

$$F_n^* = \frac{3\sqrt{3}}{2}\frac{H}{L}; \tag{3.10}$$

which is typically relevant in a transition region between $S = 1$ and $S \to 0$. The last force F_h^* encompasses all higher order terms, which are mainly related to surface-fluid interactions. These include slip effects, surface tension and any other surface potential related to, for example, electrostatic forces. This forces are expected to be relevant at small S or equivalently at small L/H and/or small shear rates ($\approx V/H$). To approximate the value of this force, we consider that in the regime of $S \to 0$ the flow is at small shear rates and thus in a Newtonian plateau and that there is full slip at the walls. Using this assumptions the following force is obtained [36]:

$$F_h^* = \frac{3}{2}\frac{K}{\tau_0}\left(\frac{H}{L}\right)^2. \tag{3.11}$$

Normal and higher-order forces are usually neglected in squeeze-flow analysis but they are the main forces involved when $L/H >> 1$, which occurs, for example, at the beginning of the compression of a geometry as the one in Fig. 3.2 (b).

The contact length in arbitrary geometries can be approximated as a weighted function between the initial and the maximum contact length, expressed as a function of the separation height H as:

$$L = \alpha \left(L_{max} - \frac{L_{max}}{H_{max}} H \right) + (1 - \alpha) L_{max}; \tag{3.12}$$

being α a geometric function defined as:

$$\alpha = \frac{1}{1 + exp\left[-\frac{H-\beta}{\gamma} \right]}. \tag{3.13}$$

The two fitting coefficients β and γ can be geometrically computed or fitted from CFD and/or experimental data.

3.4 Viscoplastic rheological model

The analytical solution given by Eq. (3.5), without normal and higher-order contributions, allows us to use the equipment described in Section 3.1 as a squeeze-flow rheometer. Thus, the parameters of the Herschel-Bulkley model, n, K and τ_0 in Eq. (4.3) are obtained by fitting experimental data. For these rheometric experiments, cylindrical test samples of 30 mm radius and 20 mm height are used. The material used is the Spabond 340LV Resin by Gurit [37]. The experiments were carried out in a range of room temperatures between 294 and 296 K. We first performed two creeping experiments at constant force (196 and 412 N) to obtain the yield stress from Eq. (3.6). The mean value obtained for the yield stress was 372.9 Pa with a standard deviation of 11%. Setting the yield stress to this mean value six experiments at constant velocity were performed (see Table 3.1) to adjust the values of n and K to experimental data using Eq. (3.5), without normal and higher-order contributions. The regression coefficients for all cases are $R^2 > 0.99$. The mean values obtained were $n = 0.324$ with a standard deviation of 18% and $K = 257.30$ with a standard deviation of 16%. The use of the squeeze flow rheometer is especially appropriate for the compression of adhesives, as long as the flow has the same shear rate values and history as in the compression of the adhesive in real geometries.

3.5 Numerical fluid-dynamic model

The experimental set-up employed for the characterization of the epoxy-based adhesive is reproduced using the two-dimensional computational domain shown in Fig. (3.3). The domain consist in a compression chamber, enclosed between two parallel walls. All the boundaries are static, except for the upper central wall, which is used for the compression. The adhesive is modeled as secondary phase and squeezed in the central (thinner) zone of the domain, using the dynamic mesh technique. The multi-phase model adopted is the Volume-Of-Fluid (VOF) method. In this approach a single momentum equation is shared between the phases, therefore the conservation of mass and momentum for the system is given by the incompressible Navier-Stokes equations as:

$$\nabla \cdot \mathbf{v} = 0; \tag{3.14}$$

$$\rho \left(\frac{\partial \mathbf{v}}{\partial t} + \mathbf{v} \cdot \nabla \mathbf{v} \right) = -\nabla p + \eta \nabla^2 \mathbf{v}; \tag{3.15}$$

being ρ the density, p the pressure, $\mathbf{v}$ the velocity and η the dynamic viscosity. The tracking of the interface between the primary (air) and secondary phase (adhesive) is achieved by the solution of a volume fraction equation, which allows Eq. (3.15) to be shared by the phases through the properties ρ and η. For the j-th phase the continuity equation reads:

$$\frac{1}{\rho_j} \left[\frac{\partial}{\partial t} \left(\phi_j \rho_j \right) + \nabla \cdot \left(\phi_j \rho_j \mathbf{v}_j \right) = S_{\phi_j} + \sum_{i=1}^{n} \left(\dot{m}_{ij} - \dot{m}_{ji} \right) \right]; \tag{3.16}$$

with the first term on right-hand side being a volumetric source and the second the mass transfer balance between the j-th and the other phase(s). In this case these two term are zero. The rheology of the adhesive is given by the Herschel-Bulkley model (Eq. 3.1), through the viscosity as:

$$\dot{\gamma} < \dot{\gamma}_{cr} : \eta = \frac{2 - \frac{\dot{\gamma}}{\dot{\gamma}_{cr}}}{\dot{\gamma}_{cr}} \tau_0 + K \left[(2-n)(n-1) \frac{\dot{\gamma}}{\dot{\gamma}_{cr}} \right]; \tag{3.17}$$

$$\dot{\gamma} > \dot{\gamma}_{cr} : \eta = \frac{\tau_0}{\dot{\gamma}} + K \left(\frac{\dot{\gamma}}{\dot{\gamma}_{cr}} \right)^{n-1}; \tag{3.18}$$

being $\dot{\gamma}_{cr}$ a critical shear rate. The equations are solved imposing pressure boundary conditions on the left and right vertical exits, no-slip on the walls. The numerical solution is carried out by finite volume method using the commercial CFD solver ANSYS Fluent® v14.0.

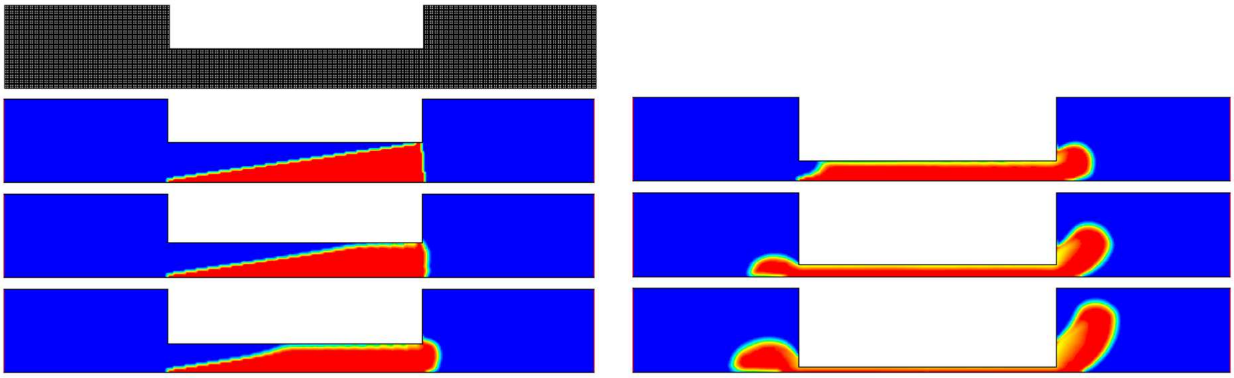

Figure 3.3: Computational mesh and time evolution of the fluid-dynamic solution for the squeeze-flow of the wedge-shaped specimen with $V = 50$ mm/min.

We adopt a third order discretization scheme (MUSCL) for momentum and the PRESTO scheme for pressure. The Semi-Implicit Method for Pressure Linked Equations (SIMPLE) is used for the pressure-velocity coupling and the transient scheme is first order implicit.

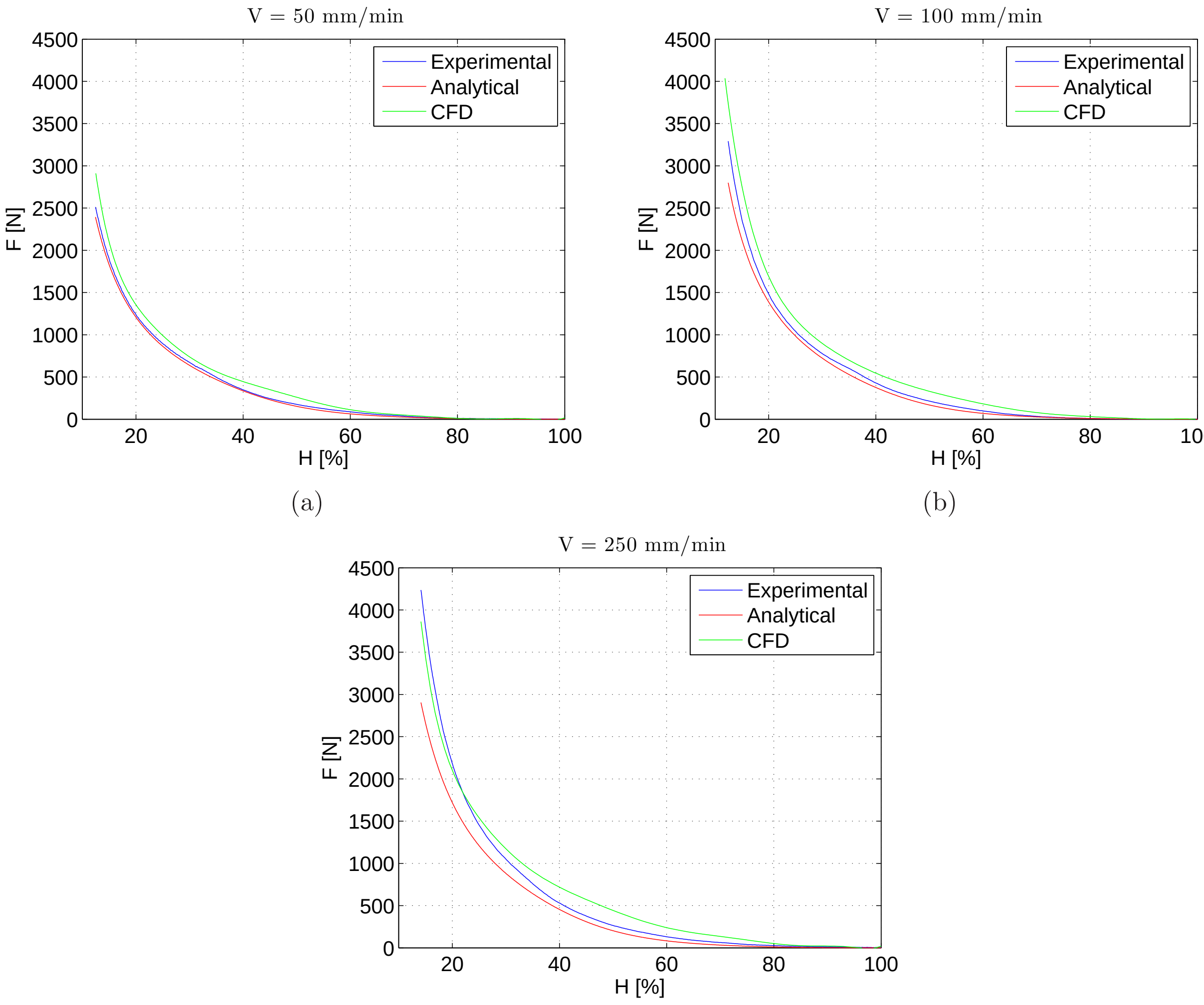

(a)

(b)

(c)

Figure 3.4: Comparison of analytical and numerical solutions with experimental data for the squeeze-flow test at constant velocity. The experimental data and numerical solutions are least-square fitted.

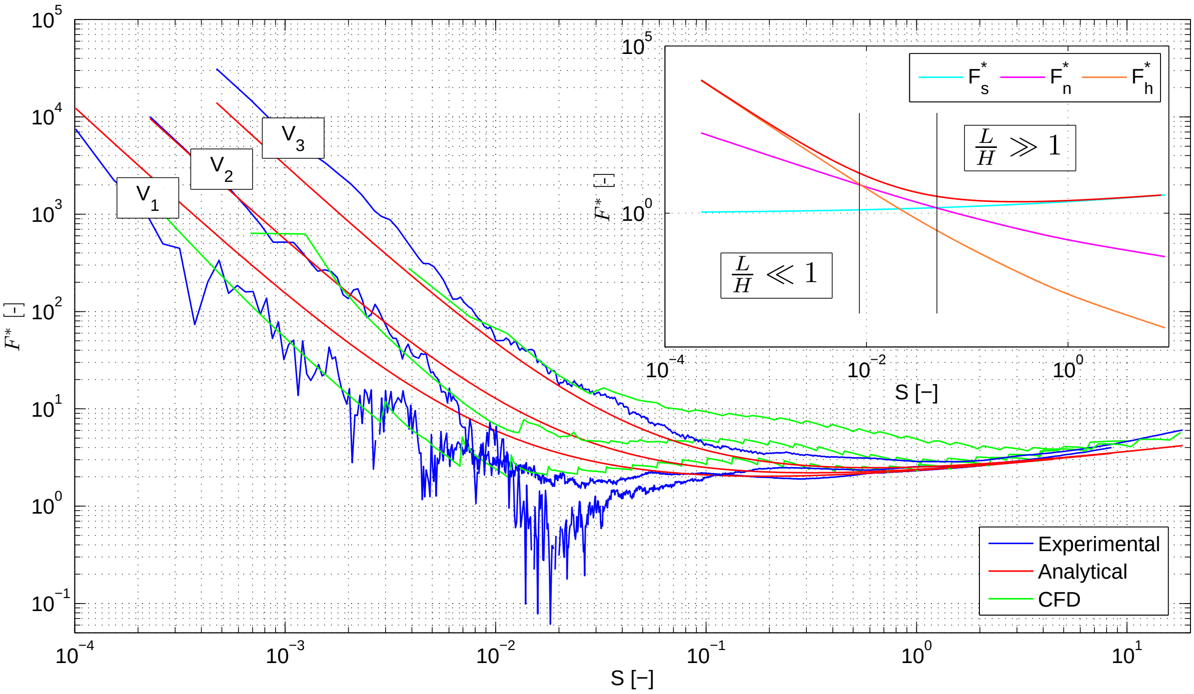

Figure 3.5: Comparison of the dimensionless analytical and numerical solutions with experimental data for $V_1 = 50$ mm/min, $V_2 = 100$ mm/min and $V_3 = 250$ mm/min . Inset: decomposition of the analytical solution F^* for $V_2 = 100$ mm/min (red) in its contributions. For $L/H \gg 1$ the flow regime is shear-dominated, while for $L/H \ll 1$, the flow regime is dominated by $O(L/H)^2$-order forces. In the transition region normal forces prevail.

3.6 Results and discussion

Experimental and numerical tests at constant velocity have been conducted and compared to the analytical solution. Dimensional results are reported in Fig. 3.4. The comparison shows a very good agreement for all cases. The final thickness of the adhesive can be computed by Eq. (3.6) using the force, the contact area and the yield stress of the adhesive. An additional dimensionless comparison provides insight into the origin of forces during the squeeze-flow process, see Fig. 3.5. It can be observed that there are three regimes, each one dominated for one of the contributed forces in Eq. (3.8). The $S > 1$ limit is well recovered by the two approaches. In the $S \to 0$ limit both CFD simulations and experimental results show significant oscillations around the expected analytical force. This is due to the nature of forces involved in this regime (i.e. surface tension, wall friction) that are all of the same order and

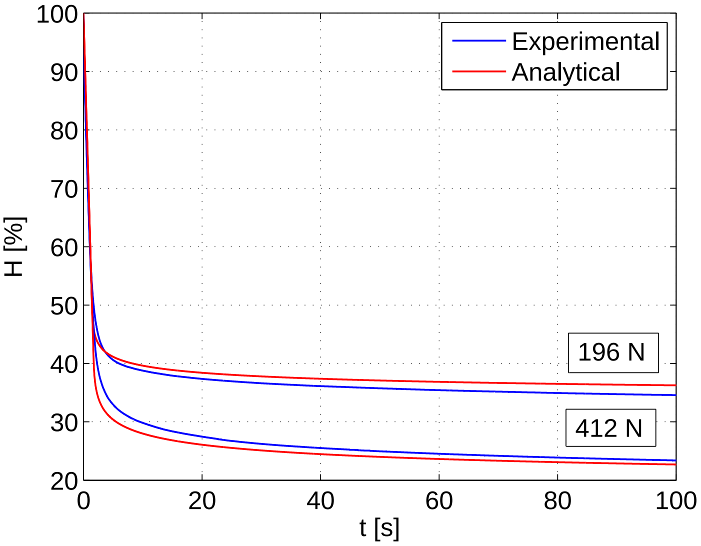

Figure 3.6: Comparison of the analytical solution with experimental data for the squeeze-flow test at constant force.

interplay, giving a dynamical behavior which has a non-trivial analytical characterization. The real interplaying forces are not exactly the same as in CFD simulations because these latter are also affected by numerical diffusion of the interphase in this stage, but they are anyway of the same order of magnitude. The intermediate regime, in which the normal forces prevail, is not properly recovered by CFD simulations. The reason is that the yield stress is not defined in the same way. In the analytical solution we deal with a Von Mises yield criterion but in the CFD simulation the yield criterion is defined by τ_0 and $\dot{\gamma}_{cr}$. A Von Mises yield criterion or advanced pressure-dependent Drucker-Prager one are not usually implemented in CFD with non-Newtonian rheologies as the conversion from a displacement formulation to a velocity one requires the use of advanced models for the transport of the stress.

Additional tests at constant force were carried out, but only experimental and analytical results are reported in Fig. 3.6. CFD simulations at constant force for $S < 1$ are difficult to carry out because of the oscillation of forces, as seen in the dimensionless analysis, which makes the simulation unstable.

3.7 Summary and outlook

An analytical model for squeeze forces occurring during compaction of viscoplastic materials has been proposed. The analytical solution has been generalized to be valid for any initial shape of the specimen before its squeeze. A two-phase numerical model of the squeeze-flow test has been also proposed. The results obtained with the two approaches showed excellent agreement with experimental data available for a wedge-shaped geometry of the specimen. The proposed numerical solution can then be seen as an auxiliary tool to be used in conjunction with the analytical solution for the prediction of forces in complex geometries.

The analysis and decomposition of the analytical solution in its various contributions, provides informations on good-engineering practices to apply when performing CFD simulations of this kind of flows. Particularly, CFD techniques are useful when working at $S > 1$, otherwise forces can be obtained more efficiently from the analytical expression. If simulations for $S < 1$ are needed, it is suggested to elaborate further on surface forces and on yield criteria.

The analytical model developed can be further improved in several ways. For example, in order to take into account the effect of roughness in thin geometries, the following modeling approaches have been previously adopted [38]: the use of an effective location of straight walls, the use of slip conditions, the use of an effective viscosity or the use of a representative porous-media layer. Another point that could be improved is the use of a temperature-dependent rheology, including the effects of an eventual curing. The latter would be particularly important when analyzing compression processes with temporal scales in the same range than those of curing.

Chapter 4

Compaction of fiber bundles

4.1 Introduction

In this chapter, the model developed for the squeeze flow of viscoplastic soft solids is applied for the analysis of the compaction of fiber bundles. In LCM, during the compaction in the mold, several textile layers are transversely compressed [11]. This results in a deformation mode which involves elastic deformation, nesting and inter-layer packing. The transverse compaction of entangled fibrous materials has been studied in considerable detail by the textile research community [39]; however in the framework of composite manufacturing it has received relatively little attention. The physics of the compaction is known to depend not only on the architecture of the fibrous reinforcement, but also on the processing parameters such as, for example, the compaction speed and dry or pre-impregnated conditions [40]. The non-linear mechanical behavior of entangled fibrous materials under compaction was first addressed by Van Wyk [41], who proposed a power-law expression for the response to load in the form:

$$p_c = c\phi^k; \tag{4.1}$$

where p_c is the applied pressure, ϕ the volume fraction, c and k material parameters. The model is essentially a non-linear elastic law, which can be used for a large variety of textiles by fitting the material parameters [42]. Equation (4.1) however, does not account for time-related effects, such as hysteresis and stress relaxation after loading [43]. Thus, more sophisticated viscoelastic models have been proposed [44] on the basis of a phenomenological analysis. From the numerical point of view, the most typical approach relies on the Finite Element Method (FEM), which is used to study the compaction at the textile-layer scale [45] or at the fiber scale [46]. For this latter case, alternative discrete simulation techniques have been also proposed [47]. A considerable effort has also been dedicated to describe the textile compaction in analytical frameworks, for a single textile layer [48] and for multiple layers [49].

In this work we propose a different framework for the analysis of the yarn compaction based on computational fluid dynamics (CFD). The yarn is modeled as a continuum soft solid using a viscoplastic constitutive equation, whose rheological parameters are obtained by fitting the experimental compression curve. For this purpose, a simplified analytical model for the evolution of the shape of the yarns is considered [48], which yields the rheology at the yarn scale through the fit and information about the evolution of the volume fraction under compaction. The resulting multi-phase model is solved numerically by computational fluid dynamics, using the commercial solver ANSYS Fluent®.

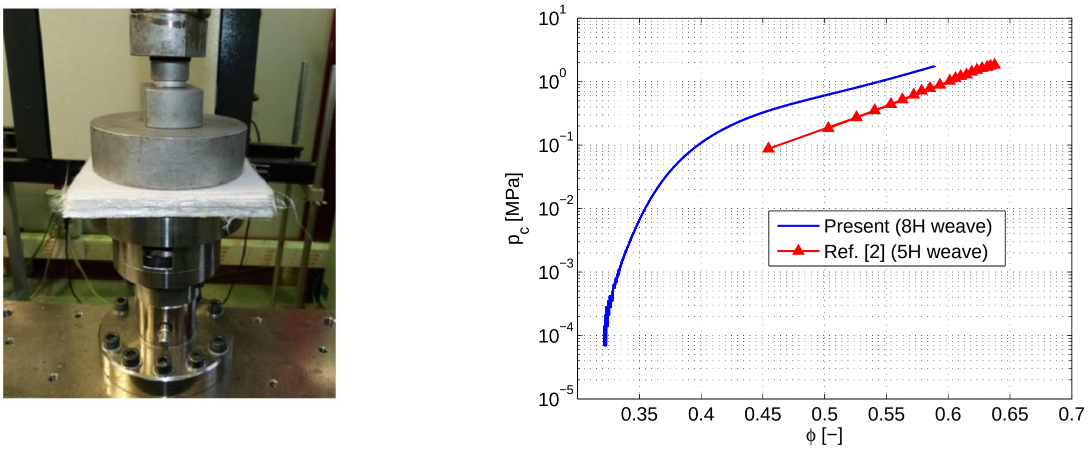

(a) (b)

Figure 4.1: (a) Experimental set-up for the textile compaction test. (b) Obtained experimental compression curve compared with the dry compression of a 5H weave (20 plies) [2].

4.2 Experimental characterization

The compression curve for the textile characterization has been obtained by compressing various textile layers. The tests are performed using a universal testing machine MTS with maximum load of 100 kN [30]. The experimental set-up is shown in Fig. 4.1(a). The tests are performed by monitoring the displacement of the compression plate and the applied force, which yield the thickness of the textile layers as a function of the applied pressure. The compression velocity is 1 mm/min (constant) and the number of textile layers is 48, with an initial thickness of 15 mm. Using the diameter of the compression plates $D = 135$ mm, the fabric weight $w = 305$ g/m^2 and the fiber density $\rho_f = 2.46$ g/cm^3, the evolution of the effective volume fraction ϕ_{eff} as a function of the thickness d is:

$$\phi_{\text{eff}} = \frac{n_{plies} w}{d \rho_f}; \tag{4.2}$$

where n_{plies} is the number of textile layers and the thickness d is a function of the applied force, thus the compaction curve is obtained (see Fig. 4.1(b)). The data is compared with the dry compression of a 5 harness (5H) satin weave at the same velocity [2], where 20 plies were used.

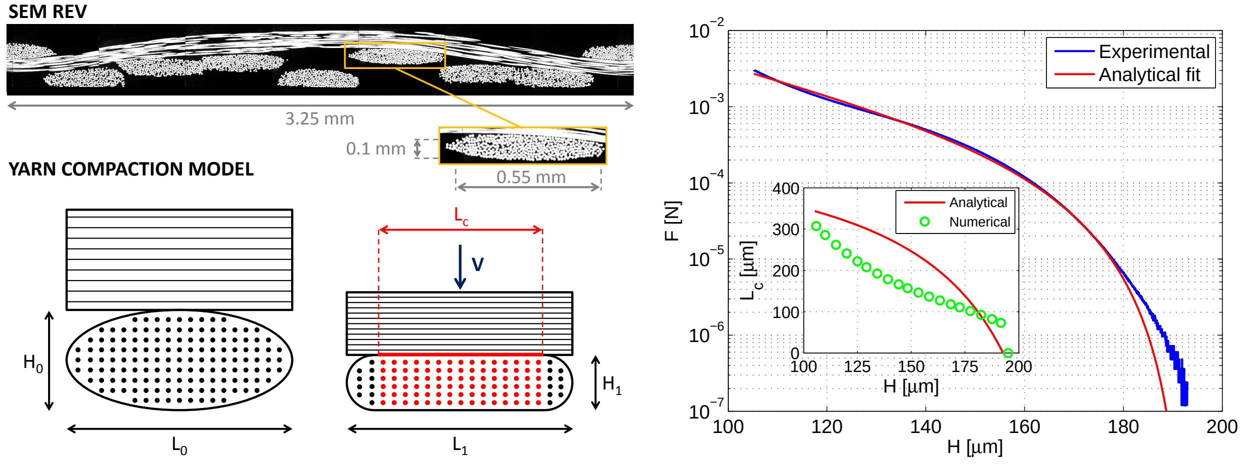

(a)

(b)

Figure 4.2: (a) Representative elementary volume (REV) extracted from a SEM image and schematic of the compaction model. (b) Compaction force at the yarn level as a function of the yarn height and fit of Eq. (4.4). In the inset, comparison of the evolution of the contact length as a function of the yarn height obtained with the CFD model with that from Eq. (4.5).

4.3 Theoretical model

The response to the compression of fibrous materials is known to be well accounted by a viscoplastic-type behavior [50]. Here we consider the quasi-static regime of compression, and the rheology is given by the Herschel-Bulkley model, which in scalar form reads:

$$\tau = \tau_0 + K\dot{\gamma}^n; \tag{4.3}$$

being τ_0 the yield stress threshold, K the consistency index and n the power-law index. The rheology is fitted to the experimental data using the generalized analytical solution for compressive forces of viscoplastic materials derived in Chapter 3 (neglecting normal and higher-order contributions):

$$F = \frac{2}{3}\frac{L_c A_c}{H}\tau_0 + \frac{2L_c A_c K}{(n+3)H}\left(\frac{2n+1}{n}\right)^n \left(\frac{L_c V}{H^2}\right)^n; \tag{4.4}$$

where L_c is the contact length, A_c the contact area, H the thickness of the material being squeezed and V the compression velocity. In order to fit the rheology, the evolution of the contact length and thus of the contact area must be known.

Let us then consider the compaction model shown in Fig. 4.2(a). The yarns are assumed to be of elliptical section, whose initial major and minor axes are respectively L_0 and H_0. At the beginning of the compression, we assume that: the contact length and area are zero (the perpendicular yarns are tangent); the fibers are aligned in a square configuration. A constant compression velocity $V = 1$ mm/min is applied and the yarns deform as shown in Fig. 4.2(a) on the right. It has been shown that the deformation of the yarn width due to the compressive force is generally small compared with the deformation of thickness [51]; therefore a reasonable assumption is $L_0 = L_1$ [48]. The contact area is a square which expands with the contact distance during the compression: $A_c = L_c^2$. The evolution of the contact distance between two yarns can be computed using an analytical solution for the deforming shape of the yarns [48]:

$$L_c = L_0 \left(1 - \frac{H}{H_0}\right) \left(\frac{4}{\pi} - \frac{H}{H_0}\right)^{-1}, \tag{4.5}$$

which is valid for $H/H_0 \leq 1$. In our case the yarn width can be obtained from the SEM images, $L_0 = L_1 = 550\ \mu$m (Fig. 4.2(a)), while the yarn height is computed using the distance between the compression plates and the number of yarns along the thickness (twice the number of plies): $H = d/2n_{plies}$. Notice that the initial thickness d_0 at the beginning of the compression yields H_0, while the final thickness d_1 yields H_1. In this case the initial thickness is 18.5 mm, thus $H_0 \cong 200\ \mu$m, while the final thickness is 10 mm, which yields $H_1 \cong 100\ \mu$m. The correctness of the estimated final yarn height is confirmed by the SEM image in Fig. 4.2(a). The resulting evolution of the contact distance as a function on the yarn height is shown in the inset of Fig. 4.2(b).

4.4 Fit of the rheological law

The rheology of Eq. (4.3) can be fitted using Eq. (4.4), considering that the contact area must be multiplied for the number of contacts among the yarns inside the specimen. The number of contacts can be computed from the area of the compression plate $A_{plate} = \pi D^2/4$ and the size of the REV ($L_{REV} = 3.25$ mm from Fig. 4.2(a)), as long as the number of warp and weft yarns in a REV is 8. Thus the number of contacts in the equivalent square area of the compression plate is:

$$n_c = n_{plies} \left(\frac{\sqrt{A_{plate}}}{L_{REV}} 8 \right)^2 ; \tag{4.6}$$

which yields the total contact area as $A_c^{tot} = A_c n_c$. For the sake of clarity, we remark that the contact area for the yarns that are in contact with the compressing plates spans the whole length of the yarns. However, the load applied is carried only by the fibers underneath the contact areas inside the specimen. This can be seen in Fig. 4.2(a), where the fibers that carry the load are those in the central zone of the yarn and are shown in red. Therefore, the volume fraction of fibers ϕ_m in the lateral zones remains unchanged during the compression, while in the central zone it increases as [48]:

$$\phi_m = \phi_{m_0} \frac{H_0}{H}; \tag{4.7}$$

where ϕ_{m_0} is the initial volume fraction before the compression. The fit of the analytical solution of Eq. (4.4) is shown in Fig. 4.2(b) and yields the coefficients for the Herschel-Bulkley model: $K = 9000$ Pas^n, $\tau_0 = 100$ Pa and $n = 1$ (Bingham fluid). Notice that, according to the definition given in Chapter 3 (Eq. 3.4), the plasticity number S ranges between 0 and 52.5, which is in the correct range for the analytical solution of Eq. (4.4), that is $0 < S < 100$.

4.5 Numerical fluid-dynamic model

The compression is simulated in ANSYS Fluent® using an available multi-phase model. The computational domain consists in a compression chamber, enclosed between two parallel walls. All the boundaries are static, except for the upper wall, which is used for the compression of the yarn. The yarn is modeled as a secondary phase and squeezed in the central zone of the domain, reproducing the compression between other two transversal yarns. The multi-phase model adopted is the Volume-Of-Fluid (VOF) method. In this approach a single momentum equation is shared between the phases; therefore the conservation of mass and momentum for the system is given by the incompressible Navier-Stokes equations as:

$$\nabla \cdot \mathbf{v} = 0; \tag{4.8}$$

$$\rho \left(\frac{\partial \mathbf{v}}{\partial t} + \mathbf{v} \cdot \nabla \mathbf{v} \right) = -\nabla p + \mu \nabla^2 \mathbf{v}; \tag{4.9}$$

being ρ the density, p the pressure, $\mathbf{v}$ the velocity and μ the dynamic viscosity. The tracking of the interface between the primary (air) and secondary phase (yarn) is achieved by the solution of a volume fraction equation, which allows Eq. (4.9) to be shared by the phases through the properties ρ and μ. For the j-th phase the continuity equation reads:

$$\frac{1}{\rho_j} \left[\frac{\partial}{\partial t} \left(\phi_j \rho_j \right) + \nabla \cdot \left(\phi_j \rho_j \mathbf{v}_j \right) = S_{\phi_j} + \sum_{i=1}^{n} \left(\dot{m}_{ij} - \dot{m}_{ji} \right) \right]; \tag{4.10}$$

where the first term on right-hand side is a source and the second the mass transfer between the phases. The rheology of the secondary phase (i.e. the yarn) is given by the Herschel-Bulkley model (Eq. (4.3)), through the viscosity as:

$$\dot{\gamma} < \dot{\gamma}_{cr} : \mu = \frac{2 - \frac{\dot{\gamma}}{\dot{\gamma}_{cr}}}{\dot{\gamma}_{cr}} \tau_0 + K \left[(2-n)(n-1) \frac{\dot{\gamma}}{\dot{\gamma}_{cr}} \right]; \tag{4.11}$$

$$\dot{\gamma} > \dot{\gamma}_{cr} : \mu = \frac{\tau_0}{\dot{\gamma}} + K \left(\frac{\dot{\gamma}}{\dot{\gamma}_{cr}} \right)^{n-1}; \tag{4.12}$$

being $\dot{\gamma}_{cr}$ a critical shear rate. The mass transfer between the phases is zero, while the evolution of the fiber volume fraction is modeled through the mass source term in the volume fraction equation (4.10).

From a phenomenological point of view, the secondary phase (the yarn) can be thought as the continuum description of the section of the fiber bundle in a suspending fluid (air). Therefore the density of the secondary phase before the compression is the weighted mean:

$$\rho = \phi_{m_0}\rho_f + (1 - \phi_{m_0})\rho_{air}. \tag{4.13}$$

When the fibers underneath the contact length compact, their volume fraction increases due to the reduction of air gaps between them, and the mass of the secondary phase decreases. This effect is modeled through the mass source term in Eq. (4.10) as:

$$S_{\phi_j} = -\frac{(1 - \Delta\phi_m)\rho_{air}}{\Delta t}; \tag{4.14}$$

being Δt the computational time step and $\Delta\phi_m$ the variation of the volume fraction between two consecutive time steps. The evolution of the volume fraction as a function of the yarn height is assumed to follow Eq. (4.7), where the yarn height is computed as:

$$H = H_0 - \Delta H = H_0 - Vt; \tag{4.15}$$

being t the simulation time. The contact length is computed on the upper wall of the domain at each time step as the total area of the cells whose value of the volume fraction is unitary. The contact length is then squared to obtain the contact area. The force is finally computed as the contact area times the normal stress on the wall (given by pressure and normal viscous contributions).

The equations are solved imposing pressure boundary conditions on the left and right vertical exits and no-slip on the walls. The numerical solution is carried out by finite volume method using the commercial CFD solver ANSYS Fluent® v14.0. We adopt a third order discretization scheme (MUSCL) for momentum and the PRESTO scheme for pressure. An implicit method is chosen for the volume fraction equation and a compressive scheme is applied to reduce the diffusion at the interphase. The Semi-Implicit Method for Pressure Linked Equations (SIMPLE) is used for the pressure-velocity coupling and the transient scheme is first order implicit.

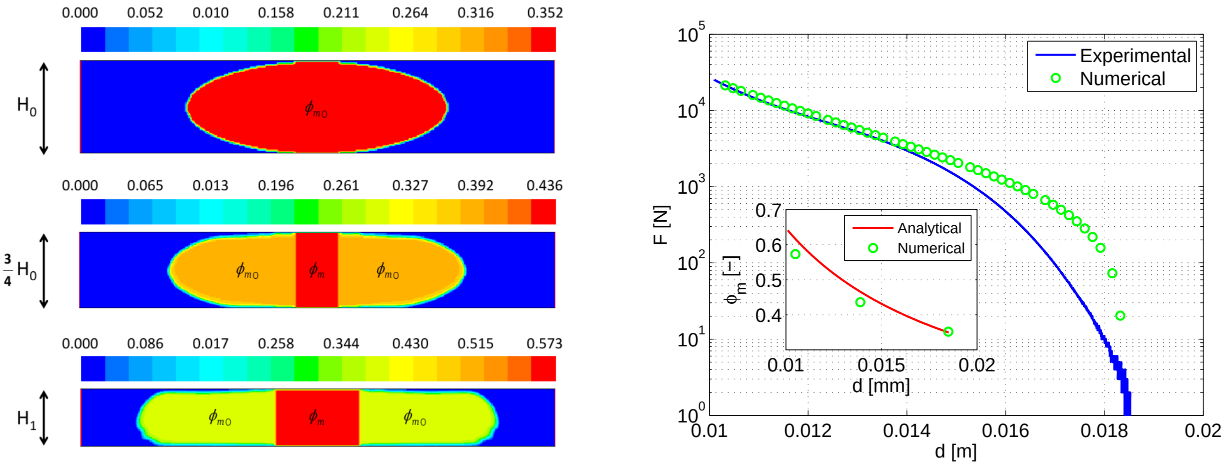

(a)

(b)

Figure 4.3: (a) Evolution of the fiber volume fraction during the compression according to the numerical model. (b) Comparison of the compaction force obtained with the CFD model with experimental data. In the inset, evolution of the fiber volume fraction ϕ_m according to the analytical model of Eq. (4.7).

4.6 Results and discussion

According to the yarn compaction model proposed, at the beginning of the compression the contact area is zero, which explains the difference between the analytical curve and the experimental data when the thickness of the yarns is very close to the initial value. However, the assumption on the initial contact area is a reasonable choice, since an initial value is difficult to estimate and would lead to non-univocal fitting curves. The scatter of the experimental data at this stage of the compression can be attributed to the higher-order forces discussed in Chapter 3, as, for example, electrostatic forces or stick-slip forces among the fibers.

The results obtained with the numerical model are shown in Fig. 4.3(a) for an initial volume fraction $\phi_{m_0} = 0.35$. The volume fraction ϕ_m evolves for the fibers underneath the contact length, while for those in the laterals zones it remains unchanged during the compression. The evolution of the contact length obtained is shown in the inset of Fig. 4.2(b), where a significant difference with the analytical model of Eq. (4.5) is observed. This discrepancy is due to the difficulty to properly recover the curvature of the yarn close to the upper wall on the computational mesh (Fig. 4.3(a)). The contact area indeed has a discontinuity at the beginning of the compression, which affects its subsequent evolution. This issue can be observed also in the compressive force. The compaction force for the whole specimen is obtained multiplying the force on a single yarn by the total number of contacts in the specimen (Eq. (4.6)). The force obtained numerically is compared with the experimental curve in Fig. 4.3(b), which shows that, at the beginning of the compression, the discontinuity in the contact length affects the evolution of the force. For high compression rates the force is very well recovered, which means that the difficulty in the CFD solution lies mainly in the discretization of the ellipse at the beginning of the compression. This issue also justifies the small discrepancy in the volume fraction between the numerical simulation and the input analytical of Eq. (4.7), shown in the inset of Fig. 4.3(b).

4.7 Summary and outlook

In this chapter, a phenomenological model for the analysis of the compaction of fiber bundles has been proposed. The yarn has been modeled as a viscoplastic soft solid, whose rheology has been obtained from experimental data using a simplified model for the evolution of the yarn shape. The proposed model addresses the analysis of the compaction of entangled fibrous materials in a non-conventional way, that is by computational fluid dynamics.

The results obtained are encouraging. The experimental compressive force yielded by the compaction test is very well recovered for high compression ratios. For low compression ratios, such as, at the beginning of the compression, the evolution of the contact area yielded by the CFD model significantly differs from the analytical model. This also affects the compressive force, which in this regime cannot be properly recovered. This issue has been found to be associated mainly with the discretization of the ellipse representative of the shape of the yarn in 2D. Indeed, if the aspect ratio of the ellipse is high, such as for the case considered, the curvature close to the compressive wall cannot be properly recovered on a Cartesian discretization (without using excessively fine meshes).

As further developments of the proposed model, it is suggested to consider shear-thickening behavior for the rheology of the yarns. This would allow, for example, to include information about friction among the fibers or stiffening effects due to out-of-plane constraints. The slip conditions at the walls (i.e. with the transversal crossing yarns) may be also studied as well as lateral contact between the yarns.

Chapter 5

Dilute viscoelastic suspensions

5.1 Introduction

In this chapter, the coupled method for the direct numerical simulation of mesoscopic suspensions is developed. The test fluid is a dilute viscoelastic suspension of polymeric molecules. One of the most commonly adopted practices for the simulation of these suspensions relies on macroscopic constitutive equations for the polymeric extra stress, derived from molecular models and solved via well-established numerical methods [52]. The advantage of this approach is the low computational cost associated, the drawback is that some kinetic models does not have a closed-form continuous counterpart. With regards to the finitely extensible non-linear elastic (FENE) model for example, a rheological law can only be derived under closure approximations, i.e. FENE-P, FENE-LS [53]. The resulting models are then able to phenomenologically describe the basic flow features but the underlying theoretical assumptions can hinder the retrieval of relevant viscoelastic phenomena.

In a more general modeling strategy, the kinetic origin of the molecular models is retained [54]. Methods using this approach are generally described as micro-macro models, due to the separated solution of the micro and macro scales. Continuity and momentum equations are solved using continuous equations (macro-scale) and kinetic equations are solved by stochastic or deterministic methods (micro-scale) [55]. In this framework, one of the most popular methodologies is the CONNFFESSIT approach, where a finite element solution of the macroscopic equations is combined with stochastic simulations for the dumbbell configuration [56]. One of the major issues concerned with this approach is the high computational expense and the embedded statistical noise, which can be filtered using variance reduction techniques [57].

Another similar and commonly used approach is the Brownian configuration field method [58]. This method already embeds efficient variance reduction, as long as individual molecules are clustered in continuous configuration fields according to their initial configuration and applied force, but the computational cost of the stochastic simulation is anyway a limit.

An alternative approach for noise reduction and faster computations consists in the solution of an equivalent Fokker-Planck equation for the probability density of the dumbbell configuration. However, a literature review reveals that due to the dimensionality of the problem and the lack of efficient numerical methods to solve the Fokker-Planck equation, little progress has been done in this framework [55] and no method prevail. Relevant recent work about the direct solution of the Fokker-Planck equation for complex flows relies on a Galerkin spectral element technique for 2D [59] and its extension to 3D [3]. Another group of promising methods are those that approximate the solution of the Fokker-Planck equation reducing the dimensionality of the problem. This order-reduction can be done *a priori*, like in the lattice-Fokker-Planck method [60], *on line* like in the proper generalized decomposition [61] or *a posteriori* like in the proper orthogonal decomposition [62]. All these techniques aim to systematically reduce the degrees of freedom and therefore the computational expense.

In this work we focus on direct deterministic numerical methods, therefore no approximation occurs beyond mesh resolution. The proposed approach relies on a previous work by Ammar [63] about a lattice Boltzmann solution of the Fokker-Planck equation for homogeneous flows. Recently this method has been also theoretically analyzed [64] and applied for the solution of a population balance equation [65] and for the Fokker-Planck equation [66]. However, none of the previous works [63–66] deals with the coupling of the kinetic solution with macroscopic fields, thus we investigate efficient ways to exploit it in multi-scale simulations.

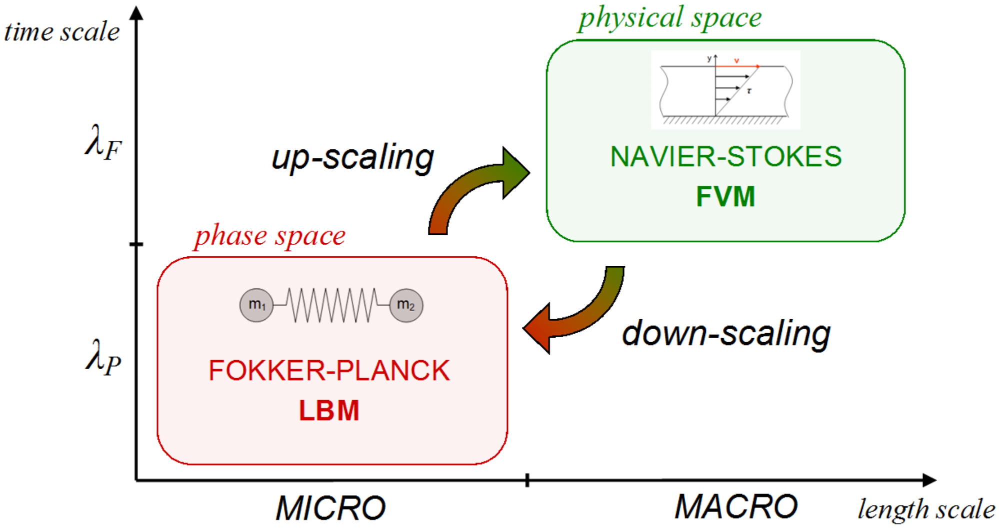

Figure 5.1: Overview of the proposed approach. λ_P and λ_F are the time-scales associated respectively with the polymer molecules and the viscosity of the solvent.

5.2 Theoretical model

5.2.1 Hydrodynamic system

Let us consider a polymeric solution as a blend between a Newtonian and a viscoelastic fluid. Assuming the flow to be incompressible and isothermal, mass and momentum conservation reads:

$$\nabla_x \cdot \mathbf{v} = 0; \tag{5.1}$$

$$\rho \frac{\partial \mathbf{v}}{\partial t} + \rho \mathbf{v} \cdot (\nabla_x \mathbf{v}) = -\nabla_x p + \nabla_x \cdot \boldsymbol{\sigma}; \tag{5.2}$$

where ρ is the density, p the pressure, $\mathbf{v}$ the velocity vector and the subscript x denotes operators in physical space. The total stress tensor $\boldsymbol{\sigma}$, embeds contributions from both the Newtonian solvent $\boldsymbol{\sigma}_s$ and the polymeric solute $\boldsymbol{\sigma}_p$, therefore $\boldsymbol{\sigma} = \boldsymbol{\sigma}_s + \boldsymbol{\sigma}_p$. Denoting by μ_s the dynamic viscosity of the solvent, $\boldsymbol{\sigma}_s$ is given as:

$$\boldsymbol{\sigma}_s = \mu_s \left(\nabla_x \mathbf{v} + (\nabla_x \mathbf{v})^{\dagger} \right) = \mu_s \dot{\boldsymbol{\gamma}}; \tag{5.3}$$

being $\dot{\boldsymbol{\gamma}}$ the rate of strain tensor. In order to close the hydrodynamic system, an additional material model must be solved for the viscoelastic contribution $\boldsymbol{\sigma}_p$.

5.2.2 Viscoelastic model

In the simplest micro-mechanical approach for polymer rheology, molecular chains are modeled by two beads and a spring connector, that is by a non-rigid dumbbell immersed in a fluid. A general kinetic model can then be derived considering the equations of motion of the beads in the dumbbell, namely the equilibrium of inertial, frictional, Brownian and connector forces [67]. For a j-th bead located in $\mathbf{r}_i$, the equilibrium yields the so called *Langevin* equation:

$$m_j \frac{d}{dt}\left(\frac{d\mathbf{r}_j}{dt} - \mathbf{v}\left(\mathbf{r}_j\right)\right) = \zeta_j \left(\frac{d\mathbf{r}_j}{dt} - \mathbf{v}\left(\mathbf{r}_j\right)\right) + \sigma \frac{d\mathbf{W}_j}{dt} + \mathbf{F}_j{}^c; \tag{5.4}$$

with m being the mass of the bead, ζ a drag coefficient, σ a coefficient for the standard Wiener process $\mathbf{W}$ and $\mathbf{F}^c$ the connector force. Indicating with k_B the Boltzmann constant and T the absolute temperature, $\sigma = \sqrt{2k_B\zeta T}$ from the principle of equipartition of energy [52]. Assuming high friction regime and thus over-dumped Brownian dynamics [68], the inertial term on the left-hand side can be dropped and, indicating with $\boldsymbol{\xi} = \mathbf{r}_2 - \mathbf{r}_1$ the end-to-end vector of a dumbbell, yields the following (Itô) stochastic differential equation:

$$\frac{d\boldsymbol{\xi}}{dt} = \boldsymbol{\kappa} \cdot \boldsymbol{\xi} - \frac{2}{\zeta}\mathbf{F}^c\left(\boldsymbol{\xi}\right) + \sqrt{\frac{4k_BT}{\zeta}}\frac{d\mathbf{W}}{dt}; \tag{5.5}$$

where $\mathbf{W}$ is a standard Brownian motion $\left(\mathbf{W}_2 - \mathbf{W}_1\right)/\sqrt{2}$ and the symbol $\boldsymbol{\kappa}$ has been adopted for the transpose of the velocity gradient tensor $\left(\nabla_x \mathbf{v}\right)^{\dagger}$. The peculiarity of the dumbbell model lies in the expression of the connector force law $H(\xi)$. In this work we are concerned with the finitely extensible non-linear elastic model, therefore indicating with h the spring constant and ξ_0 a finite extensibility parameter, the connector force reads:

$$\mathbf{F}^c\left(\boldsymbol{\xi}\right) = H(\xi)\boldsymbol{\xi} = \frac{h}{1 - ||\boldsymbol{\xi}||^2/\xi_0{}^2}\boldsymbol{\xi}; \tag{5.6}$$

with $||\cdot||$ indicating vector norm. This entropic force law, originally proposed by Warner [69], exhibits linear behavior for small extensions and the finite length ξ_0 in the limit of an infinite force. In a stochastic approach, Eq. (5.5) should then be stochastically solved for the dumbbell configurations in the random process $\mathbf{W}$.

Using stochastic analysis, the ordinary differential equation (5.5), can be associated with a partial differential equation for a probability density function (PDF), which can then be deterministically solved instead of a large number of realizations for the Brownian driver. In this case the resulting probability density function $\psi\left(\mathbf{x}, \boldsymbol{\xi}, t\right)$ satisfies the Fokker-Planck equation [70]:

$$\frac{\partial\psi}{\partial t} + \mathbf{v}\cdot\left(\nabla_x\psi\right) + \nabla_\xi\cdot\left[\left(\boldsymbol{\kappa}\cdot\boldsymbol{\xi} - \frac{2}{\zeta}\mathbf{F}^c\left(\boldsymbol{\xi}\right)\right)\psi\right] = \frac{2k_BT}{\zeta}\nabla_\xi^2\psi; \tag{5.7}$$

which is also called *Smoluchowski* equation in polymer science. Index ξ on operators indicates that they act in configuration space. Due to its dimensionality, the solution of Eq. (5.7) is non-trivial and we proceed as detailed in the next section.

5.2.3 Solution strategy

In order to solve the Fokker-Planck equation directly, we consider a time-splitting-like procedure similar to that proposed by Lozinski and Chauvière [59]. Following this idea, the operators acting in the configuration space are separated from those acting in the physical space. In this way Eq. (5.7) can be firstly solved in the configuration space for an intermediate distribution function ψ^{n^*}, which is then used for the solution in the physical space. We adopt a mixed explicit/implicit framework:

$$\frac{\psi^{n^*} - \psi^n}{\Delta t_\xi} = -\nabla_\xi\cdot\left[\left(\boldsymbol{\kappa}\cdot\boldsymbol{\xi} - \frac{2}{\zeta}\mathbf{F}^c\left(\boldsymbol{\xi}\right)\right)\psi^n\right] + \frac{2k_BT}{\zeta}\nabla_\xi^2\psi^n; \tag{5.8}$$

$$\frac{\psi^{n+1} - \psi^{n^*}}{\Delta t_x} + \mathbf{v}\cdot\left(\nabla_x\psi^{n+1}\right) = 0; \tag{5.9}$$

thus Eq. (5.7) reduces to an advection-diffusion equation in the configuration space (5.8) and an advection equation in physical space (5.9). Let us now firstly focus on Eq. (5.8): the space scaling is achieved considering a relaxation time $\theta = \zeta/4h$ and a dimensionless finite extensibility parameter $b = \xi_0^2 h/k_BT$, therefore $\boldsymbol{\xi}$ is made dimensionless with $\sqrt{k_BT/h}$, $\boldsymbol{\kappa}$ with θ^{-1} and time with θ, thus the resulting dimensionless equation reads:

$$\frac{\psi^{n^*} - \psi^n}{\Delta\hat{t}_{\hat{\xi}}} = -\nabla_{\hat{\xi}}\cdot\left[\left(\hat{\boldsymbol{\kappa}}\cdot\hat{\boldsymbol{\xi}} - \frac{1}{2}H(\hat{\xi})\hat{\boldsymbol{\xi}}\right)\psi^n\right] + \hat{\alpha}\nabla_{\hat{\xi}}^2\psi^n; \tag{5.10}$$

with the dimensionless diffusion coefficient being $\hat{\alpha} = 1/2$.

From now on, the convection vector of ψ in the configuration space (terms in round brackets on right-hand side of Eq. (5.10)) will be indicated with $\mathbf{u}$ for convenience. The reader should notice that the scaling of the velocity gradient tensor $\boldsymbol{\kappa}$ represents the link between the physical velocity field and the convection vector $\mathbf{u}$ through the relaxation time θ of the polymer. On the basis of this consideration, we define a microscopic (or local) Weissenberg number that will be used later, based on the second invariant of the rate of strain tensor as:

$$Wi_m := \theta \mathrm{II}_{\dot{\gamma}} = \theta \frac{1}{2}\Big[(\mathrm{tr}(\dot{\boldsymbol{\gamma}}))^2 - \mathrm{tr}(\dot{\boldsymbol{\gamma}}^2)\Big] \tag{5.11}$$

According to the adopted scaling, the connector force law $H(\xi)$ in Eq. (5.6) in dimensionless form reads as:

$$H(\hat{\xi}) = \Big[1 - ||\hat{\boldsymbol{\xi}}||^2/b\Big]^{-1}. \tag{5.12}$$

Equation (5.10) with the connector force law (5.12) is therefore the final dimensionless equation to be solved in the configuration space. We assume the dumbbells to be always laying in the same plane, therefore the configuration space is two-dimensional and the dumbbell extensibility domain (support of the PDF) results in a disc of radius $\sqrt{b}$. Equation (5.10) is solved for a solution of ψ^{n^*} for the local convection vector $\mathbf{u}$ at each point in a domain. The details about the numerical method together with its optimization will be extensively discussed later.

The obtained intermediate ψ^{n^*} should be convected in physical space by Eq. (5.9) according to the second stage of the operator-splitting procedure. However, we note that the convection of the full PDF in an Eulerian framework would require a prohibitively amount of data to be stored and transported. This issue can be overcome considering that the final target for the hydrodynamic system is the viscoelastic stress tensor. Therefore, we proceed by computing an intermediate stress tensor, which is convected in physical space in place of the relative distribution. Being $\langle\langle\cdot\rangle\rangle$ the ensemble averaging operator, the intermediate dimensionless viscoelastic stress tensor $\hat{\boldsymbol{\sigma}}_p^{n^*}$ is calculated from ψ^{n^*} using the Kramers expression [54]:

$$\hat{\boldsymbol{\sigma}}_p^{n^*} = \langle\langle H(\hat{\xi})\hat{\boldsymbol{\xi}} \otimes \hat{\boldsymbol{\xi}}\rangle\rangle - \mathbf{I} = \int_{||\hat{\boldsymbol{\xi}}||^2<b} \psi^{n^*}(H(\hat{\xi})\hat{\boldsymbol{\xi}} \otimes \hat{\boldsymbol{\xi}})d\hat{\boldsymbol{\xi}} - \mathbf{I}.$$

Applying the ensemble average to Eq. (5.9) yields:

$$\frac{\hat{\boldsymbol{\sigma}}_p^{n+1} - \hat{\boldsymbol{\sigma}}_p^{n^*}}{\Delta t_x} + \mathbf{v} \cdot \left(\nabla \hat{\boldsymbol{\sigma}}_p^{n+1}\right) = \mathbf{0}. \tag{5.13}$$

In the iterative solution adopted, this procedure is formally equivalent to the convection of the PDF before computing stresses. Furthermore, the conservation of stresses is analogous to the conservation of the second order moment of the distribution, which is actually the target quantity. The advantage of this approach is that the second stage for the solution of the Fokker-Planck equation (5.9), reduces to the convective transport of three scalar quantities, one for each component of the symmetric stress tensor.

Finally, the dimensionless stress tensor is scaled-up to its corresponding in the physical space, to serve as volumetric source term in the momentum equation (5.2). Indicating with n_c the number of polymer chains per unit volume, an equivalent polymer viscosity can be defined as $\mu_p = \theta n_c k_B T$ and the extra stress is scaled as [71]:

$$\boldsymbol{\sigma}_p = \frac{\mu_p}{\theta} \left(\frac{b+4}{b}\right) \hat{\boldsymbol{\sigma}}_p^{n+1}. \tag{5.14}$$

5.3 Numerical methods

5.3.1 Finite Volume Method

The macroscopic governing equations (5.1) and (5.2) and the transport of stresses (5.13) are solved by finite volume method (FVM). In this approach, transport equations are numerically solved on a discretized computational domain (mesh) and the conserved variables are calculated at cell centers. Partial differential equations are therefore converted to algebraic equations by integration about the cells (or control volumes), for example Eq. (5.2):

$$\int_{V_c} \rho \frac{\partial \mathbf{v}}{\partial t} dV + \oint \rho \mathbf{v} \cdot (\nabla_x \mathbf{v})\, d\mathbf{A} = \oint (-\nabla_x p + \nabla_x \cdot \sigma)\, d\mathbf{A}. \tag{5.15}$$

Equation (5.15) is then applied to each control volume and its neighboring cells in the domain, resulting in a system of algebraic equations with sparse coefficient matrix to be solved. Fluxes at cell faces, which are required for convective terms, can then be interpolated using several numerical schemes: we adopt a third order quadratic upwind scheme (QUICK) for momentum (5.2) and transport of stresses (5.13) and a second order scheme for pressure interpolation. The Semi-Implicit Method for Pressure Linked Equations (SIMPLE) is chosen for the pressure-velocity coupling. For the sake of clarity, we remark that despite the hyperbolic nature of Eq. (5.13), the solution is sufficiently smooth to be solved with a third order scheme. The interested reader can refer for example to [72] for details on the methods.

5.3.2 Lattice Boltzmann Method

The advection-diffusion equation for the FENE model (5.10) is solved by lattice Boltzmann method (LBM). This mesoscopic approach relies on the Boltzmann transport equation, whose discrete form in the Bhatnagar-Gross-Krook (BGK) approximation of the collision operator, reads as [73]:

$$f_i\left(\hat{\boldsymbol{\xi}} + \mathbf{c}_i \delta\hat{t}, \hat{t} + \delta\hat{t}\right) - f_i\left(\hat{\boldsymbol{\xi}}, \hat{t}\right) = -\frac{1}{\tau}\left(f_i\left(\hat{\boldsymbol{\xi}}, \hat{t}\right) - f_i^{eq}\left(\hat{\boldsymbol{\xi}}, \hat{t}\right)\right); \tag{5.16}$$

with $\delta\hat{t}$ being the time step, f_i the discrete particle distribution functions and $\mathbf{c}_i$ the associated microscopic velocity vectors.

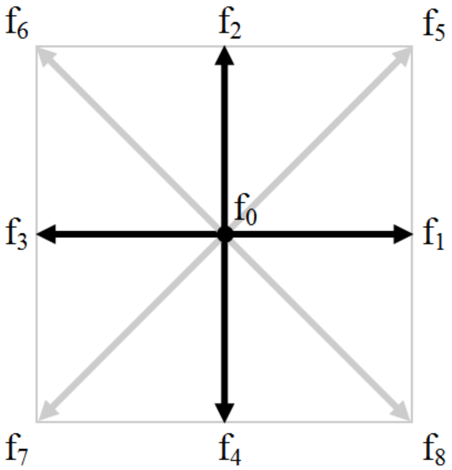

Figure 5.2: Lattices and relative discrete distribution functions: five links for D2Q5 (black color) and four additional links for D2Q9 (gray diagonals).

The equilibrium distribution function f_i^{eq} can be derived, for example, via second-order Taylor expansion in the Mach number of the Maxwell-Boltzmann equilibrium [74]:

$$f_i^{eq} = \left(1 + \frac{\mathbf{c}_i \mathbf{u}}{c_s^2} + \frac{(\mathbf{c}_i \mathbf{u})^2}{2c_s^4} - \frac{||\mathbf{u}||^2}{2c_s^2}\right) \omega_i \psi; \tag{5.17}$$

where c_s is the lattice speed of sound that, indicating with $\delta\hat{\xi}$ the lattice spacing and thus $c = \delta\hat{\xi}/\delta\hat{t}$ the lattice speed, is defined as $c_s = c/\sqrt{3}$. The reader should notice that in this case we retain the tilde notation for space and time for analogy with the equation being solved (5.10), but rigorously we should consider dimensionless lattice units. Macroscopic quantities can be recovered from the moments of the distribution function:

$$\psi = \sum_i f_i = \sum_i f_i^{eq}; \tag{5.18}$$

$$\psi \mathbf{u} = \sum_i \mathbf{c}_i f_i^{eq}; \tag{5.19}$$

$$\psi \left(\mathbf{u}\mathbf{u} + c_s^2 \mathbf{I}\right) = \sum_i \mathbf{c}_i \mathbf{c}_i f_i^{eq}; \tag{5.20}$$

which also allow to recover the macroscopic equation (5.10) and an expression for the lattice relaxation time by asymptotic expansion (Chapman-Enskog procedure) [63]. Let us drop the tilde notation for readability and denote with Ω_i the collision operator, that is, the terms on right-hand side of Eq. (5.16). Considering a 2-nd order Taylor expansion of the post-collision term (first term on the left-hand side), Eq. (5.16) yields:

$$\Omega_i\left(f\right) \approx \left(\partial_t + \nabla \cdot \mathbf{c}_i\right) f_i + \frac{1}{2}\left(\partial_t^2 + 2\partial_t \nabla \cdot \mathbf{c}_i + \nabla\nabla : \mathbf{c}_i\mathbf{c}_i\right) f_i. \tag{5.21}$$

Let us also consider the following expansions of the time derivative ∂_t and distribution function f_i in terms of a small formal number ϵ (spatial derivative is not expanded):

$$\nabla = \varepsilon \nabla_1 + O\left(\epsilon^2\right); \tag{5.22}$$

$$\partial_t = \epsilon \partial_{t1} + \epsilon^2 \partial_{t2} + O\left(\epsilon^3\right); \tag{5.23}$$

$$f_i = {f_i}^{eq} + \epsilon {f_i}^{(1)} + \epsilon^2 {f_i}^{(2)} + O\left(\epsilon^3\right). \tag{5.24}$$

Applying (5.23) and (5.24) in Eq. (5.21) yields the scale-separated form (5.25) and (5.26). Combining to get rid of higher order derivatives yields (5.27).

$$\left(\partial_{t1} + \nabla \cdot \mathbf{c}_i\right) {f_i}^{eq} = -\frac{1}{\tau\delta t}{f_i}^{(1)}; \tag{5.25}$$

$$\partial_{t2}{f_i}^{eq} + \left(\partial_{t1} + \nabla \cdot \mathbf{c}_i\right) {f_i}^{(1)} + \frac{\delta t}{2}\left(\partial_{t1} + \nabla \cdot \mathbf{c}_i\right)^2 {f_i}^{eq} = -\frac{1}{\tau\delta t}{f_i}^{(2)}; \tag{5.26}$$

$$\partial_{t2}{f_i}^{eq} + \left(1 - \frac{1}{2\tau}\right)\left(\partial_{t1} + \nabla \cdot \mathbf{c}_i\right) {f_i}^{(1)} = -\frac{1}{\tau\delta t}{f_i}^{(2)}. \tag{5.27}$$

Using now the 0-th order moment (5.18) and the condition (5.28) on the non-equilibrium distribution functions, yields (5.29) and (5.30):

$$\sum_i {f_i}^{neq} = \sum_i {f_i}^{(1,2)} = 0; \tag{5.28}$$

$$\partial_{t1}\psi + \nabla \cdot \left(\psi \mathbf{u}\right) = 0; \tag{5.29}$$

$$\partial_{t2}\psi + \left(1 - \frac{1}{2\tau}\right)\nabla \cdot \sum_i \mathbf{c}_i {f_i}^{(1)} = 0. \tag{5.30}$$

Recovering ${f_i}^{(1)}$ from Eq. (5.25), the sum in (5.30) becomes (5.31), rearranging (5.32):

$$\begin{aligned}\sum_i \mathbf{c}_i {f_i}^{(1)} &= -\,\tau\delta t \sum_i \mathbf{c}_i \left(\partial_{t1} + \nabla\cdot\mathbf{c}_i\right) {f_i}^{eq} \\ &= -\,\tau\delta t \left(\partial_{t1}\left(\psi\mathbf{u}\right) + \nabla\cdot\left[\psi\left(\mathbf{u}\mathbf{u} + c_s^2\mathbf{I}\right)\right]\right); \end{aligned} \tag{5.31}$$

$$\sum_i \mathbf{c}_i {f_i}^{(1)} = -\tau\delta t\Big(\mathbf{u}\left(\partial_{t1}\psi + \nabla\cdot\left(\psi\mathbf{u}\right)\right) + c_s^2\nabla\psi\Big). \tag{5.32}$$

Finally using (5.32) into (5.30) and reassembling scales, yields the final macroscopic equation:

$$\frac{\partial\psi}{\partial t} = -\nabla_\xi\cdot\left(\mathbf{u}\psi\right) + \delta t\left(\tau - \frac{1}{2}\right) c_s^2\nabla_\xi^2\psi; \tag{5.33}$$

that from the comparison with (5.7), gives the following expression for the lattice relaxation time (introducing again the tilde notation):

$$\tau = \frac{\hat{\alpha}}{\delta\hat{t}{c_s}^2} + \frac{1}{2}. \tag{5.34}$$

Given the advective-diffusive nature of Eq. (5.10), the numerical solution can be carried out on two lattice topologies, D2Q9 and D2Q5 (Fig. 5.2). The domain length l is imposed to be 20 percent larger then the domain of existence of the PDF, therefore indicating with N the number of nodes, the lattice spacing $\delta\hat{\xi}$ is given by l/N. The discrete velocities $\mathbf{c}_i$ and weights ω_i for the D2Q9 lattice are:

$$\mathbf{c}_i = \begin{cases}(0,0) & i=0\\ (\pm c,0),(0,\pm c) & i=1,2,3,4\\ (\pm c,\pm c) & i=5,6,7,8\end{cases} \qquad \omega_i = \begin{cases}4/9 & i=0\\ 1/9 & i=1,2,3,4\\ 1/36 & i=5,6,7,8\end{cases}$$

and for the D2Q5 lattice:

$$\mathbf{c}_i = \begin{cases}(0,0) & i=0\\ (\pm c,0),(0,\pm c) & i=1,2,3,4\end{cases} \qquad \omega_i = \begin{cases}1/3 & i=0\\ 1/6 & i=1,2,3,4\end{cases}$$

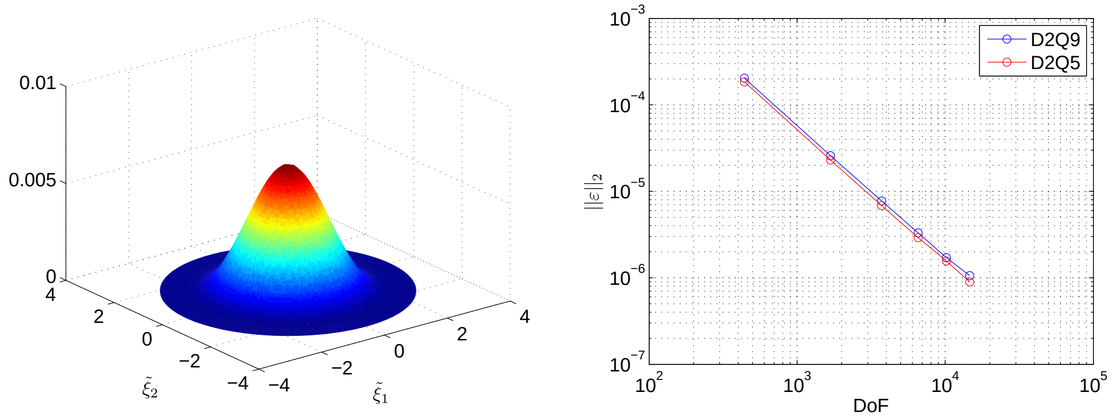

(a)

(b)

Figure 5.3: Shaded surface of the analytical equilibrium PDF (Eq. 5.35) on a 1,681 DoF lattice (a) and ℓ_2-*norm* convergence of ψ with $\tau = 0.55$ (b).

5.3.3 Coupled algorithm

The numerical solution of the coupled model has been carried out using the commercial CFD code ANSYS Fluent®. The lattice Boltzmann solution is called at cell centers as a sub-grid routine via compiled-C user defined function (UDF). The numerical procedure is as follows:

1. solution of the governing equations for $\mathbf{v}$ and p by FVM: Eq. (5.1) and (5.2);
2. sub-grid lattice Boltzmann solution of the FENE kinetic equation: Eq. (5.10);
3. computation of the local viscoelastic stress tensor: Eq. (5.13);
4. convective transport of the viscoelastic stresses by FVM: Eq. (5.13);
5. addition of the extra-stress to the momentum equation: (Eq. 5.2).

The procedure is iteratively repeated until global convergence. The internal convergence criterion for the FVM iterations (step 1 and 4 of the above algorithm) is a 10^{-8} residual, while for global convergence (between step 5 and 1 of the next loop) is 10^{-4}.

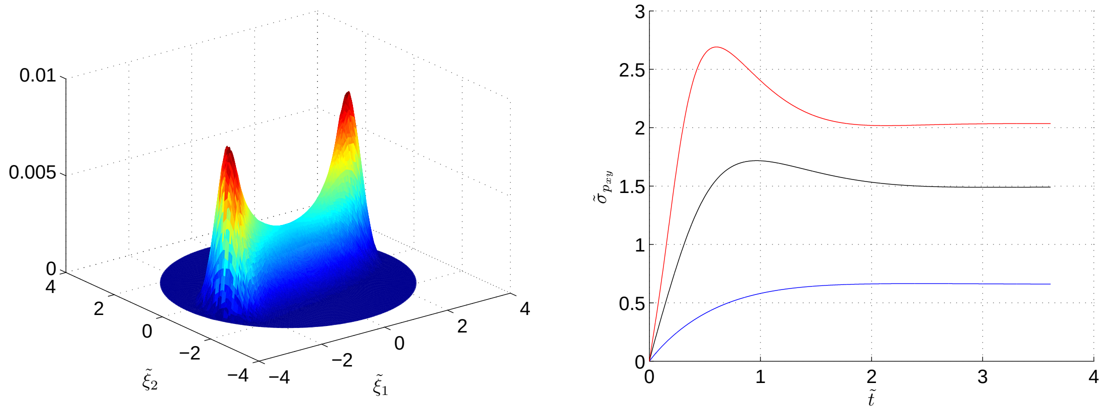

(a)

(b)

Figure 5.4: Start-up plane Couette flow: shaded surface of the equilibrium PDF for $Wi_m = 5$ on a 1,681 DoF lattice (a) and dimensionless shear stress evolution $\hat{\sigma}_{p_{xy}}$ for different Wi_m on a D2Q9 lattice with 3,721 DoF and $\tau = 0.55$ (b).

The standard test case of the viscoelastic flow around a confined cylinder (used for the validation, see Section 5.4.2) has a steady-state solution. Thus, a proper choice of the time steps, both in the configurational and physical space, is needed. The configurational-space time step Δt_ξ is the one needed to reach the steady state of the local viscoelastic stress, which is dynamically checked in each cell. It should be noticed that several internal time steps in lattice units $\delta\hat{t}$ are needed to reach Δt_ξ. The physical-space time step Δt_x is chosen in order to obtain an equilibrium between accuracy and performance, as done in other operator-splitting approaches [3].

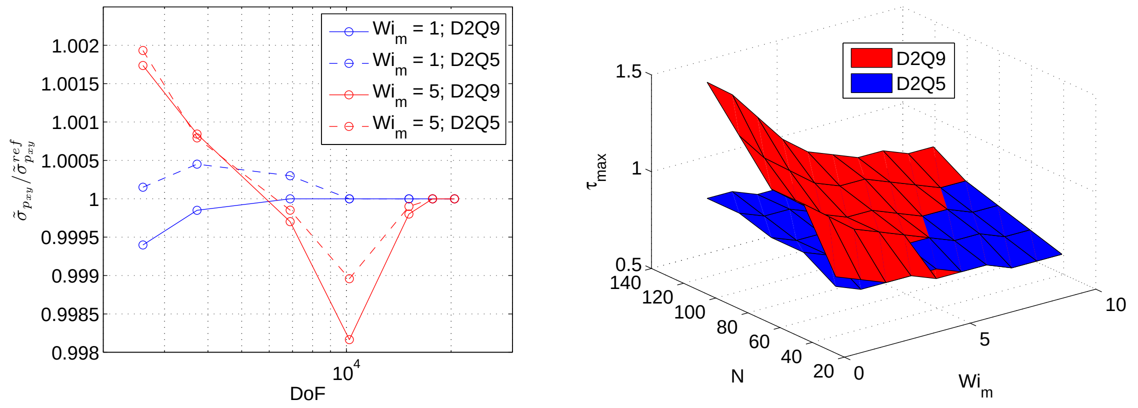

(a)

(b)

Figure 5.5: Error convergence for $Wi_m = 1$ and 5 on the two lattices (a) and stability map for D2Q9 and D2Q5 lattices (b).

5.4 Model analysis

5.4.1 Sub-grid solution

In this section, the indexes introduced in Section 5.2 are omitted for readability. We analyze the sub-grid solution of the Fokker-Planck equation by a lattice Boltzmann method in terms of: its relaxation towards equilibrium, evolution to steady-state solutions, numerical errors, stability range and computational time.

The relaxation of the probability density $\psi(\hat{\boldsymbol{\xi}}, \hat{t})$ to equilibrium is tested considering that for null velocity gradient $\hat{\boldsymbol{\kappa}}$, an analytical solution for Eq. (5.10) can be found in the form [63]:

$$\psi_{eq} = H(\hat{\xi})^{-b/2} \left[\int H(\hat{\xi})^{-b/2} d\hat{\boldsymbol{\xi}} \right]^{-1} ; \tag{5.35}$$

which for a dimensionless dumbbell extensibility $b = 10$ (constant throughout this chapter), yields the equilibrium distribution shown in Fig. 5.3(a).

Table 5.1: Comparison of the computational time [s] and relative numerical error [%] for the two lattices for $\tau = 0.55$ and $\tau = \tau_{max}$ (start-up plane Couette flow at $Wi_m = 5$).

stencil	**DoF = N^2**	**1,681**	**3,721**	**6,561**	**10,201**	**14,641**
D2Q9	$\tau = 0.55$	0.98	4.88	15.24	36.86	80.54
	$\tau = \tau_{max}$	0.33	0.87	2.48	4.63	8.43
	speed-up	3.0	5.6	6.1	8.0	9.6
	error	0.5357	-0.1933	-0.1538	-0.1690	-0.1092
D2Q5	$\tau = 0.55$	0.62	3.11	6.45	9.93	14.24
	$\tau = \tau_{max}$	0.2	0.63	1.93	3.92	7.03
	speed-up	3.1	4.9	3.4	2.5	2.0
	error	0.0764	-0.0594	-0.0297	-0.0347	-0.0198

Given an initial distribution function ψ_0 (constant in this case), satisfying the normality condition $\int \psi(\hat{\boldsymbol{\xi}})d\hat{\boldsymbol{\xi}} = 1$, the relaxation rate and error convergence are analyzed by an ℓ_2-*norm* with respect to the reference solution ψ_{eq} defined as:

$$||\varepsilon||_2 = \frac{1}{N}\sum_{k=1}^{N}\sqrt{\psi_{eq}^2 - \psi_{\hat{t}}^2}; \tag{5.36}$$

being $\psi_{\hat{t}}$ the distribution function at time $\hat{t}$. The convergence criterion for relaxation is a 10^{-8} residual calculated as backward finite difference on the norm. The analysis for the two lattices shows that the error of the 8-neighbors lattice is slightly larger than that of the 4-neighbors one (see Fig. 5.3(b)).

With regards to the analysis of non-null $\hat{\boldsymbol{\kappa}}$ gradient, we examine the time evolution of the shear stress $\hat{\sigma}_{p_{xy}}$ for a start-up planar Couette flow $[0, \hat{\kappa}_{xy}; 0, 0]$. The initial distribution function ψ_0 is in this case (as in the rest of the paper) given as Eq. (5.35). According to its definition (5.11), in this case the local Weissenberg number corresponds to the magnitude of the component $\hat{\kappa}_{xy}$ itself. The resulting steady-state PDF for $Wi_m = 5$ is shown in Fig. 5.4(a), while the stress evolution for varying Wi_m is shown in Fig. 5.4(b). The error analysis has been carried out for $Wi_m = 1$ and $Wi_m = 5$ and is shown in Fig. 5.5(a). To allow a proper visualization of the comparison, the shear stress has been normalized using the value obtained with the highest number of nodes $\hat{\sigma}_{p_{xy}}/\hat{\sigma}_{p_{xy}}^{ref}$ for each case. Notice as for a higher Wi_m the solution requires a higher number of nodes to converge, in particular for the D2Q9 lattice.

This behavior can be associated with the shape of the PDF at steady-state, that for lower Wi_m is closer to the initial condition. More details about error analysis of lattice Boltzmann methods for Fokker-Planck equations can be found in [63, 66].

An analysis of the stability domains for the two tested lattices has been also carried out for Wi_m in the range 1 to 10. The results show that the stability range of the D2Q9 is larger than that of the D2Q5 lattice in the region of low Wi_m and high DoF (Fig. 5.5(b)). Despite the increased stability, the error of the 8-neighbors lattice is also slightly larger than that of the 4-neighbors one (Fig. 5.5(a)).

Table 5.1 shows the comparison of the computational time required by the two lattices to converge to steady-state for the start-up plane Couette flow at $Wi_m = 5$, using the minimum relaxation time $\tau = 0.55$ and the maximum stable allowed on the basis of the stability map. The tested CPU is an Intel© Xeon© X5650 2.67GHz. The D2Q5 lattice requires less computational time due to the reduced number of links and therefore of computational operations, however the speed-up for the D2Q9, when moving from τ_{min} to τ_{max}, is greater due to the larger stability range. The relative numerical error introduced increasing the relaxation time for the two lattices is anyway always lower than 1% and the maximum speed-up achievable is nearly ten times for the D2Q9 lattice.

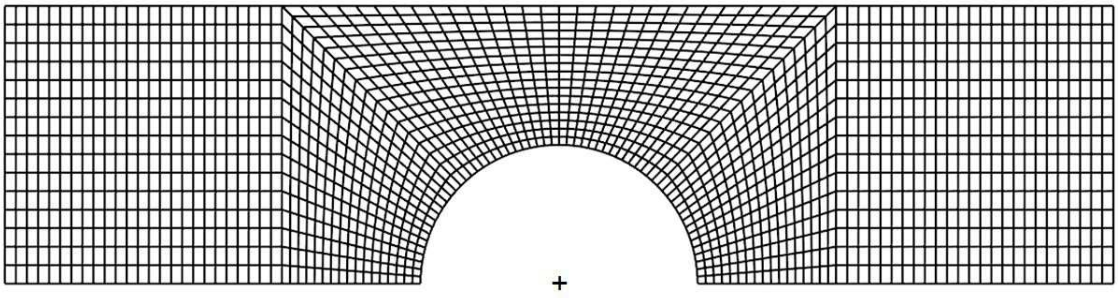

Figure 5.6: Mesh layout close to the cylinder surface (2 m length and 1,770 cells displayed).

5.4.2 Validation

The coupled model is validated against the benchmark problem of two-dimensional viscoelastic flow around a cylinder confined between two parallel plates [52]. In order to save in computational time, only half of the domain is studied and symmetry conditions are applied on the lower boundaries. The domain extent is 4 m length (L), 0.5 m height (H) and the hole is 0.25 m radius (R) centered in the origin. The ratio of the radius of the cylinder to the half-width of the channel (blockage) has been chosen to be $\Lambda = 0.5$ and the ratio of the solvent to the total zero-shear-rate viscosity is $\beta = \mu_s/(\mu_s + \mu_p) = 0.59$ [3, 71]. The mesh layout close to the cylinder surface is shown in Fig. 5.6, where only 2 m length and 1,770 cells are displayed to allow a proper visualization of the mesh layout. The boundary conditions are: stream-wise periodicity between inlet and outlet; no-slip for momentum and homogeneous Neumann for convection of stresses on the hole and upper boundary (walls). Indicating with v_{ref} the reference velocity at inlet (or outlet) of the periodic domain, we define for this problem a macroscopic (or global) Weissenberg and Reynolds number as:

$$Wi_M = \frac{v_{\text{ref}}}{R}\theta = \dot{\gamma}_{\text{ref}}\theta; \qquad Re_M = \frac{\rho v_{\text{ref}} R}{\mu}. \tag{5.37}$$

The Reynolds number is kept constant to 10^{-3} for steady-state creeping flow. In order to test the FVM mesh independence, the solution has been carried out on three different grids, respectively of 15,000 (M1), 25,000 (M2) and 40,000 (M3) cells for $Wi_M = 0.6$. The number of nodes and relaxation time for the sub-grid solution are $N = 128$ and $\tau = 0.8$ (D2Q5). The obtained profiles of dimensionless viscoelastic stresses on the symmetry plane and on the cylinder surface are consistent with those obtained by Chauvière and Lozinski [3] with a Galerkin

Table 5.2: Comparison of the calculated drag factor with the results obtained by Chauvière and Lozinski [3] for different Weissenberg number.

Wi_M	C_D^μ	C_D^μ [3]	C_D^p	C_D^p [3]	$C_D^{\sigma_p}$	$C_D^{\sigma_p}$ [3]	C_D	C_D [3]
0.6	6.2103	6.2248	1.9342	1.9980	0.6769	0.6696	8.8216	8.8925
0.9	5.8497	6.0175	1.9061	1.9953	0.5915	0.5393	8.3474	8.5521

spectral element method for the 2D case (Fig. 5.7). We also report the contours of dimensionless dumbbell elongations in the domain (Fig. 5.8) and of the dimensionless viscoelastic stresses (Fig. 5.9). These latter are reported also for the case $Wi_M = 0.9$ in Fig. 5.10. As further validation we compare a drag coefficient defined as follows:

$$C_D = \frac{F_x}{4\pi R(\mu_s + \mu_p)v_{\text{ref}}}; \tag{5.38}$$

with F_x being the total drag force on the cylinder surface (with polar angle ϑ):

$$F_x = 2\int_0^\pi \left[\left(-p + 2\mu_s\frac{\partial v_x}{\partial x} + \sigma_{pxx}\right)\cos\vartheta + \left(\mu_s\left(\frac{\partial v_y}{\partial x} + \frac{\partial v_x}{\partial y}\right) + \sigma_{pxy}\right)\sin\vartheta\right] R d\vartheta. \tag{5.39}$$

In order to compare the results with those obtained by Chauvière and Lozinski [3], the drag factor C_D is split into pressure C_D^p, viscous C_D^μ and viscoelastic contributions $C_D^{\sigma_p}$. The analysis (Table 5.2) show very good agreement for $Wi_M = 0.6$, the relative error on the total drag factor is below 1%. On the other hand, for $Wi_M = 0.9$ the error is around 2.5%. We noticed that despite a converged solution can be achieved with increasing Wi_M, the accuracy decreases. The cause of this decrease in accuracy can be sought in the discretization of the PDF in cartesian coordinates with the lattice-Boltzmann method and on the choice of the time-step. In this work we limit the maximum Wi_M to 0.9 and leave a deeper analysis of this issue for future work.

The sub-grid solution can be called from Fluent® via user defined function implementation and eventually parallelized on multiple processors. For computational efficiency, we use an accelerated version running on graphic card (GPU). The GPU is less flexible on the choice of the number of nodes, but provides remarkable acceleration: in this case the speed-up reaches nearly 50x with respect to the CPU (see Appendix A for details).

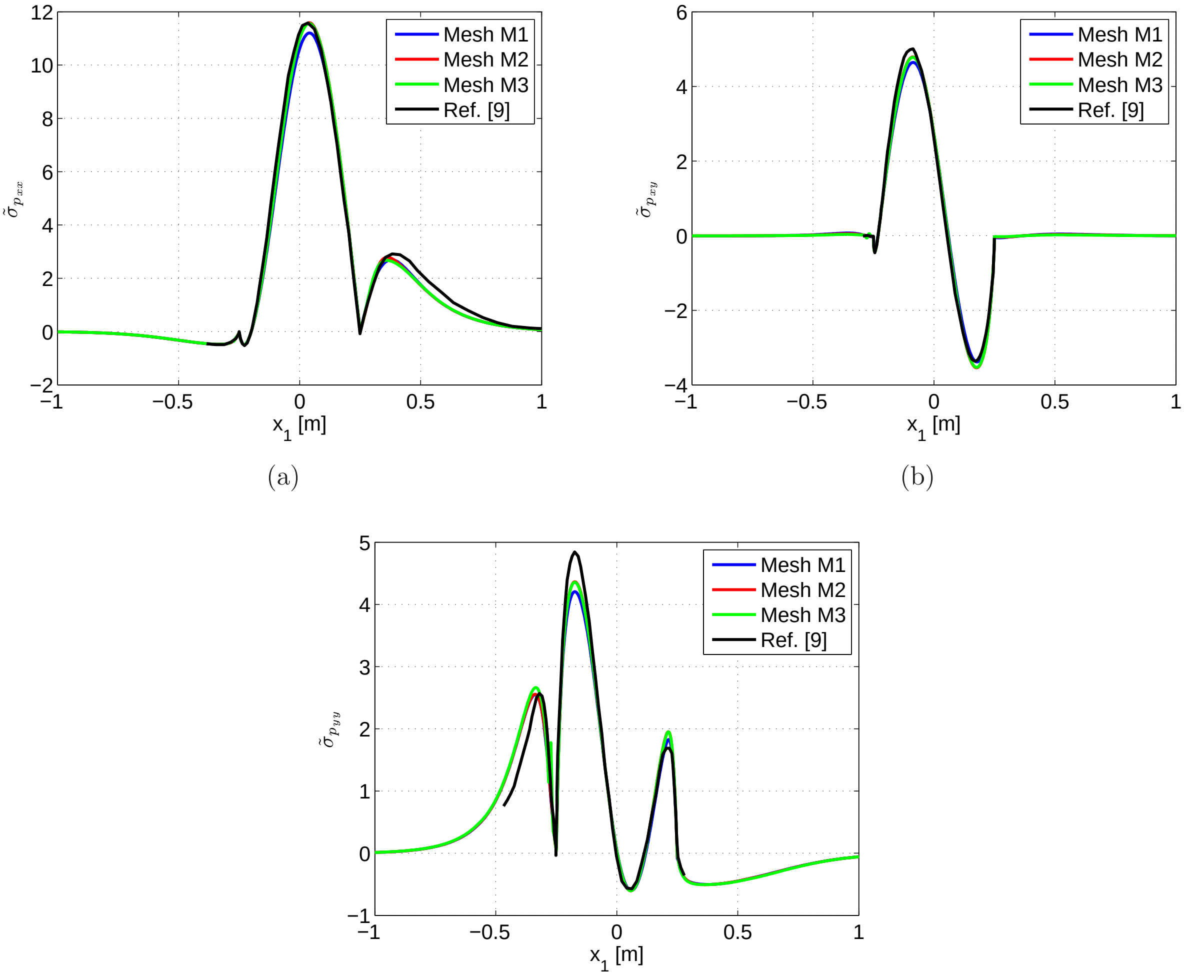

(a)

(b)

(c)

Figure 5.7: Profiles of the dimensionless viscoelastic stresses on the symmetry plane and on the cylinder surface for $Wi_M = 0.6$. The results for the two tested FVM meshes (M1, M2 and M3) are compared with ref. [3]: (a) $\hat{\sigma}_{p_{xx}}$ (b) $\hat{\sigma}_{p_{xy}}$ (c) $\hat{\sigma}_{p_{yy}}$.

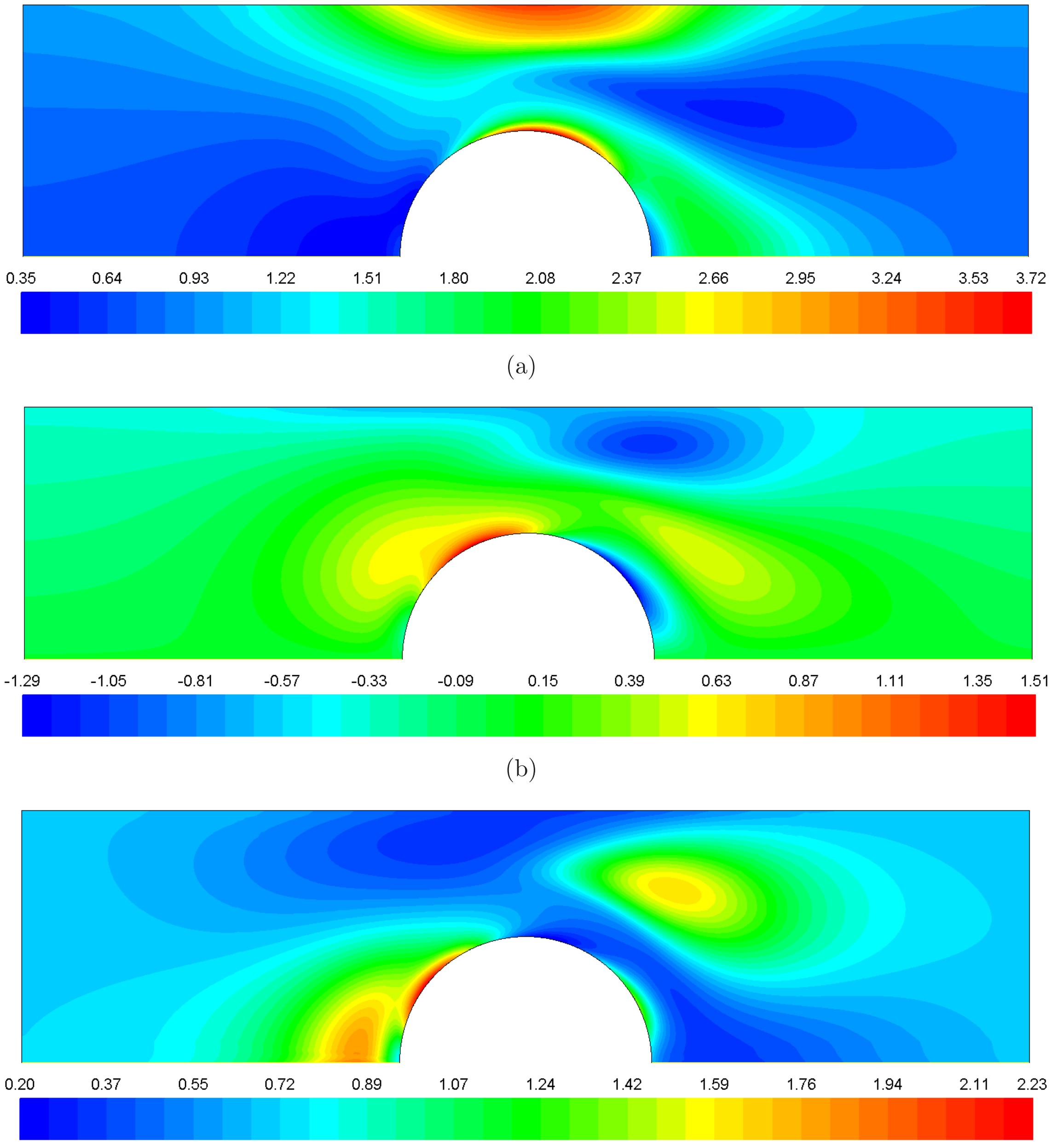

(a)

(b)

(c)

Figure 5.8: Contours of dimensionless molecular elongations (configuration tensor) for $Wi_M = 0.6$: (a) $\langle\langle\hat{\xi}_x\hat{\xi}_x\rangle\rangle$ (b) $\langle\langle\hat{\xi}_x\hat{\xi}_y\rangle\rangle$ (c) $\langle\langle\hat{\xi}_y\hat{\xi}_y\rangle\rangle$.

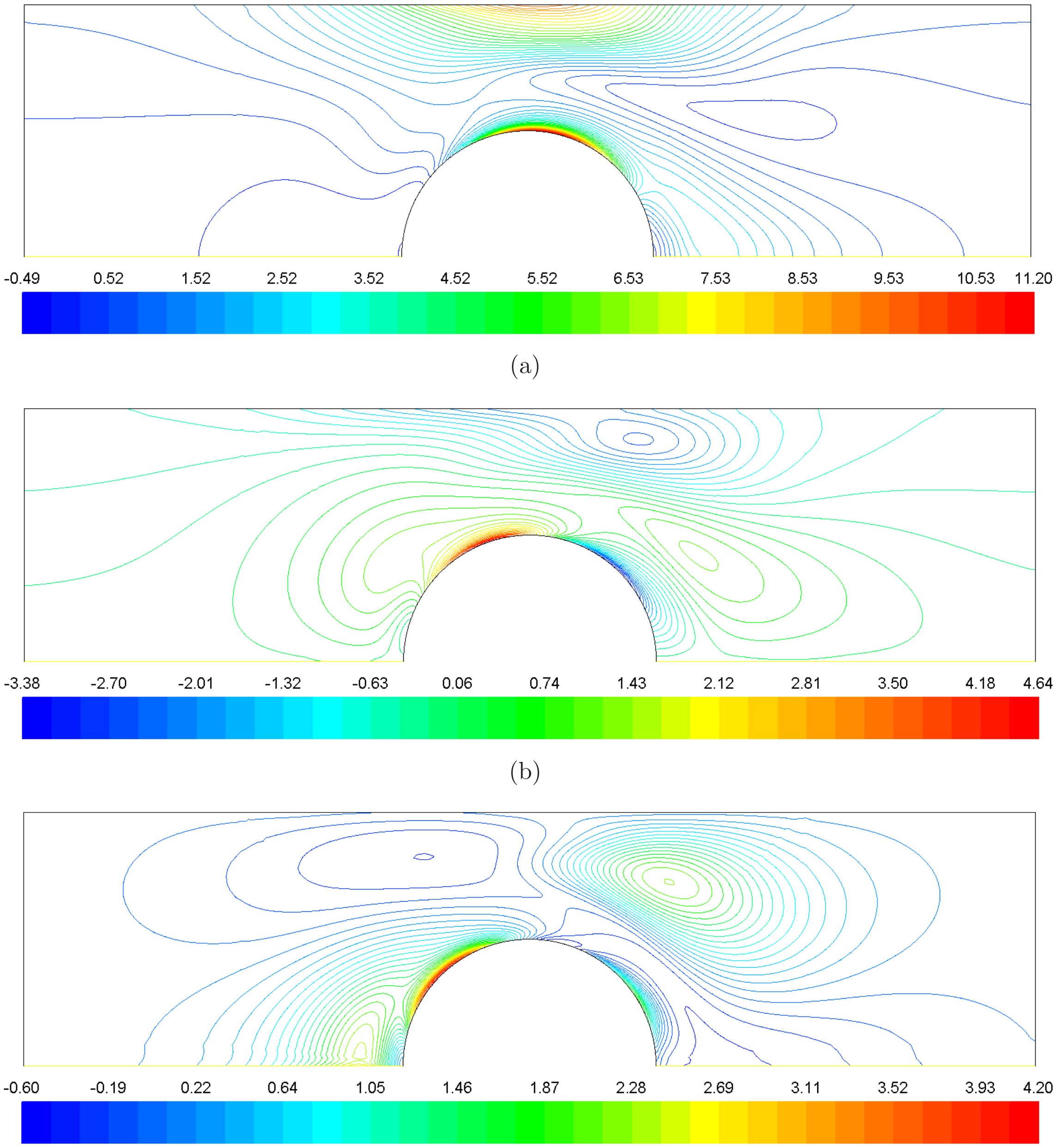

(a)

(b)

(c)

Figure 5.9: Contours of dimensionless viscoelastic stresses for $Wi_M = 0.6$: (a) $\hat{\boldsymbol{\sigma}}_{p_{xx}}$ (b) $\hat{\boldsymbol{\sigma}}_{p_{xy}}$ (c) $\hat{\boldsymbol{\sigma}}_{p_{yy}}$.

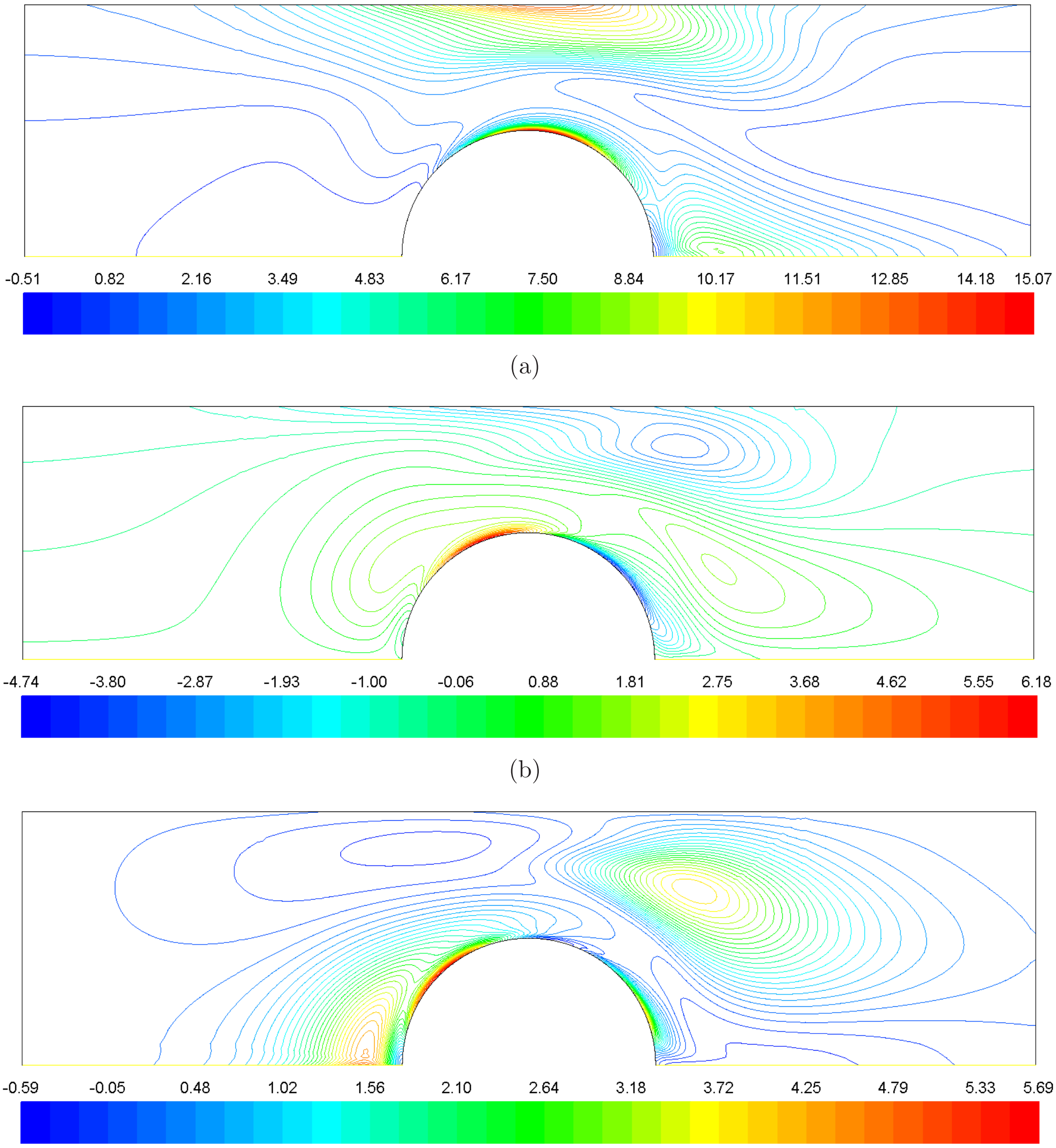

Figure 5.10: Contours of dimensionless viscoelastic stresses for $Wi_M = 0.9$: (a) $\hat{\boldsymbol{\sigma}}_{p_{xx}}$ (b) $\hat{\boldsymbol{\sigma}}_{p_{xy}}$ (c) $\hat{\boldsymbol{\sigma}}_{p_{yy}}$.

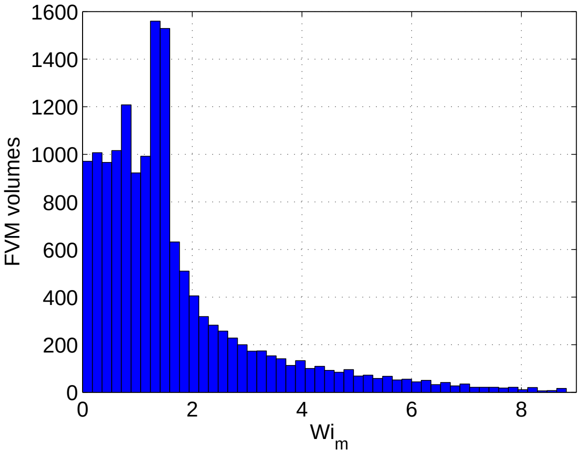

Figure 5.11: Discrete distribution of Wi_m in the physical domain (mesh M1, number of bins 50, $Wi_M = 0.6$).

5.4.3 Optimization

Let us now focus more in detail on the solution for $Wi_m = 0.6$. As derived from the analysis in Section 5.4.1, the error and numerical performance depends on the local Wi_m. The parameters for the sub-grid solution can then be adjusted according to the local Weissenberg number in the domain (Fig. 5.11). For this case, the local Weissenberg ranges between 0 and 9, with the highest frequencies between 0 and 2 and tail between 2 and 9. The parameters N and τ can then be chosen according to the following criteria:

1. Minimize numerical error: high lattice resolution and minimum relaxation time are to be used. This approach assures converged solution throughout the domain but non-homogeneous numerical error. The computational cost is high due to excessive number of nodes in $low{-}Wi_m$ regions.

2. Maximize computational speed: coarse lattice resolution and maximum stable relaxation time. The lattice parameters are chosen according to the maximum value of Wi_m in the domain, that is the coarsest allowed lattice and the maximum stable relaxation time. This approach does not guarantee constant nor converged numerical error. The maximum error depends on the choice of the lattice size (Fig. 5.5(a)).

Table 5.3: Summary table of the three sub-grid solution approaches: ME (minimize error), SA (strain-adaptive) and MS (maximize speed). The comparison of the computational speed-up per FVM iteration refers to different approaches on the same stencil (results for mesh M1).

stencil	**approach**	**N**	$\boldsymbol{\tau}$	**error**	**speed-up**
D2Q9	(ME) *minimize error*	N_{max}	τ_{min}	variable	13.6 (ME/SA) 17.9 (SA/MS)
	(SA) *strain-adaptive*	$f(Wi_m)$	τ_{max}	controlled	
	(MS) *maximize speed*	N_{min}	τ_{max}	variable	
D2Q5	(ME) *minimize error*	N_{max}	τ_{min}	variable	2.9 (ME/SA) 23.7 (SA/MS)
	(SA) *strain-adaptive*	$f(Wi_m)$	τ_{max}	controlled	
	(MS) *maximize speed*	N_{min}	τ_{max}	variable	

3. Strain-adaptive: lattice resolution based on local Wi_m. The lattice parameters are dynamically adapted according to the local Wi_m (Fig. 5.11). Therefore, coarser lattices are used in $low - Wi_m$ regions and finer lattices in $high - Wi_m$ ones. This approach represents a trade-off between the two above discussed ones and allows to optimize the computational speed, providing control on the error. The number of different lattices to use can be chosen on the basis of an expanded analysis such as that in Fig. 5.5(a), according to the desirable degree of speed-up/error control.

An overview of the three approaches is reported in Table 5.3. The parameters for the comparison of the achievable speed-up are: $N_{min} = 41$, $N_{max} = 121$, $\tau_{min} = 0.55$ and τ_{max} the maximum local stable value for the locally-adaptive approach (Fig. 5.5(b)) and the maximum stable value for $Wi_m = 9$ for optimizing the computational speed (0.6 for D2Q9 and 0.55 for D2Q5). In order to compare the advantage of the locally-adaptive approach here we use two lattice sizes, namely $N = 81$ for $Wi_m = 1 \div 5$ and $N = 121$ for $Wi_m = 6 \div 9$. We remark that this choice is made to illustrate the methodology but the number of lattice resolutions is arbitrary.

5.5 Summary and outlook

A novel micro-macro model for dilute polymeric solutions has been presented. The proposed approach relies on a coupled numerical solution for the macro and microscopic scales: a finite-volume method for the fluid-flow equations and a lattice-Boltzmann method for the kinetic viscoelastic model. This micro-macro approach allows to properly simulate non-homogeneous viscoelastic flows. The convection of the configuration distribution function in physical space is taken into account by means of an operator-splitting algorithm. This leads to an hyperbolic equation for the convective transport of viscoelastic stresses in physical space, which is equivalent to the transport of the distribution function. The algorithm is validated for its use in steady-state conditions. The validity of the introduced model has been proven against the benchmark problem of two-dimensional flow past a confined cylinder. We have observed a decrease of accuracy as reaching $Wi = 1$. Regarding this issue, there are three sources of error that deserve further investigation: (i) the failure of the Chapman-Enskog expansion for $Wi_M > 1$ as reported by Singh et al. [66]; (ii) the time step selected for the operator-splitting algorithm, which is not unique and affects the accuracy and (iii) the Cartesian discretization of the configuration distribution function used when the Fokker-Planck equation is solved with the lattice Boltzmann method. These three sources of error could be avoided by a proper redefinition of the approach and this is left for future work.

From a computational point of view, we have introduced and proven the validity of the coupling strategy when the micro-solver is implemented in a graphic card. This allows a 60x acceleration of the computational time. We have used a low-performance single graphic card, but the solution can also be distributed on multiple units, further reducing the computational time. We remark that in this work we proposed the coupling with a finite volume method solver, but the accelerated sub-grid solution can be easily called from other solvers (i.e. FEM-LBM or LBM-LBM solutions). Finally, the results obtained suggest that a direct numerical method together with proper hardware implementation, may deserve attention in the framework of numerical methods for complex fluids.

Chapter 6

Deformable fibrous media

6.1 Introduction

In this chapter the coupled numerical method developed for dilute viscoelastic suspensions is applied for the solution of a mesoscopic model for the fiber dynamics during the injection in LCM. As already discussed in the introduction of this thesis, textile preforms for these applications generally present a hierarchical structure and therefore different length scales to be taken into account (typically ranging between one and three orders of magnitude). As a consequence, the numerical solution of the fluid flow in the real geometry is computationally expensive or even not affordable with standard techniques when length scales diverge. The most commonly adopted practice for the numerical evaluation of the permeability of textile preforms, consist therefore in the numerical solution of the fluid flow in a REV of the textile, were the micro-scale permeability is computed by well established correlations. This approach however, has been shown to yield uncertainties on the prediction of the effective permeability (see Chapter 2), which can be attributed to the topology of the fibers that is not well accounted by the correlations for the micro-scale permeability.

The so-called “constitutive” relations [12], are analytical solutions or experimental correlations which serve as auxiliary means for the numerical simulations and are generally derived separating scales and/or reducing the dimensionality of the problem. A review of the several experimental and analytical techniques developed in this framework can be found in [13, 14]. One of the best established correlations was proposed by Gebart [23], who derived analytically a permeability law for ordered arrangements of cylinders:

$$\frac{K}{R^2} = C\left[\sqrt{\frac{1-\varepsilon_c}{1-\varepsilon}} - 1\right]^{5/2}; \tag{6.1}$$

where K is the permeabiloity, R is the characteristic radius, C is a geometrical factor depending on the arrangement, ε is the porosity and ε_c its critical value (or percolation threshold). The author calculated $C = 16/9\pi\sqrt{2}$, $\varepsilon_c = 1 - \pi/4$ for square arrangements and $C = 16/9\pi\sqrt{6}$, $\varepsilon_c = 1-\pi/2\sqrt{3}$ for hexagonal ones. Papathanasiou [75] addressed the multi-scale nature of the problem by solving numerically a square array layout of permeable multi-filament yarns with circular fibers and showed that the effective permeability depends strongly on the microscopic porosity only at low values of the macroscopic one. He proposed a dimensionless correlation for the multi-scale permeability in the form [76]:

$$K_{\text{eff}} = K_M\left[1 + a_1\left(\frac{K_{_M}}{K_m}\right)^{n-3/2}\right]; \tag{6.2}$$

being K_M and K_m respectively the macro- and microscopic permeabilities. The constants a_1 and n are geometrical parameters that the author best fitted with numerical simulation data, obtaining: $a_1 = 2.3$ and $n = 0.59$ for square arrangements, $a_1 = 3.0$ and $n = 0.625$ for hexagonal. Analogous studies were conducted for different yarn cross-sections and arrangements [77, 78]. Due to the geometrical dependence on the percolation threshold, the validity of the above (or similar) correlations is limited to strictly regular layouts, both at the macro- and microscopic scales. Consequently, their use for the numerical simulation of textile geometries often results in an unacceptable loss of accuracy due to: (i) the false assumption of regular topologies; (ii) the deformation of the structures induced by the fluid flow.

In order to overcome the first issue (i), random or realistically-reconstructed fiber configurations have been extensively studied [79, 80] and statistical descriptors have been proposed to relate the permeability to non-regular fiber arrangements [81, 82]. The effect of several microstructural parameters on the effective permeability has been also investigated using up-scaling techniques [83, 84]. However, despite the intense work on configurations and up-scaling, the fluid-structure interaction problem (ii) has not been addressed in this framework, as far as the present authors know.

The flow-induced deformation of fibers however, affects the interconnectivity of the porous matrix and thus the percolating paths, which in turn affect the permeability [12]. Indeed, relevant recent work on the permeability of deforming porous matrices, relies on the idea that the flow resistance of particle clusters (in two dimensions) is larger than that justifiable by single particle contributions. This is basically due to the entrapment of fluid within the cluster, which increases the apparent volume fraction reducing the hydraulic (or wet) area. Scholz et al. [85] recently proposed an empirical expression for permeability based on this concept:

$$K = c l_c^2 \left(\frac{1 - \chi_o}{N} \right)^{\beta} ; \tag{6.3}$$

where c is a constant that depends on the local pore geometry, l_c is the limiting hydrodynamic length, χ_o is the open-space Euler characteristic (of the conducting phase), N is the number of particles and β is the conductivity exponent. The Euler characteristic χ is a Minkowski functional that in this framework is defined as the difference between the number of connected components of each phase [86]; thus χ_o is the difference between the liquid phase and the number of solid components (neglecting the fluid entrapped in closed cavities). The authors best fitted $\beta = 1.27$ against experimental and numerical data for quasi-two-dimensional porous structures (close to the critical value $\beta_c = 1.3$ for two-dimensional structures [85]). The quantity $1 - \chi_o$ is generally referred to as *genus* and represents the total number of clusters of single or touching particles; thus $\left(1 - \chi_o\right)/N$ is the number of clusters per particle or *cluster density*, which in the following will be called Ω for compactness.

Based on this latter idea, we propose a multi-scale framework for the analysis of the local fiber topology induced by the fluid flow, through the cluster density. A two-dimensional mesoscopic model for the deformation of the fibers subject to out-of-plane movement restrictions is derived for creeping flow conditions by analogy with non-Brownian suspensions of particles with confining potentials. This leads to a homogeneous Fokker-Planck equation in phase space for the probability density function of the fiber displacements. A fiber clustering criterion is then defined via autoconvolution functions of the probability densities, which yield the local topology of the fibers and the related change in permeability through the cluster density Ω. The resulting multi-scale hydrodynamic system is solved numerically by a coupled finite-volume/lattice-Boltzmann method (the latter accelerated on GPU). Due to the lack of experimental or analytical means for its validation, the proposed model is assessed in terms of a non-Newtonian reduced viscosity related to the Brinkman's closure for porous media.

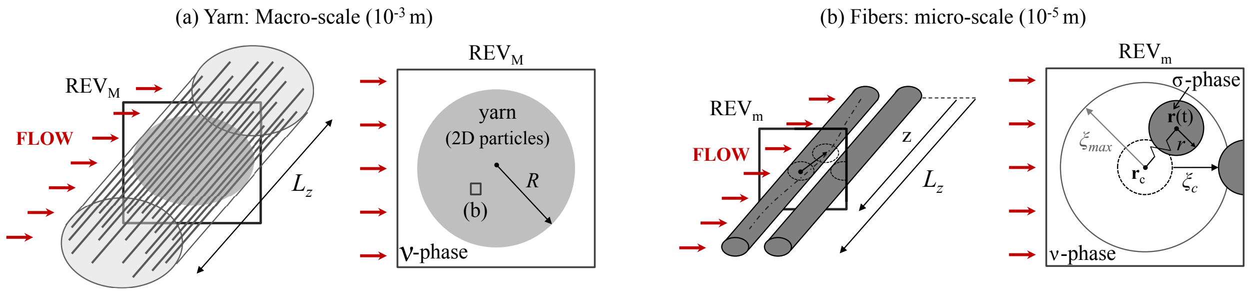
(a) Yarn: Macro-scale (10^{-3} m)

(b) Fibers: micro-scale (10^{-5} m)

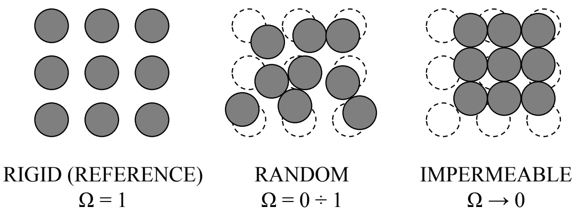
(c) Fiber configurations (topology)

Figure 6.1: Schematics of the scales considered and relative representative elementary volumes (REV): yarn macro-scale (a) and fiber micro-scale (b). Fiber configurations (c) and correspondent cluster density Ω, which is defined as the number of single or connected components per fiber.

6.2 Theoretical model

Let us consider the modeling framework shown in Fig. 6.1. We consider two scales: a macro-scale (the yarn scale in Fig. 6.1(a)) and a micro-scale (the fiber scale in Fig. 6.1(b)). The relative two-dimensional representative elementary volumes (REV) are shown on the right, respectively REV$_M$ and REV$_m$. The fibers are assumed to be clamped at both ends, thus they can bend under the effect of the perpendicular flow field. The cross-section of the yarn results in a domain of two-dimensional interacting particles suspended in the fluid (Fig. 6.1(a))), whose movement is restricted by the out-of-plane constraint.

Each fiber can bend up to ξ_{max}, which is a function of the distance z from REV$_m$ to the clamped end (Fig. 6.1(b)). The length of the fiber L_z is imposed by the structure of the textile, for example, by knit points. The two-dimensional model, is intended to be applied to real 3D fabrics.

The bending direction is imposed by the flow field, so in general the section of each fiber on REV$_m$ can move in a circle whose radius is ξ_{max}. The bending of each fiber affects that of the neighboring ones by hydrodynamic interaction, so the relative movement can lead to an increase or a reduction in the distance between them (Fig. 6.1(c)). Contact is approached as the relative distance ξ_c tends to zero. The resulting topology affects the fluid percolating paths, as long as clustered structures or preferential channels can form, which reduce or increase the hydraulic conductivity of the yarn.

In order to derive the theoretical model, we start by considering the transport equations at the micro-scale and proceed by upscaling them to the macro-scale via volume-averaging technique. The fluctuating stress tensor resulting from the fluid-structure interaction problem is closed with the proposed models for the fiber dynamics and clustering (which are detailed in dedicated sections).

6.2.1 Volume-averaged equations

Let us consider the representative elementary volume at the micro-scale (REV$_m$) in Fig. 6.1(b). The section of the fiber is represented by the solid σ-phase, suspended in the fluid ν-phase. The σ-region is therefore a mono-disperse solid phase without interconnectivity. The flow in the fluid ν-region is assumed to be Newtonian, isothermal and incompressible. The inertial effects are neglected in creeping flow conditions. The continuum transport equations for the fluid ν-region are given by the steady-state Stokes system:

$$\nabla_x \cdot \mathbf{v} = 0; \tag{6.4}$$

$$\mathbf{0} = -\nabla_x p + \mu \nabla_x^2 \mathbf{v}; \tag{6.5}$$

where $\mathbf{v}$ is the velocity vector, p is the pressure and μ the viscosity. The subscript x on operators indicates that they act in physical space. For solving this system of equations the no-slip boundary condition is set at the $\nu - \sigma$ interface, $\mathbf{v}|_{\nu\sigma} = \mathbf{0}$. In order to account for the porous media description, the superficial average of a quantity φ is defined as:

$$\langle \varphi \rangle = \frac{1}{\mathcal{V}} \int_{V_\nu} \varphi dV; \tag{6.6}$$

and the intrinsic volume average as:

$$\langle \varphi \rangle^{\nu} = \frac{1}{V_{\nu}} \int_{V_{\nu}} \varphi dV; \tag{6.7}$$

where V_{ν} is the volume of the fluid ν–phase in the total averaging volume $\mathcal{V}$ (extending over the length L_z). The relationship between superficial and intrinsic volume-averaged quantities is $\langle \varphi \rangle = \varepsilon_m \langle \varphi \rangle^{\nu}$, with ε_m the porosity for the ν–phase defined as $\varepsilon_m = V_{\nu}/\mathcal{V}$. The superficial average of the continuity equation (6.4) is expanded by applying the spatial averaging theorem [87]:

$$\nabla_x \cdot \langle \mathbf{v} \rangle + \frac{1}{\mathcal{V}} \int_{S_{\nu\sigma}} \mathbf{n}_{\nu\sigma} \cdot \mathbf{v} dS = 0; \tag{6.8}$$

where $S_{\nu\sigma}$ is the interface area between the fluid ν–phase and the solid σ–phase, $\mathbf{n}_{\nu\sigma}$ its unit normal. Equation (6.8) can be simplified by imposing the boundary condition $\mathbf{v}|_{\nu\sigma} = \mathbf{0}$ at the ν-σ–interface [88], which yields:

$$\nabla_x \cdot \langle \mathbf{v} \rangle = 0. \tag{6.9}$$

The superficial average is applied to the momentum equation (6.5), which yields:

$$\mathbf{0} = -\langle \nabla p \rangle + \mu \langle \nabla_x^2 \mathbf{v} \rangle. \tag{6.10}$$

Applying twice the spatial averaging theorem [87] and arranging terms in such a way that the superficial averaged velocity and the intrinsic averaged pressure are the main variables in the equation, the averaged momentum equation is obtained [88, 89]:

$$\begin{aligned} \mathbf{0} = & - \nabla_x \langle p \rangle^{\nu} + \frac{\mu}{\varepsilon_m} \nabla_x^2 \langle \mathbf{v} \rangle - \frac{\mu}{\varepsilon_m} \left(\nabla_x \varepsilon_m \cdot \nabla_x \langle \mathbf{v} \rangle^{\nu} \right) \\ & - \frac{1}{V_{\nu}} \int_{S_{\nu\sigma}} \mathbf{n}_{\nu\sigma} \cdot [-\mathbf{I}(p - \langle p \rangle^{\nu}) \\ & + \mu (\nabla_x \mathbf{v} - \nabla_x \langle \mathbf{v} \rangle^{\nu})] dS; \end{aligned} \tag{6.11}$$

being $\mathbf{I}$ the unit tensor. The last term is the position-dependent fluctuating stress tensor [90], which represents the drag force exerted by the solid phase onto the fluid phase ($\mathbf{F}^{d}_{\nu\sigma \to \nu}$) within the averaging volume V_{ν}. This term needs to be closed in order to solve the equations.

Table 6.1: Geometrical parameters and physical properties of the glass fibers considered.

	symbol	units	value		symbol	units	value
Geometry				**Material**			
Yarn radius	R	μm	$100 \div 500$	Density	ρ_o	g/cm^3	2.4
Fiber radius	r	μm	10	Young Modulus	E	MPa	85
Fiber length	L$_z$	μm	800				

The Brinkman's approximation for this term is [91]:

$$\mathbf{F}^{d,Br}_{\nu\sigma\to\nu} \approx -\mu\mathbf{K}_m^{-1}(\mathbf{x},\varepsilon_m)\cdot\langle\mathbf{v}\rangle + (\mu_{\text{eff}}-\mu)\nabla_x^2\langle\mathbf{v}\rangle\,; \tag{6.12}$$

where the first term is a Darcy drag, while the second is a correction that accounts for randomness in disordered media through an effective viscosity μ_{eff}. In this work we adopt the following closure:

$$\mathbf{F}^{d,\Omega}_{\nu\sigma\to\nu} \approx -\mu\mathbf{K}_m^{-1}(\mathbf{x},\varepsilon_m,\Omega)\cdot\langle\mathbf{v}\rangle\,; \tag{6.13}$$

where the permeability tensor is a function of the porosity and of the local topology of the solid phase through the cluster density Ω. This latter parameter accounts for the degree of aggregation of the solid phase, thus intrinsically for apparent variations in porosity through the open-space Euler characteristic χ_o [85]. Finally, for constant porosity ε_m, the equations to be solved in the yarn domain at the macro-scale (Fig. 6.1(a)) read:

$$\nabla_x\cdot\langle\mathbf{v}\rangle = 0; \tag{6.14}$$

$$\mathbf{0} = -\nabla_x\langle p\rangle^\nu + \frac{\mu}{\varepsilon_m}\nabla_x^2\langle\mathbf{v}\rangle - \mu\mathbf{K}_m^{-1}(\mathbf{x},\varepsilon_m,\Omega)\cdot\langle\mathbf{v}\rangle\,; \tag{6.15}$$

where the permeability tensor is recovered by solving the models for fiber dynamics and clustering, as explained in the next sections.

6.2.2 Microscopic dynamics

The equations to reproduce the movement of the solid σ–phase in Fig. 6.1(b) are derived from Newton's Second Law in a statistical way. As shown in the figure, the bending of the fibers is modeled by a mass-spring system, whose spring represents the resistance to bending and is thus related to the out-of-plane forces. The dynamic equilibrium on the mass is regulated by: (i) a drag force ($\mathbf{F}^d(t)$), due to the movement through the viscous solvent; (ii) the connector force ($\mathbf{F}^c(t)$), which represents the resistance to bending; (iii) a stochastic diffusion term ($\mathbf{F}^h(t)$), which accounts for hydrodynamic dispersion. Inertial terms are neglected in the limit of small Stokes numbers, which in this case we define as [92]:

$$St = \frac{2\rho_o r L_z v_{in}}{18\mu R} \ll 1; \tag{6.16}$$

being ρ_o the density of the material of the fibers and v_{in} the velocity at the inlet of REV$_M$ (Fig. 6.1(a)). The velocity v_{in} results from imposing creeping flow conditions through a Reynolds number based on the yarn radius R (see Section 6.4.3 for details).

Indicating with $\mathbf{r}_c$ the position of the fixed end of the spring (i.e. the undeformed state) and $\mathbf{r}(t)$ the position vector of the mass (see Fig. 6.1(b)), the drag force is:

$$\mathbf{F}^d(t) = \zeta L_z \left(\mathbf{v}(\mathbf{r}(t), t) - \frac{d\mathbf{r}}{dt}(t) \right), \tag{6.17}$$

with ζ being an Oseen drag coefficient [93], L_z the length of the fiber and the term inside the brackets the velocity of the mass relative to the viscous solvent.

The connector force is given as:

$$\mathbf{F}^c(t) = H(\mathbf{r}_c - \mathbf{r}(t)), \tag{6.18}$$

where the connector force law H will be discussed later. The last force results from hydrodynamic interactions:

$$\mathbf{F}^h(t) = \sigma d\mathbf{W}(t), \tag{6.19}$$

being σ the standard deviation of the Wiener process $\mathbf{W}(t)$. In this work we use this term to model the diffusive random fluctuations of the fibers due to hydrodynamic dispersion; for this purpose we adopt a diffusion coefficient D and write $\sigma = \sqrt{2D}$ for convenience.

Table 6.2: Summary table of the model parameters.

Parameter	**Dimensional**				**Dimensionless**		
	symbol	Eq.	units	value	symbol	scaling	value
Macro, micro porosities	-	-	-	-	$\varepsilon_M, \varepsilon_m$	-	1 - $\pi/4 \div 0.99$
Maximum extensibility	ξ_{max}	(6.23)	μm	$0 \div 36$	$\hat{\xi}_{max}$	$\hat{\xi}_{max} = \xi_{max}^2/2\theta D$	$0 \div 6.5 \cdot 10^4$
Contact distance	ξ_c	(6.25)	μm	$0 \div 157$	$\hat{\xi}_c$	$\hat{\xi}_c = \xi_c/\sqrt{2\theta D}$	$0 \div 1.1 \cdot 10^3$
Macro viscous number	-	(6.29)	-	-	I_M	-	$0 \div 3$
Fiber relaxation time	θ	-	s	$0.01 \div 15$	-	-	-
Micro viscous number	-	(6.30)	-	-	I_m	-	$0 \div 14$
Diffusion coefficient	D	-	m^2/s	$10^{-12} \div 10^{-9}$	$\hat{D}$	$\hat{D} = D/2D$	1/2

In the limit of small Stokes number, lubrication forces [94] are neglected, assuming that the relative velocity between the fibers is small. Finally, the dynamic equilibrium of forces on the mass yields the stochastic differential equation (Langevin equation):

$$\frac{d\mathbf{r}}{dt}(t) = \mathbf{v}(\mathbf{r}(t), t) + \frac{H}{\zeta L_z}(\mathbf{r}_c - \mathbf{r}(t)) + \sqrt{2D}\frac{d\mathbf{W}}{dt}(t). \tag{6.20}$$

Applying the forward Kolmogorov equation [95] and letting $\boldsymbol{\xi} = \mathbf{r}_c - \mathbf{r}(t)$ yields the diffusion (Fokker-Planck) equation for the probability density $\psi(\boldsymbol{\xi}, t)$ of the local fiber displacement with respect to the undeformed state:

$$\frac{\partial \psi}{\partial t} + \nabla_\xi \cdot \left[\left(\nabla_x \mathbf{v} \cdot \boldsymbol{\xi} - \frac{H\boldsymbol{\xi}}{\zeta L_z} \right) \psi \right] = D \nabla_\xi^2 \psi. \tag{6.21}$$

In this work we assume the connector force law to follow the finitely extensible non-linear elastic model [95], therefore:

$$H = \frac{h}{1 - ||\boldsymbol{\xi}||^2 / \xi_{max}^2}; \tag{6.22}$$

with h being the spring constant and ξ_{max} the maximum extensibility (see Fig. 6.1(b)).

6.2.3 Model parameters

Let us now focus on the calculation of the maximum extensibility ξ_{max} and of the contact distance ξ_c (see Fig. 6.1(b)). Considering the fiber as a high-aspect-ratio hyperstatic beam subject to a distributed load, the bending (and thus the maximum extensibility) is given as [96]:

$$\xi_{max} = \frac{\zeta z^2}{24EJ} (L_z - z)^2; \tag{6.23}$$

being E the Young modulus of the material and $J = \pi r^4/4$ the second moment. The drag force per unit length ζ can be recovered by the Oseen formula [93] as:

$$\zeta = \frac{4\pi\mu v_{in}}{\log\left(4/Re_m\right) - \gamma + 0.5}; \tag{6.24}$$

where Re_m is the Reynolds number based on the fiber radius and γ the Euler constant. The maximum bending ξ_{max} depends on the geometry of the fibers, on their material and on the flow, which makes this parameter representative of the out-of-plane forces.

On the other hand, the contact distance ξ_c is a geometrical function of the porosity. In this work we consider the fibers to be in a square arrangement when undeformed (see Fig. 6.1(c)); thus the contact distance can be written as:

$$\xi_c = \sqrt{\frac{\pi r^2}{1 - \varepsilon_m}} - 2r. \tag{6.25}$$

An overview of the material properties and dimensions are shown in Tab. 6.1.

6.2.4 Nondimensionalization

Considering a characteristic time-scale $\theta = \zeta L_z/2h$ of the fiber relaxation and a characteristic length-scale of the mass-spring system $\ell = \sqrt{2\theta D}$ (see Fig. 6.1(b)), the maximum extensibility and contact distance are made dimensionless respectively as $\hat{\xi}_{max} = \xi_{max}^2/2\theta D$ and $\hat{\xi}_c = \xi_c/\sqrt{2\theta D}$. The dimensionless form of Eq. (6.21) is:

$$\frac{\partial \psi}{\partial \hat{t}} + \nabla_{\hat{\xi}} \cdot \left[\left(\theta\left(\nabla_x \mathbf{v}\right) \cdot \hat{\boldsymbol{\xi}} - \frac{1}{2}\hat{H}\hat{\boldsymbol{\xi}}\right)\psi\right] = \hat{D}\nabla_{\hat{\xi}}^2\psi; \tag{6.26}$$

where $\hat{D}$ is a dimensionless diffusion coefficient which is equal to $1/2$ due to scaling and $\theta\left(\nabla_x \mathbf{v}\right)$ is the dimensionless shear-rate. The dimensionless connector force in Eq. (6.22) reads:

$$\hat{H} = \left[1 - ||\hat{\boldsymbol{\xi}}||^2/\hat{\xi}_{max}\right]^{-1}; \tag{6.27}$$

thus the support of the probability density function is a disc of radius $\hat{\xi}_{max}^{-1/2}$. The initial distribution for Eq. (6.26) is given as the analytical solution for $\theta\left(\nabla_x \mathbf{v}\right) = 0$, which, considering

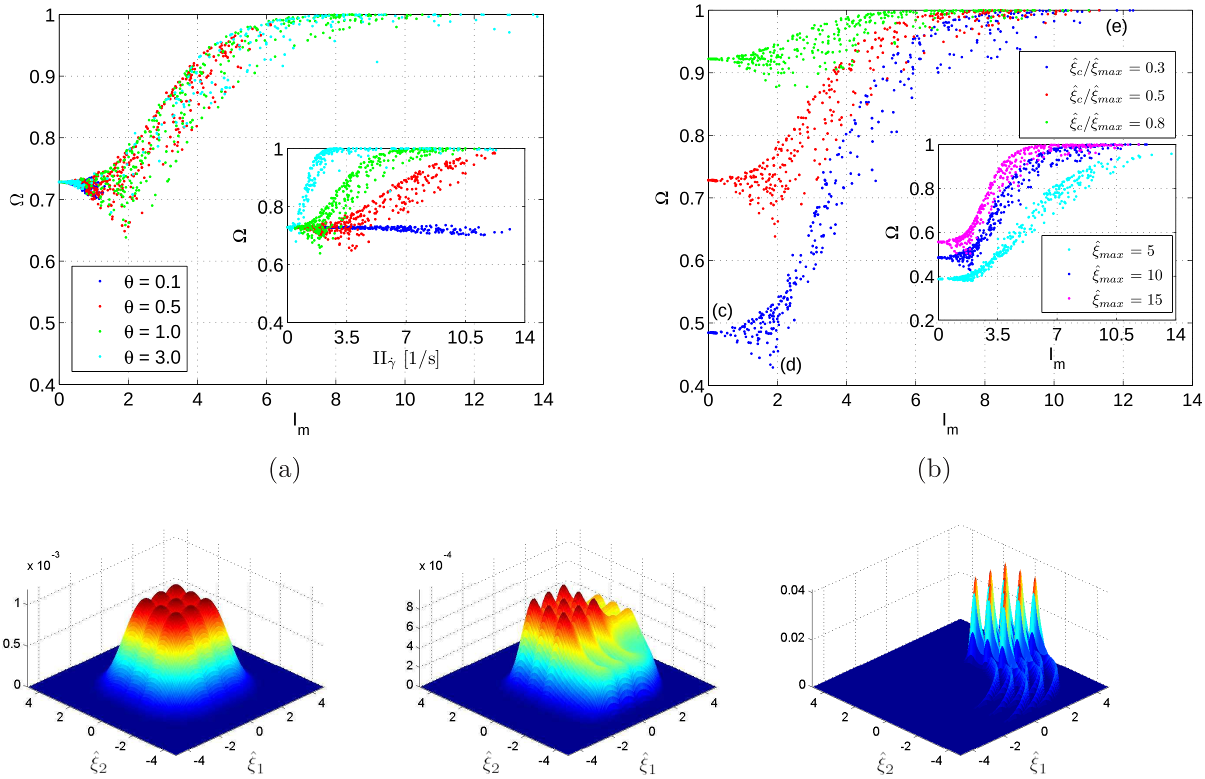

(a) (b)

(c) (d) (e)

Figure 6.2: (a) Numerical data obtained for Ω as a function of the viscous number I_m. The main figure shows the collapse of the data in the inset with the relaxation time θ ($\hat{\xi}_{max} = 10$, $\hat{\xi}_c/\hat{\xi}_{max} = 0.5$). (b) Cluster density Ω as a function of the contact/bending ratio $\hat{\xi}_c/\hat{\xi}_{max}$ for $\hat{\xi}_{max} = 10$ and of the maximum extensibility $\hat{\xi}_{max}$ for $\hat{\xi}_c/\hat{\xi}_{max} = 0.3$ (inset). Figures (c), (d) and (e) show an example configuration of the probability densities at the corresponding points in Fig. 6.2(b).

unitary normalization, reads:

$$\psi_0(\hat{\boldsymbol{\xi}}) = \hat{H}^{-\hat{\xi}_{max}/2} \left[\int \hat{H}^{-\hat{\xi}_{max}/2} d\hat{\boldsymbol{\xi}} \right]^{-1}. \tag{6.28}$$

An overview of the model parameters is shown in Table 6.2. The relaxation time θ is estimated on the basis of a viscous number defined as [97, 98]:

$$I_M = \theta \frac{v_{in}}{R}, \tag{6.29}$$

which represents the ratio between the time scale of the fiber rearrangement and the time scale of the flow. In this work, we set the maximum viscous number $I_M = 3$, which is the maximum value for which we found stability of the numerical methods (see Section 6.3). The dimensionless shear rate at the fiber scale (i.e. in the porous region), is then defined in scalar form as:

$$I_m = \theta \mathrm{II}_{\dot{\gamma}}; \tag{6.30}$$

being $\mathrm{II}_{\dot{\gamma}} =$ the second invariant of the rate of strain. The dimensionless shear rate I_m can be seen as a microscopic viscous number (whose typical value is I_M/ε_m).

The proposed model does not explicitly account for the contact among the fibers, therefore the maximum extensibility is restricted to $\xi_{max} \leq \xi_c + r$ (Fig. 6.1(b)). This physically means that when the contact is approached, the fiber cannot extend any further. The condition in dimensionless form reads (from Eq. (6.25)):

$$\hat{\xi}_{max} \leq \left(\sqrt{\frac{\pi r^2}{1 - \varepsilon_m}} - r \right) (2\theta D)^{-1} . \tag{6.31}$$

Considering that the porosity ε_m is bounded between the percolation threshold $\varepsilon_m^c = 1 - \pi/4$ (for a square arrangement) and 1, and assuming for the diffusion coefficient D values in the range $10^{-12} \div 10^{-9}$ m^2/s, Eq. (6.31) yields for the maximum extensibility the values given in Table 6.2.

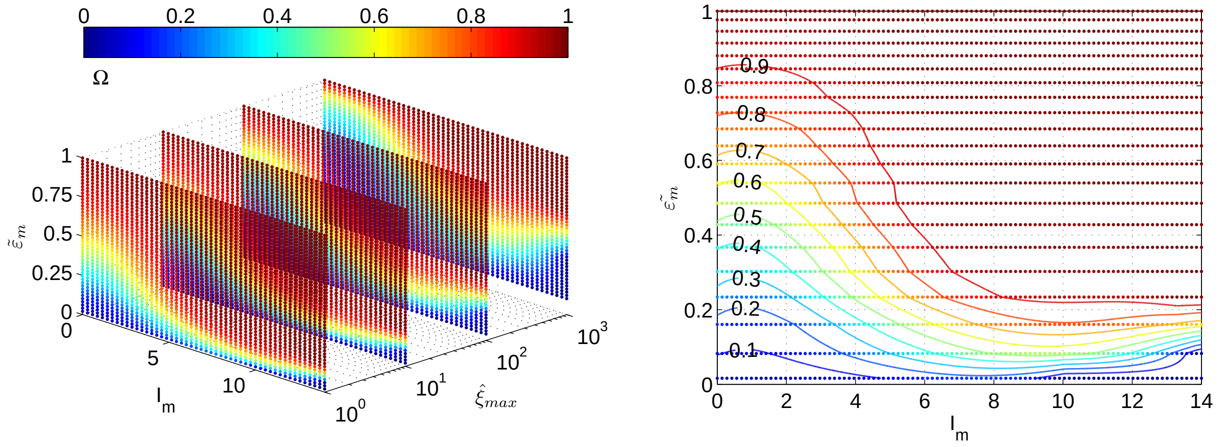

(a) (b)

Figure 6.3: Micro-scale phase diagram for deformable fibrous media (a). The diagram shows the iso-colors of the cluster density Ω as a function of the microscopic viscous number I_m, the normalized microscopic porosity $\tilde{\varepsilon}_m$ and the maximum extensibility $\hat{\xi}_{max}$ ($\hat{\xi}_c/\hat{\xi}_{max} = 0 \div 1$ and $D = 10^{-12}$ m^2/s). The numerical data are best fitted and a reduced number of points per dimension are shown to allow a proper visualization. Figure (b) shows the iso-Ω contours on the plane $\hat{\xi}_{max} = 10$ in (a).

6.2.5 Fiber clustering

The clustering criterion is defined on the basis of topological arguments, that is on the basis of the configuration of the fibers obtained from Eq. (6.26) through the probability of their displacement from the initial position. The distribution functions are associated with the section of the fibers in Fig. 6.1(b) and 6.1(c), thus a contact zone is defined by the overlap of the probability of one fiber with its neighboring ones. The probability that a fiber be in contact range with the neighbors is given by:

$$\Omega = 1 - \left(\frac{1-m}{n_f}\right) \sum_{i=1}^{n_f} \psi(\hat{\boldsymbol{\xi}}) * \psi(\hat{\boldsymbol{\xi}} + \hat{\xi}_c \mathbf{n}_i); \tag{6.32}$$

where n_f is the number of neighboring fibers, m is the reciprocal of the maximum number of fibers in a cluster, $\mathbf{n}_i$ is the unit vector to the i-th neighboring fiber and $*$ is the convolution operator. In this work we assume a square (undeformed) configuration, and thus each fiber has 8 neighbors ($n_f = 8$) on a square reference topological unit (Fig. 6.1(c) left). Notice that the topological unit is representative of the configuration of a number of fibers N, through the probability density, and thus the parameter m varies between 1/2 (for a cluster of 2 fibers) and

0 (for infinitely large cluster). In this work we analyze the worst condition for permeability, that is $m = 0$. When $\Omega = 1$ no clustering occurs (rigid fibers) while when $\Omega = 0$ the fibers form a single cluster (impermeable structure).

According to the chosen definition for overlap, Ω represents the quantity $(1 - \chi_o/N)$ in Eq. (6.3), with N in this case being the number of fibers represented by the topological unit. Therefore, considering that in our case the limiting hydrodynamic length l_c in Eq. (6.3) is the contact distance ξ_c in Eq. (6.25), the permeability can be rewritten as:

$$K_m = c \left[\sqrt{\frac{\pi r^2}{1 - \varepsilon_m}} - 2r \right]^2 \Omega^\beta, \tag{6.33}$$

where for the local pore geometry constant we adopt the same value ($c = 1/12$) as for Eq. (6.3) [85], which corresponds to a confinement between parallel plates [99].

Finally, Eq. (6.33) yields the permeability as a function of the porosity ε_m and of the cluster density Ω, which is used for the closure of the hydrodynamic system (Eq. (6.15)).

6.3 Numerical methods

The numerical approach for solving the theoretical model consists in a coupled finite-volume/lattice-Boltzmann solution: finite volume method for the fluid flow equations and lattice Boltzmann method for the Fokker-Planck equation. This hybrid methodology has already been applied and validated for the numerical simulation of viscoelastic suspensions in Chapter 5; therefore here we briefly recall the approach and refer the reader to the previous Chapter for further details.

6.3.1 Fluid flow equations

The volume-averaged transport equations (6.14) and (6.15) are solved by the finite volume method (FVM) using the commercial solver ANSYS Fluent®. In this paper we adopt a third order quadratic upwind scheme for momentum and a second order scheme for pressure interpolation. The Semi-Implicit Method for Pressure Linked Equations is used for the pressure–velocity coupling.

6.3.2 Fiber dynamics model

The Fokker-Planck equation in the configuration space (6.26) is solved by a lattice Boltzmann method (LBM) using a lattice-BGK equation. In this work we adopt a 16,384 DoF lattice (D2Q5) and a relaxation time $\tau = 0.55$ (see Chapter 5). For computational efficiency, the lattice Boltzmann solution is accelerated on a Graphic Processing Unit (GPU) by a Compute Unified Device Architecture (CUDA) implementation [100] using *shared memory*. For the details of the implementation see Appendix A.

6.3.3 Multi-scale system

The multi-scale hydrodynamic system resulting from Eq. (6.14), (6.15) and (6.26) is solved by coupling the two previous methods. The compiled CUDA code of the lattice Boltzmann solution is dynamically called at cell centers from the FVM solver through a compiled User Defined Function (UDF). The sub-grid simulation is driven by passage and retrieval of the required variables between the two compiled codes through a stream process.

The algorithm has already been applied and validated for non-homogeneous Fokker-Planck equations in dilute viscoelastic suspensions in Chapter 5. In this chapter we deal with a homogeneous Fokker-Planck equation, therefore the algorithm reduces to the following:

1. solution of Eq. (6.14) and (6.15) by the finite volume method (on the CPU);
2. solution of Eq. (6.26) by lattice Boltzmann method (on the GPU);
3. solution of Eq. (6.32) for the clustering model (on the GPU);
4. correction of Eq. (6.33) for the local permeability (on the CPU).

The initial guess for the loop is given by the correspondent case of rigid porous medium (i.e. without sub-grid model). The numerical algorithm is repeated until global convergence of Eq. (6.14) and (6.15), which in this case requires 4 to 6 complete loops. Each loop requires around 2 hours of GPU time with a 20-25,000 cell FVM mesh.

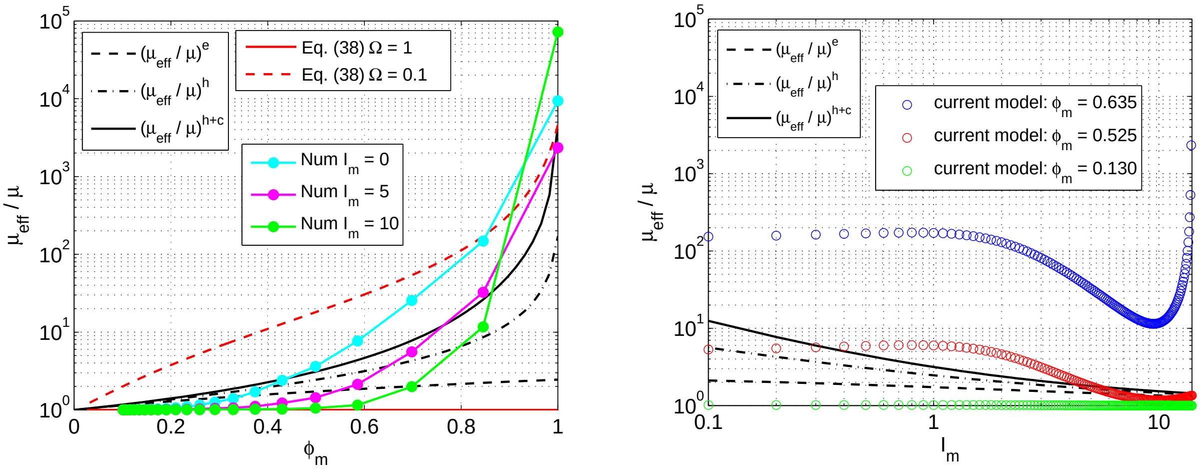

(a) (b)

Figure 6.4: Comparison of the reduced viscosity of the proposed model with that of wet granular media. Dimensionless viscosity as a function of the normalized volume fraction $\tilde{\phi}_m$ (a) and of the viscous number I_m (b). The maximum extensibility is $\hat{\xi}_{max} = 10$, the diffusion coefficient $D = 10^{-10}$ m^2/s and the constant $A = 0.1r^2$ (Eq. (6.37)).

6.4 Results and discussion

6.4.1 Micro-scale model

Let us first focus on the analysis of the proposed model for the fiber dynamics (Eq. (6.26)) and clustering (Eq. (6.32)). A parametric study has been carried out using a set of 2,000 random realizations of the velocity gradient tensor $\nabla \mathbf{v}$, which account for local inhomogeneity of the flow field inside the porous medium. Incompressibility condition has been assured. The study has been performed varying the parameters θ (fiber relaxation time), $\hat{\xi}_{max}$ (maximum bending) and the ratio $\hat{\xi}_c/\hat{\xi}_{max}$ (contact/bending ratio). The cluster density Ω in Eq. (6.32) is computed for each realization, which allows the analysis of its dependence on each parameter.

The data obtained for varying θ as a function of the invariant of $\nabla \mathbf{v}$ is shown in the inset of Fig. 6.2(a): the data collapse into a single curve for $\theta \mathrm{II}_{\dot{\gamma}}$, which is the dimensionless rate of strain or microscopic viscous number I_m. The spread of the data is due to the definition of I_m based on the invariant, for which, the same value can be yield by different $\nabla \mathbf{v}$.

The effect on Ω of varying $\hat{\xi}_c/\hat{\xi}_{max}$ and $\hat{\xi}_{max}$ is shown in Fig. 6.2(b) and relative inset, while Fig. 6.2(c), 6.2(d) and 6.2(e) show an example configuration of the probability densities at the corresponding points in the figure.

In order to interpret physically the results, let us firstly recall that Ω is bounded between 0 and 1, which respectively correspond to the maximum and minimum fiber clustering, i.e. to the impermeable and rigid conditions of the fibrous medium. If $I_m \to 0$, the strain rate (or the relaxation time) tends to zero, therefore Ω is given by the overlap of the initial probability densities of Eq. (6.28) (see Fig. 6.2(c)). For increasing I_m, the probability densities present more localized features, thus the overlap reduces and Ω increases (see Fig. 6.2(d) and 6.2(e)). This physically recovers the increasing anisotropy and stiffness of the fibers due to the higher strain rate, which leads the fibers towards the rigid condition ($\Omega = 1$).

With regards to the dependence of Ω on the maximum bending $\hat{\xi}_{max}$ and contact/bending ratio $\hat{\xi}_c/\hat{\xi}_{max}$, Fig. 6.2(b) shows that for constant $\hat{\xi}_{max}$ and increasing $\hat{\xi}_c$, the contact probability is reduced and Ω increases. This is justified by the fact that, for increasing $\hat{\xi}_c$, the porosity increases (see Eq. (6.31)), lowering the contact probability. Similarly, the inset in the figure shows the effect of varying $\hat{\xi}_{max}$ with constant $\hat{\xi}_c/\hat{\xi}_{max}$.

In order to present the results in a compact manner, a microscopic phase diagram is built (Fig. 6.3(a)). The numerical data is best fitted and a reduced number of points is plotted for each dimension to allow a proper visualization. The diagram shows the contours of the cluster density Ω for $D = 10^{-12}$ m^2/s as a function of the microscopic viscous number I_m, the maximum extensibility parameter $\hat{\xi}_{max}$ and a normalized microscopic porosity $\tilde{\varepsilon}_m$ defined as:

$$\tilde{\varepsilon}_m = \frac{\varepsilon_m - \varepsilon_m^c}{\varepsilon_m^{max} - \varepsilon_m^c}, \tag{6.34}$$

where the porosity ε_m as a function of the model parameters is given by Eq. (6.31), and $\hat{\xi}_c/\hat{\xi}_{max}$ ranges between 0 and 1. The maximum porosity ε_m^{max} is given by $\hat{\xi}_c = \hat{\xi}_{max}$.

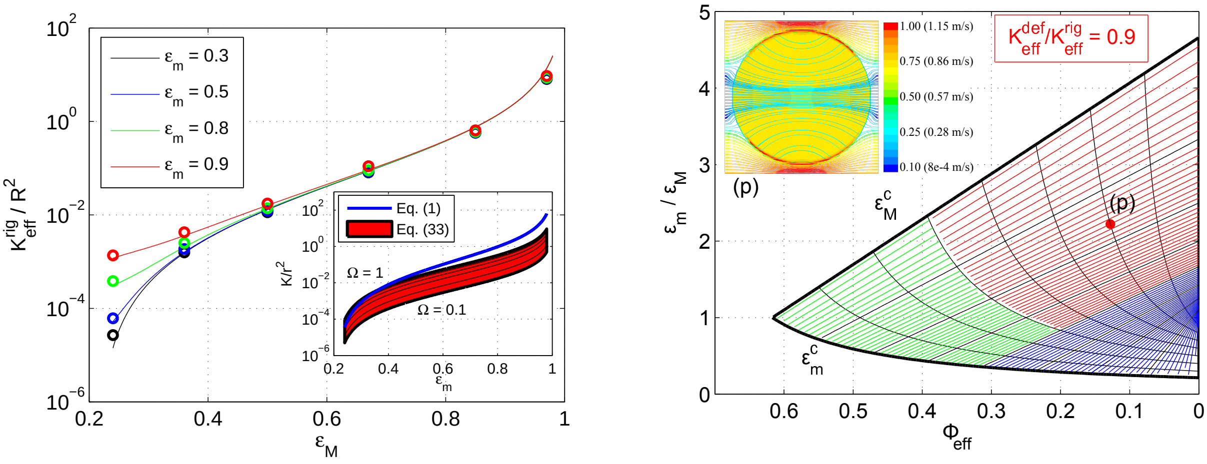

(a) (b)

Figure 6.5: (a) Comparison of the numerically predicted effective permeability with the analytical solution of Eq. (6.2) for rigid porous media. In the inset, comparison of the microscopic permeability given by Eq. (6.1) and Eq. (6.33). (b) Multi-scale phase diagram for fibrous media. In the blue area, the microscopic porosity has a negligible effect on permeability; in the green area, the effects of fiber deformations are negligible; in the red area, the effect of fiber deformation significantly modifies the effective permeability. In the inset, flow field configuration at point (p). The model parameters for the simulation are: $\hat{\xi}_{max} = 10$, $\varepsilon_M = 0.36$, $\varepsilon_m = 0.8$, $I_M = 0.6$, $\hat{\xi}_c/\hat{\xi}_{max} = 0.36$, $D = 10^{-11}$ m^2/s and $z = L_z/2$. The colorbar shows the Ω scale for the contours and the velocity magnitude (within parentheses) for the pathlines.

The plane corresponding to $\hat{\xi}_{max} = 10$ in the phase diagram is shown in Fig. 6.3(b). The contours show the iso-Ω values as a function of the viscous number I_m and normalized porosity $\tilde{\varepsilon}_m$. For $\Omega < 0.1$ the fibrous medium tends to the impermeable state and for $\Omega > 0.9$ to the rigid one. In the intermediate range, the cluster density Ω for a constant porosity increases with the viscous number, and decreases with the maximum extensibility (Fig. 6.3(a)). The first effect is related to the increasing stiffness of the fibers and thus to the lower contact probability, while the second one is due to the increasing maximum bending of the fibers. Finally, the increase in Ω observed for very high I_m, can be associated with the jamming of the fibers for very low porosities.

6.4.2 Model assessment

We will now focus on the assessment of the behavior of the proposed model. We should first indicate that a framework for the validation is not available, neither experimentally nor analytically. Therefore we compare the results of our model with the rheology of wet granular media in terms of an equivalent reduced viscosity. Boyer et al. [98] have recently proposed a phenomenological law for the rheology of dense suspensions of spherical particles in terms of volume fraction ϕ_m and a dimensionless viscous number I_v (which is formally equivalent to our definition for I_m). The authors deduced the dimensionless shear viscosity in the following form:

$$\hat{\eta} = 1 + \frac{5}{2}\phi_m \left(1 - \frac{\phi_m}{\phi_m^{max}}\right)^{-1} + \nu(\phi_m)\left(\frac{\phi}{\phi_m^{max} - \phi_m}\right)^2 ; \tag{6.35}$$

where $\phi_m^{max} = 0.585$ is the maximum volume fraction at the jamming point and $\phi_m = \phi_m^{max}/(1+I_v^{1/2})$. The first two terms on the right-hand side of Eq. (6.35) represent the hydrodynamic contribution $\hat{\eta}^h$ to the rheology and they tend to the Einstein viscosity $\hat{\eta}^E = 1 + 5\phi_m/2$ at $O(\phi_m)$. The third term represents solid contact contributions $\hat{\eta}^c$, where:

$$\nu(\phi_m) = c_1 + \frac{c_2 - c_1}{1 + I_0\phi_m^2(\phi_m^{max} - \phi_m)^{-2}} ; \tag{6.36}$$

being $c_1 = 0.32$, $c_2 = 0.7$ and $I_0 = 0.005$ fitting rheological parameters [98]. The expression for the contact contribution has been chosen to be similar to an analogous one for dry granular media [97].

In order to assess the behavior of our model, we compare the numerical results obtained with the above mentioned contributions, namely η^E, η^h and η^{h+c}, according to the following rheological description:

$$\hat{\eta} = \frac{\mu_{\text{eff}}}{\mu} \approx 1 + A\left[\left(K_m^{\text{def}}\right)^{-1} - \left(K_m^{\text{rig}}\right)^{-1}\right], \tag{6.37}$$

obtained by comparison of the Brinkman's closure (Eq. (6.12)) and ours (Eq. (6.13)). The prefactor A results from the comparison, which is based on a simplified 1D approximation of the two closures for unidirectional flow within the porous medium. The exact value of the prefactor depends on the integration constants (i.e. boundary conditions). Here we show the results for a typical value $A = 0.1r^2$.

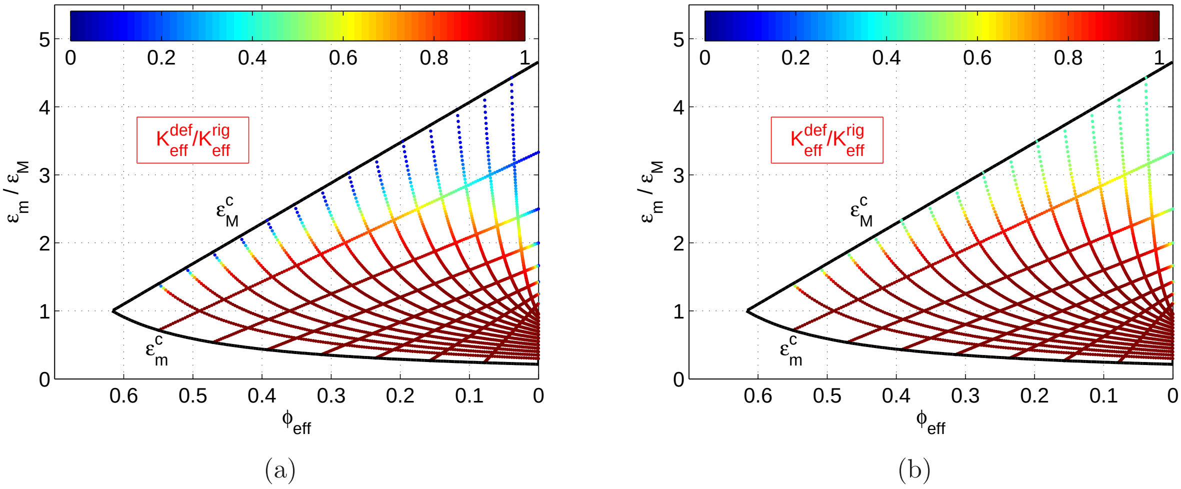

(a) (b)

Figure 6.6: (Color online) Multi-scale permeability of deformable fibrous media: $\Omega = 0.1$ (a) and $\Omega = 0.5$ (b). The colorbars show the ratio between the effective permeabilities in the deformable and rigid cases.

The comparison is shown in Fig. 6.4(a), where the permeabilities in the deformable and rigid case are given by Eq. (6.33). In the rigid case $\Omega = 1$ (constant). The volume fraction has been normalized as it is done for the porosity in Eq. (6.34). The normalization allows a better comparison of the results, as long as the maximum volume fraction at jamming for wet granular media is $\phi_m^{max} = 0.585$, while in our case it can be assumed to be $\phi_m^{max} = 1 - \varepsilon_m^c$ (due to the ordered packing).

The numerical data show qualitative agreement with the rheology of wet granular suspensions. For a constant viscous number I_m and increasing volume fractions, the behavior is shear-thickening, due to the increasing clustering of the fibers for the reduced mobility. On the other hand, the behavior is shear-thinning for constant volume fraction and increasing viscous number. This physically recovers the increasing stiffness of the fibers and thus the lower clustering probability. Figure (6.4(b)) shows that for low and intermediate volume fractions the non-Newtonian reduced viscosity exhibits shear-thinning behavior with low- and high-shear *plateaux*. For high volume fractions and high shear rates, the behavior changes abruptly from shear thinning to shear thickening (compare Fig. 6.3(b)). This phenomenon is related to the restriction caused by the out-of-plane forces, which leads the fibers close to jamming.

6.4.3 Multi-scale model

In order to assess the accuracy of the FVM numerical solution, we firstly analyze the permeability of a dual-scale rigid porous medium (Fig. 6.1(a)). The domain is periodic, and the macroscopic Reynolds number $\mathrm{Re}_M = \rho v_{in} R/\mu$ is kept constant at 10^{-3} (creeping flow). The microscopic permeability is computed according to Eq. (6.1) considering a square fiber arrangement. The effective permeability is then recovered by Darcy's law as:

$$K_{\text{eff}} = -\frac{\mu}{\Delta p} v_{in}; \tag{6.38}$$

where Δp is the stream-wise pressure drop per unit length. The numerical results (Fig. 6.5(a)) show very good agreement with the correlation for multi-scale fibrous media of Eq. (6.2). As expected, the effect of the microscopic porosity ε_m on the effective permeability is important for low macroscopic porosities, in this case for $\varepsilon_M < 0.6$. In this range, the effective permeability can vary up to two orders of magnitude, depending on the microscopic porosity ε_m.

At the microscopic scale, the permeability can vary with respect to the rigid case according to the topology of the fibers induced by the fluid flow. The entity of this variability is shown in the inset of Fig. 6.5(a), which shows that the permeability of the rigid case given by Eq. (6.33) for $\Omega = 1$ slightly underestimates that given by Eq. (6.1). The permeability decreases with the clustering of the fibers, that is, with decreasing Ω. If Ω tends to zero, the permeability also tends to zero, which means that the yarn is impermeable (we show only $\Omega = 0.1$ for illustration). Therefore, better conditions for infiltration are achieved for high Ω, that is, high (dimensionless) strain rates (compare Fig. 6.3(b)).

In order to analyze this effect on the effective permeability, a multi-scale phase diagram (Fig. 6.5(b)) is built with the effective volume fraction ϕ_{eff}, which is a commonly used quantity for textiles since it is experimentally measurable through the weight and volume of the textile. For a given ϕ_{eff}, the relationship between micro and macroscopic porosities cannot be easily computed; however the effective volume fraction can be written in terms of the porosities in the following form:

$$\phi_{\text{eff}} = (1 - \varepsilon_m)(1 - \varepsilon_M); \tag{6.39}$$

which describes all the possible configurations of the textile. The diagram in Fig. 6.5(b) shows the whole range of micro- and macroscopic porosities, down to the percolation thresholds (ε_m^c and ε_M^c). The blue area corresponds to $\varepsilon_M > 0.6$, where the microscopic porosity has a negligible effect on permeability (Fig. 6.5(a)). The green area identifies the range of microscopic porosity from the percolation threshold to 0.5, where the effects of fiber deformations are negligible due to the high packing of fibers and thus to their reduced mobility. The red area represents the range of micro- and macroscopic porosities where the effect of fiber deformation and thus of the clustering significantly modifies the effective permeability.

The inset shows the pathlines of the flow field on top of the Ω contours obtained with the multi-scale model in the deformable case at the corresponding point (p) in the diagram. The model parameters are: $\hat{\xi}_{max} = 10$, $\varepsilon_M = 0.36$, $\varepsilon_m = 0.8$, $I_M = 0.6$ and $\hat{\xi}_c/\hat{\xi}_{max} = 0.36$ with $D = 10^{-11}$ m^2/s. For this case, the effective permeability is 10% lower than in the rigid case due to the clustering of fibers in the yarn.

In order to present the results in a compact manner, we show the effect of the clustering of fibers in the yarn on the effective permeability using the phase diagrams in Fig. 6.6(a) and 6.6(b). The effective permeability is given by Eq. (6.2), where the macro permeability K_M is given by Eq. (6.1) and the microscopic one K_m by Eq. (6.33). The qualitative limiting values shown in Fig. 6.5(b) are well recovered, that is, fiber deformation is important in the red region. Fig. 6.6(b) shows that for typical textile parameters, namely intermediate cluster density ($\Omega = 0.5$), low to intermediate effective volume fractions ($\phi_{\text{eff}} < 0.4$) and intermediate to high micro-to-macro porosities ($\varepsilon_m/\varepsilon_M = 1.5 \div 2.5$), the effective permeability of the deformable case can be up to 60% lower than that of the rigid case.

6.5 Summary and outlook

A two-dimensional mesoscopic model for fiber deformation in hierarchical fibrous media has been presented. The model has been derived for creeping flow conditions by analogy with non-Brownian suspensions of particles with confining potentials. The resulting multi-scale hydrodynamic system is numerically solved by a coupled finite-volume/lattice-Boltzmann method. The behavior of the proposed model has been compared with the rheology of wet granular suspensions through a non-Newtonian reduced viscosity and qualitative agreement has been found.

The microscopic permeability of the fibrous medium has been characterized in terms of porosity, dimensionless shear rate and dimensionless out-of-plane forces. The best conditions for infiltration have been found for high shear rates and high out-of-plane forces, that is for rigid fibers and thus reduced clustering.

The effective permeability has been shown to be sensitively affected by deformability over the whole range of volume fractions; in particular for typical values for textiles, the effective permeability of the deformable case can be up to 60% lower than that in the rigid case. The results obtained suggest that a better insight on the physics of the fibers can be helpful in identifying best operating conditions for infiltration in hierarchical fibrous media.

The present work could be improved considering further physical or chemical potentials within the fibers. In order to reduce the computational cost, model order reduction techniques could be applied.

Chapter 7

Conclusions

7.1 Conclusions and further work

Most of the uncertainty on the numerical evaluation of the permeability of textile preforms for fiber-reinforced composites is related to the deformations that the textiles undergo during the production process, that is: the compaction in the mold (i), and the injection of the resin (ii). The difficulties in the development of proper numerical models to account for these deformations are due to the hierarchical structure of the preforms, which requires non-standard modeling techniques. The development of novel numerical models to account for the effect on permeability of these deformations has been subject of this thesis.

The analysis of the mechanical behavior of the textile during the compression in the mold (i), has been addressed by means of a phenomenological model, where the yarns have been modeled as viscoplastic soft solids, based on the analogy between the fiber bundles and flowing granular media. The resulting multi-phase model has been solved numerically using the commercial CFD code ANSYS Fluent.

The analysis of the deformation of the textile and its interaction with the resin during the injection (ii), has been addressed by means of a mesoscopic model, which accounts for the fluid-structure interaction at the fiber level. A coupled numerical method has been developed for the solution, which consists in the finite volume method for the fluid flow equations (in ANSYS Fluent) and a lattice Boltzmann method for the fiber dynamics (accelerated on GPU through a tailored implementation).

On the basis of the results obtained, the following main conclusions can be drawn:

1. The model developed for the compaction in the mold, showed to be appropriate for a phenomenological analysis of the deformation of the yarns under compression. The model allows to quantitatively analyze the evolution of the fiber volume fraction during the compaction, which yields useful information for a better understanding of the distribution of the fibers before the injection of the resin.

2. The proposed analogy between fiber bundles and granular materials provides the possibility to develop advanced mesoscopic constitutive models for the yarns (and ultimately, for the textiles). Such constitutive models can then be efficiently solved using computational fluid dynamics, to study the fiber topology resulting from the compaction and its effect on permeability.

3. The mesoscopic model developed for the fiber dynamics during the injection, allows analyzing their topology induced by the fluid flow. The permeability of the fibers has been described in terms of a topological invariant instead of geometrical parameters, which is the fundamental point for the analysis. The computational cost of the mesoscopic model has been remarkably reduced by the coupled numerical method developed.

4. It has been found that the clustering of fibers during the injection significantly reduces the effective permeability in hierarchical fibrous media, which could explain the overestimations generally obtained with simplified numerical approaches. In this sense, the phase diagrams presented for the permeability, allow identifying the best operating conditions for the infiltration of the resin.

5. The proposed models have been developed using non-conventional techniques of fluid dynamics, which opens the possibility for a unified framework for the analysis and ultimately, for a more precise estimation of the permeability. This work aims to represent a first tentative in this direction.

As regards the future developments of the present work, the following improvements of the proposed models are suggested:

YARN COMPACTION MODEL

- A viscometric rheology [98, 101] can be adopted for the yarns in the quasi-static regime of compression. This would lead to the inclusion of normal viscosities, which is this framework should be related to the restriction due to the out-of-plane forces.
- In order to account for time-related effects (e.g. fiber relaxation or hysteresis), viscoelastic constitutive models can be considered. In this sense, an extension for this case of the model developed in Chapter 6 can be also considered.
- Improvement of the behavior of the interface adding multi-scale information through phase-field models [102].
- Further elaboration on the topology of the fibers (i.e. clustering), which has been found in this thesis to sensibly affect the hydraulic conductivity of the yarns during the injection of the resin.

FIBER DYNAMICS MODEL

- Extension of the proposed model to transient, non-saturated conditions. This would involve the solution of a multi-phase model for partially-saturated conditions.
- Inclusion of further potentials (e.g. lubrication and electrostatic forces) among the fibers. These mesoscopic potentials could be also fed via molecular dynamics (e.g. REAX potentials for curing [103]).
- Application of model order reduction techniques to the sub-grid scale equation, in conjunction with the use of GPU computing.
- Generalization of the numerical model developed for different applications in mesoscopic material modeling.

UNIFIED CFD APPROACH

Taking into account the possible future developments, the models have been thought for their implementation into the commercial CFD solver ANSYS Fluent. In this sense, the following procedure is suggested as a first approximation towards a unified framework for the analysis:

1. compaction of the yarn with the model proposed in Chapter 4;
2. extraction of the final compressed geometry of the yarn as a new fluid zone;
3. switch the solver to single-phase model and disable dynamic mesh;
4. define the newly created zone as porous and use the model proposed in Chapter 6;
5. apply a pressure drop and compute the permeability.

Some of the advantages of this methodology are that: (i) the mesh is unique, Cartesian and very simple; (ii) the computational cost is negligible; (iii) several test cases and configurations can be easily analyzed; (iv) the numerical framework is ready for the extension to 3D geometries.

7.2 Conclusiones y trabajo futuro (Español)

Muchas de las incertidumbres sobre la predicción numérica de la permeabilidad de tejidos para materiales compuestos reforzados en fibra, están relacionadas con las deformaciones que dichos tejidos experimentan durante el proceso de producción, es decir: la compactación en el molde (i) y la inyección de la resina (ii). Las dificultades en el desarrollo de modelos numéricos aptos para tener en cuenta estas deformaciones, están relacionadas con la estructura jerárquica de la tela, que requiere técnicas de modelado no estándar. El desarrollo de nuevos modelos numéricos para tener en cuenta el efecto de estas deformaciones sobre la permeabilidad ha sido el objeto de esta tesis.

La respuesta mecánica de la tela durante la compactación en el molde (i), ha sido estudiada mediante un modelo fenomenológico, en el cual las hebras se han modelado como sólidos blandos viscoplásticos, en la base de una analogía entre el conjunto de fibras y materiales granulares. El modelo multi-fase resultante ha sido resuelto numéricamente usando el software comercial de CFD ANSYS Fluent.

La deformación de la tela y su interacción con la resina durante la inyección (ii), ha sido estudiada mediante un modelo mesoscópico que tiene en cuenta la interacción fluido-estructura a nivel de fibra. Un método numérico acoplado se ha desarrollado para la solución numérica, que consiste en el método de volúmenes finitos para las ecuaciones del flujo fluido (en ANSYS Fluent) y un método de lattice Boltzmann para la dinámica de las fibras (acelerado en GPU a través de una implementación adaptada).

En base a los resultados obtenidos, se derivan las siguientes conclusiones principales:

1. el modelo desarrollado para la compactación en el molde resulta apto para un estudio fenomenológico de la deformación de las hebras bajo compactación. Dicho modelo permite analizar cuantitativamente la evolución de la fracción de fibra, lo cual proporciona información útil para la mejora de la comprensión de la distribución de las fibras antes de la inyección de la resina.
2. La analogía propuesta entre el conjunto de fibras y materiales granulares proporciona la posibilidad de desarrollar modelos constitutivos avanzados para las hebras (y finalmente para la tela). Dichos modelos constitutivos se pueden luego resolver eficientemente con

herramientas de fluidodinámica computacional, para estudiar la topología de las fibras que resulta de la compresión y finalmente su efecto sobre la permeabilidad.

3. el modelo desarrollado para la dinámica de las fibras durante la inyección, permite analizar la topología de las mismas inducida por el flujo. La permeabilidad de las fibras ha sido caracterizada a través de un invariante topológico en lugar de parámetros geométricos, lo cual constituye el punto fundamental del análisis. El coste computacional del modelo mesoscópico ha sido reducido significativamente gracias al modelo numérico acoplado que se ha desarrollado.

4. Se ha visto que el agrupamiento de fibras durante la inyección reduce significativamente la permeabilidad efectiva a nivel de hebra en medios fibrosos jerárquicos, lo cual podría explicar la sobrestimación que se obtiene con modelos numéricos simplificados. En este sentido, los diagramas de fase obtenidos para la permeabilidad permiten identificar las condiciones operativas mejores para la infiltración de la resina.

5. Los modelos propuestos han sido desarrollados usando técnicas no convencionales de fluidodinámica computacional, lo cual permitiría en un futuro utilizar entornos unificados para el análisis del proceso y finalmente una estimación más precisa de la permeabilidad. El actual trabajo constituye así una primera aproximación en esta dirección.

Con vistas a un posible ulterior desarrollo de los modelos propuestos se sugieren las siguientes mejoras:

MODELO DE COMPACTACIÓN DE LAS HEBRAS

- Adopción de una reología viscométrica [98, 101] para las hebras en el régimen quasi-estático de compresión que permita incluir viscosidades normales, las cuales en este caso deben estar relacionadas con las fuerzas fuera de plano.
- Para tener en cuenta efectos temporales (como por ejemplo de relajación de las fibras o de histéresis) se podrían adoptar reologías viscoelásticas. En este sentido, una extensión para este caso del modelo propuesto en el capítulo 6 se podría considerar.
- Mejora del comportamiento de la interface añadiendo información multi-escala a través de modelos phase-field [102].
- Ulterior desarrollo sobre la topología de las fibras (es decir, el agrupamiento), lo cual se ha visto en esta tesis afecta significativamente la conductividad hidráulica de las hebras durante la inyección de la resina.

MODELO PARA LA DINÁMICA DE LAS FIBRAS

- Extensión del modelo propuesto para condiciones transitorias no saturadas. Esto conllevaría la solución de un modelo multi-fase para condiciones parcialmente saturadas.
- Inclusión de potenciales mesoscópicos adicionales entre las fibras (como por ejemplo de lubricación y de fuerzas electrostáticas). Estos potenciales se podrían alimentar con simulaciones de dinámica molecular (por ejemplo, potenciales REAX para el curado [103]).
- Aplicación de técnicas de reducción de orden a la ecuación de sub-malla, en conjunción con la utilización de GPUs.
- Generalización del modelo numérico desarrollado en diferentes aplicaciones de modelos mesoscópicos de materiales.

ENTORNO UNIFICADO DE CFD

Teniendo en cuenta los posibles desarrollos futuros, los modelos propuestos han sido pensados para una implementación basada en el código comercial de CFD ANSYS Fluent. En este sentido, el siguiente procedimiento es sugerido como primera aproximación hacia un entorno unificado para el análisis:

1. compactación de la hebra con el modelo propuesto en el capítulo 4;
2. extracción de la geometría final de la hebra como una nueva zona fluída;
3. cambiar el solutor para mono-fase y deshabilitar la malla dinámica;
4. definir la nueva zona como porosa y usar el modelo propuesto en el capítulo 6;
5. aplicar un gradiente de presión y calcular la permeabilidad.

Algunas de las ventajas que esta metodología proporciona son que: (i) la malla es única, Cartesiana y muy sencilla; (ii) el coste computacional es muy bajo; (iii) se podrían analizar de forma muy sencilla varios casos test y configuraciones; (iv) el entorno numérico es adecuado para la extensión a geometrías 3D.

Appendix A

GPU implementations

In this section we present and discuss the methodology that progressively led us to the faster implementation for Graphic Processing Unit (GPU). Going into the details of coding goes beyond the purpose of the present work, therefore we provide a methodological description for each strategy. A slightly more detailed description is given for the faster implementation achieved. The available GPU is an NVIDIA© Quadro 600 1GB DRAM DDR3 96 cores and all the tests are performed in single-precision floating point operations. The CPU for the comparisons is an Intel© Xeon© X5650 2.67 GHz.

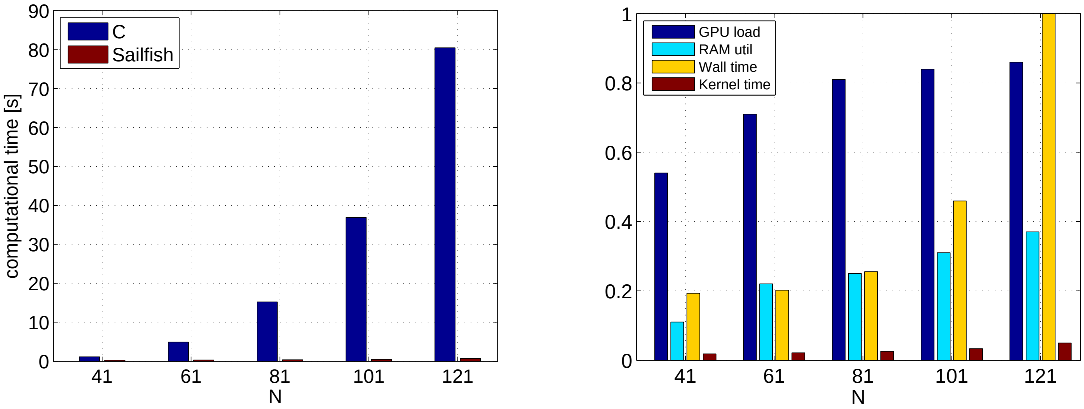

(a)

(b)

Figure A.1: Comparison of the computational time for compiled a compiled C code and SAILFISH (D2Q9 lattice with $\tau = 0.55$) on the available hardware (a) and GPU profiling for the coupling (normalized quantities).

A.1 *Sailfish* implementation

Sailfish is an open-source code for computational fluid dynamics based on lattice Boltzmann method and optimized for NVIDIA© graphic cards [104]. The structure of the code is non-trivial as it makes use of different scripting languages. The highest level code is Python, where the simulation parameters are set-up (mesh size, methods, initial and boundary conditions). The code generation passes then through *Mako* templates, which generate CUDA C or OpenCL optimized code. The generated code is then compiled on-the-fly and the resulting binary is run on graphic card. The code in its current version (0.3) is primarily designed to solve Navier-Stokes equations, however small changes in the lowest-level kernels allow us to tailor it for our purposes, that is, to solve an advection-diffusion equation. The speed-up achieved with respect to the CPU reaches nearly 60x (see Fig. A.1(a)).

The coupling with Fluent® is realized by means of serial dynamical calls to *Sailfish* from a compiled user defined function (written in C). Despite the simplicity of implementation, this approach has proven not to be computationally efficient, due to the time required by *Sailfish* for the GPU code generation and compilation for each call. The total time (or *wall time*) for a single call is indeed significantly higher than the effective computational time on the GPU cores (*kernel time*). A profiling of the timing and of the GPU utilization is reported in Fig. A.1(b). We conclude that *Sailfish* in its current version cannot be straightforwardly exploited for our purposes and an *ad-hoc* implementation for GPU has to be developed.

A.2 Texture memory implementation

The Compute Unified Device Architecture (CUDA) is a parallel computing platform and coding environment developed by NVIDIA© [100], which enables to exploit the power of graphic processing units for scientific applications (GPGPU). A GPU-oriented implementation for CUDA-enabled cards can be all the way written in C or C++, taking advantage of the language extensions (API) provided (see the CUDA Programming Guide [105]).

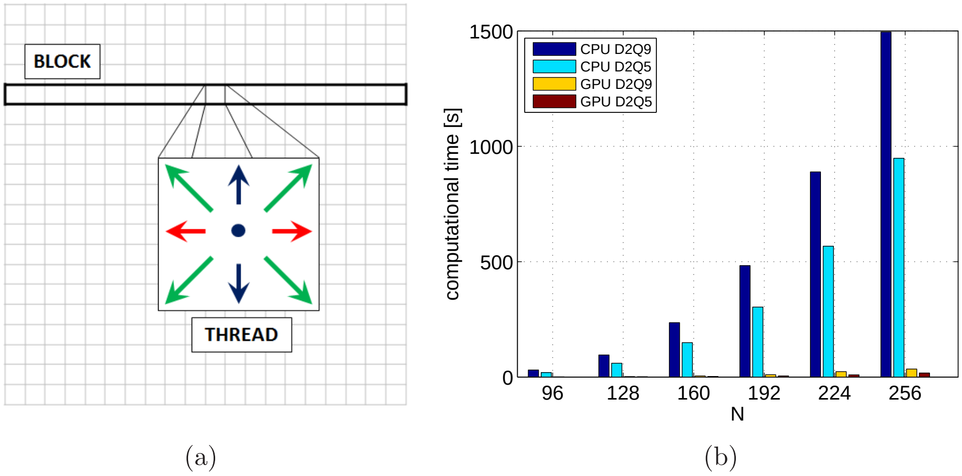

(a) (b)

Figure A.2: Scheme of the CUDA implementation using shared memory (a) and comparison of the computational time for compiled C and the CUDA implementation using shared memory (D2Q9 and D2Q5 lattices with $\tau = 0.55$) (b).

The general layout of a code, comprises a *host function* running on CPU and *kernel functions* running on the GPU. The kernels therefore take advantage of the parallelization on the graphic card. Due to the large computing power, the bottleneck resides in the memory read/write operations. As a general rule, a proper implementation should then reduce memory accesses as much as possible and/or use faster memories available on the graphic card. In this implementation for example we use *texture memory*, which is a read-only memory that is spatially cached, making faster the data retrieval in the device memory [105].

The implementation relies on two kernels, one for the collision step and one for the streaming. The mesh is hierarchically divided into grid, blocks and threads. Typically each node is assigned a thread, which is then handled by a processor. Data is allocated and passed from the CPU to the GPU and vice-versa, respectively at the beginning and at the end of the solution process. The data exchange between the two kernels is optimized using textures, however this data passage represent a bottleneck in the code. By means of this approach, indeed, the maximum speed-up achieved is around 25x with respect to the CPU.

Table A.1: Comparison of the computational time [s] for a compiled C code and the CUDA code (shared memory implementation).

N	96	128	160	192	224	256
D2Q9 CPU	30.4	95.5	235.8	483.0	889.0	1495.0
D2Q9 GPU	0.8	2.0	4.7	10.1	23.3	34.7
speed-up	38x	48x	50x	48x	38x	43x
D2Q5 CPU	19.0	60.0	149.0	303.5	567	948
D2Q5 GPU	0.4	1.3	2.5	5.0	9.6	7.1
speed-up	48x	46x	60x	60x	60x	55x

A.3 Shared memory implementation

In order to overcome the limit of the previous code, in this version we make use of *shared memory*, an extremely fast on-chip memory. The main issues to take into account for the implementation of a lattice Boltzmann method, is that it is of limited size (for our card is 48 KB), and that the data is shared only between threads belonging to the same block. A proper implementation of a lattice Boltzmann method using shared memory was originally proposed by Tölke [106]. We also refer the reader to [107] for more details on the hardware and for code excerpts.

Here we propose a similar strategy, but tailored for small meshes (our case). The code relies on a single kernel for collision and propagation and the mesh is processed by rows; therefore each block corresponds to one mesh row and the number of threads to the mesh width Fig. A.2(a). In this way the size of the data loaded into shared memory per block is limited to that required to process one row. Collision and propagation are then performed on shared memory, where the horizontal propagation of the distributions is straightforward within the block, while the vertical one is achieved with a correct alignment between global and shared memory. The coalescence of global memory accesses and the lack of bank conflicts on shared memory has been checked using the CUDA visual profiler [108] (we do not go into the details of these issues, the interested reader can refer to the CUDA Programming Guide [105]).

It is important to remark that this implementation is tailored for small meshes and does not apply in other cases. Fixing the block size equal to the mesh width indeed, sets a constraint on the choice of the number of threads (which plays a key-role for performance). This approach represents a tentative to properly exploit the GPU for small meshes, which is not normally done, but relevant for our application. With this implementation the speed-up reaches nearly 60x with respect to the CPU, as shown in Fig. A.2(b) and Table A.1.

The developed code is finally compiled with the CUDA compiler (nvcc) and dynamically called from a Fluent® user defined function. The sub-grid simulation is driven by passage and retrieval of the required variables between the two compiled codes through a stream process.

Appendix B

Thesis contributions

The following scientific contributions have been accomplished on the basis of this work:

Journal publications

4. L. Bergamasco, S. Izquierdo, M. Laspalas, M.A. Jiménez, *Analysis of multi-scale effects on the permeability of textile reinforcements for liquid composite molding*, Composites Part A: Applied Science and Manufacturing, *almost completed*;

3. L. Bergamasco, S. Izquierdo, I. Pagonabarraga, N. Fueyo, *Multi-scale permeability of deformable fibrous porous media*, Physical Review E: Statistical, Non-linear and Soft Matter Physics, *submitted to journal*;

2. L. Bergamasco, S. Izquierdo, E. Duvivier, J.M. Royo, A. Chiminelli, M.A. Jiménez, *Generalized analytical solution for compressive forces in adhesively-bonded-joint assembling*, International Journal of Adhesion & Adhesives, 52 (2014) 26–30;

1. L. Bergamasco, S. Izquierdo, A. Ammar, *Direct numerical simulation of complex viscoelastic flows via fast lattice-Boltzmann solution of the Fokker-Planck equation*, Journal of Non-Newtonian Fluid Mechanics, 201 (2013) 29-38;

Conference Proceedings

2. M. Laspalas, M. Lizaranzu, M. Castrillón, A. Gimeno, S. Izquierdo, L. Bergamasco, F. Martín de la Escalera, J.R. Sainz de Aja, M.A. Jiménez, *Input data determination for RTM simulation of composite materials*, Proceedings of the 16th European Conference on Composite Materials (ECCM16), Seville (Spain), Jun 2014.
1. L. Bergamasco, S. Izquierdo, M.A. Jiménez, *RTM permeability prediction using CFD and a GPU acceleration of a lattice Boltzmann solution for sub-grid probability density functions*, Proceedings of the 20th European Congress on Computational Methods in Applied Sciences and Engineering (ECCOMAS), Vienna (Austria), Sep 2012;

Workshop/Conference talks

3. L. Bergamasco, S. Izquierdo, M. Laspalas, M.A. Jiménez, *Analysis of multi-scale effects on the permeability of textile reinforcements for liquid composite molding*, 12th International Conference on Flow Processing in Composite Materials (FPCM12), Enschede (Netherlands), Jul 2014.
2. L. Bergamasco, S. Izquierdo, M.A. Jiménez, *RTM permeability prediction using CFD and a GPU acceleration of a lattice Boltzmann solution for sub-grid probability density functions*, 20th European Congress on Computational Methods in Applied Sciences and Engineering (ECCOMAS), Vienna (Austria), Sep 2012;
1. L. Bergamasco, S. Izquierdo, M.A. Jiménez, *Lattice Boltzmann solution of FENE kinetic equations for polymeric fluids*, Maths & Chemistry Workshop, Zaragoza (Spain), Jun 2012;

References

[1] MicroView Software, 2014. URL http://microview.sourceforge.net/. xvii, 14

[2] R. A. Saunders, C. Lekakou, and M. G. Bader. Compression in the processing of polymer composites 1. A mechanical and microstructural study for different glass fabrics and resins. *Comp. Sci. Technol.*, 59(7):983 – 993, 1999. xviii, 37

[3] C. Chauvière and A. Lozinski. Simulation of complex viscoelastic flows using the Fokker-Planck equation: 3D FENE model. *J. Non-Newt. Fluid Mech.*, 122(1-3):201–214, 2004. xix, xxi, 46, 57, 61, 62, 63

[4] C. D. Rudd, A. C. Long, K. N. Kendall, and C. Mangin. *Liquid Moulding Technologies: Resin Transfer Moulding, Structural Reaction Injection Moulding and Related Processing Techniques*. Woodhead Publishing, 1st edition, 1997. 1

[5] K. Potter. *Resin Transfer Moulding*. Springer, 1st edition, 1997. 1

[6] T. S. Mesogitis, A. A. Skordos, and A. C. Long. Uncertainty in the manufacturing of fibrous thermosetting composites: A review. *Composites Part A*, 57(0):67 – 75, 2014. 2

[7] PAM-RTM | ESI group - virtual product engineering software and services, 2014. URL https://www.esi-group.com/software-services/virtual-manufacturing/. 2

[8] PolyWorx Software, 2014. URL http://www.polyworx.com/. 2

[9] LIMS Software, 2014. URL http://www.ccm.udel.edu/Tech/LIMS/. 2

[10] R. Arbter, J. M. Beraud, C. Binetruy, L. Bizet, J. Brard, S. Comas-Cardona, C. Demaria, A. Endruweit, P. Ermanni, F. Gommer, S. Hasanovic, P. Henrat, F. Klunker, B. Laine, S. Lavanchy, S. V. Lomov, A. Long, V. Michaud, G. Morren, E. Ruiz, H. Sol, F. Trochu, B. Verleye, M. Wietgrefe, W. Wu, and G. Ziegmann. Experimental determination of the

permeability of textiles: A benchmark exercise. *Composites Part A*, 42(9):1157 – 1168, 2011. 2, 20

[11] N. Vernet, E. Ruiz, S. Advani, J. B. Alms, M. Aubert, M. Barburski, B. Barari, J. M. Beraud, D. C. Berg, N. Correia, M. Danzi, T. Delavire, M. Dickert, C. Di Fratta, A. Endruweit, P. Ermanni, G. Francucci, J. A. Garcia, A. George, C. Hahn, F. Klunker, S. V. Lomov, A. Long, B. Louis, J. Maldonado, R. Meier, V. Michaud, H. Perrin, K. Pillai, E. Rodriguez, F. Trochu, S. Verheyden, M. Weitgrefe, W. Xiong, S. Zaremba, and G. Ziegmann. Experimental determination of the permeability of engineering textiles: Benchmark II. *Composites Part A*, 61(0):172 – 184, 2014. 3, 20, 21, 35

[12] A. Hunt, R. Ewing, and B. Ghanbarian. *Percolation Theory for Flow in Porous Media*. Springer, 3rd edition, 2014. 3, 70, 72

[13] B. T. Åström, R. B. Pipes, and S. G. Advani. On flow through aligned fiber beds and its application to composites processing. *J. Compos. Mater.*, 26(9):1351–1373, 1992. 3, 70

[14] K. Yazdchi and S. Luding. Towards unified drag laws for inertial flow through fibrous materials. *Chem. Eng. J.*, 207208(0):35 – 48, 2012. 3, 70

[15] TexGen Software, 2014. URL `http://texgen.sourceforge.net/`. 4, 15

[16] T. M. Kruckenberg. The use of vibration in compaction and resin infiltration of composities. *PhD Thesis*, 2005. University of Sydney. 5, 21

[17] WiseTex Suit, 2014. URL `http://www.mtm.kuleuven.be/Onderzoek/Composites/`. 5, 15

[18] B. Verleye, R. Croce, M. Griebel, M. Klitz, S.V. Lomov, G. Morren, H. Sol, I. Verpoest, and D. Roose. Permeability of textile reinforcements: Simulation, influence of shear and validation. *Comp. Sci. Technol.*, 68(13):2804 – 2810, 2008. 5

[19] B. Verleye, S.V. Lomov, A. Long, I. Verpoest, and D. Roose. Permeability prediction for the meso–macro coupling in the simulation of the impregnation stage of Resin Transfer Moulding. *Composites Part A*, 41(1):29 – 35, 2010. 5

[20] S. Yip and M. P. Short. Multiscale materials modelling at the mesoscale. *Nat. Mater.*, 12(9):774–777, 2013. 6

[21] J. T. Padding, L.V. Mohite, D. Auhl, W. J. Briels, and C. Bailly. Mesoscale modeling of the rheology of pressure sensitive adhesives through inclusion of transient forces. *Soft Matter*, 7:5036–5046, 2011. 6

[22] G. Morren, S. Bossuyt, and H. Sol. 2D permeability tensor identification of fibrous reinforcements for RTM using an inverse method. *Composites Part A*, 39(9):1530 – 1536, 2008. 11

[23] B. R. Gebart. Permeability of unidirectional reinforcements for RTM. *J. Compos. Mater.*, 26(8):1100–1133, 1992. 17, 21, 70

[24] C. Demaría, E. Ruiz, and F. Trochu. In-plane anisotropic permeability characterization of deformed woven fabrics by unidirectional injection. part i: Experimental results. *Polym. Composite.*, 28(6):797–811, 2007. 17, 18

[25] G. Francucci, E. S. Rodríguez, and A. Vázquez. Study of saturated and unsaturated permeability in natural fiber fabrics. *Composites Part A*, 41(1):16 – 21, 2010. 20

[26] A. Shojaei, F. Trochu, S. R. Ghaffarian, S. M. H. Karimian, and L. Lessard. An experimental study of saturated and unsaturated permeabilities in resin transfer molding based on unidirectional flow measurements. *J. Reinf. Plast. Comp.*, 23(14):1515–1536, 2004. 20

[27] Y. Luo, I. Verpoest, K. Hoes, M. Vanheule, H. Sol, and A. Cardon. Permeability measurement of textile reinforcements with several test fluids. *Composites Part A*, 32(10): 1497 – 1504, 2001. 20

[28] A. Tamayol and M. Bahrami. Analytical determination of viscous permeability of fibrous porous media. *Int. J. Heat Mass Transfer*, 52(910):2407 – 2414, 2009. 21

[29] A. Tamayol and M. Bahrami. Parallel flow through ordered fibers: An analytical approach. *J. Fluids Eng.*, 132(11):114502, 2010. 21

[30] MTS Group Homepage, 2014. URL `http://www.mts.com/en/index.htm`. 24, 37

[31] MTS TestWorks Software. URL `http://www.mts.com/en/products/`. 24

[32] J. Engmann, C. Servais, and A. S. Burbidge. Squeeze flow theory and applications to rheometry: A review. *J. Non-Newt. Fluid Mech.*, 132(13):1 – 27, 2005. 25

[33] J. D. Sherwood and D. Durban. Squeeze-flow of a Herschel-Bulkley fluid. *J. Non-Newt. Fluid Mech.*, 77(12):115 – 121, 1998. 25

[34] G. Meeten. Constant-force squeeze flow of soft solids. *Rheol. Acta*, 41(6):557–566, 2002. 25, 27

[35] M. J. Adams, B. Edmondson, D. G. Caughey, and R. Yahya. An experimental and theoretical study of the squeeze-film deformation and flow of elastoplastic fluids. *J. Non-Newt. Fluid Mech.*, 51(1):61 – 78, 1994. 25

[36] J. D. Sherwood and D. Durban. Squeeze flow of a power-law viscoplastic solid. *J. Non-Newt. Fluid Mech.*, 62(1):35 – 54, 1996. 27

[37] GURIT Website. URL `http://www.gurit.com/`. 28

[38] S. Izquierdo, J. R. Valdés, M. Martínez, M. Accolti, S. Woudberg, P. Asinari, M. Miana, and J. P. Du Plessis. Porous-layer model for laminar liquid flow in rough microchannels. *Microfluid. Nanofluid.*, 9(6):1063–1075, 2010. 34

[39] X. Chen. *Modelling and Predicting Textile Behaviour.* Woodhead Publishing, 1st edition, 2009. 35

[40] P. A. Kelly, R. Umer, and S. Bickerton. Viscoelastic response of dry and wet fibrous materials during infusion processes. *Composites Part A*, 37(6):868 – 873, 2006. 35

[41] C. M. Van Wyk. Note on the compressibility of wool. *J. Text. Inst.*, 37(12):T285–T292, 1946. 35

[42] T. Kruckenburg and R. Paton. Compaction of dry and lubricated reinforcements. *Proceedings of FPCM7 Conference*, page 425, 2004. 35

[43] N. Pearce and J. Summerscales. The compressibility of a reinforcement fabric. *Compos. Manuf.*, 6(1):15–21, 1995. 35

[44] Y. Luo and I. Verpoest. Compressibility and relaxation of a new sandwich textile preform for liquid composite molding. *Polym. Composite.*, 20(2):179–191, 1999. 35

[45] Q. T. Nguyen, E. Vidal-Sall, P. Boisse, C. H. Park, A. Saouab, J. Brard, and G. Hivet. Mesoscopic scale analyses of textile composite reinforcement compaction. *Composites Part B*, 44(1):231 – 241, 2013. 35

[46] N. Moustaghfir, S. El-Ghezal Jeguirim, D. Durville, S. Fontaine, and C. Wagner-Kocher. Transverse compression behavior of textile rovings: finite element simulation and experimental study. *J. Mater. Sci.*, 48(1):462–472, 2013. 36

[47] C. Barbier, R. Dendievel, and D. Rodney. Numerical study of 3D-compressions of entangled materials. *Comp. Mater. Sci.*, 45(3):593 – 596, 2009. 36

[48] B. Chen and T.-W. Chou. Compaction of woven-fabric preforms in liquid composite molding processes: single-layer deformation. *Compos. Sci. Technol*, 59(10):1519 – 1526, 1999. 36, 39, 40

[49] Z.-R. Chen and L. Ye. A micromechanical compaction model for woven fabric preforms. Part II: Multilayer. *Comp. Sci. Technol.*, 66(16):3263 – 3272, 2006. 36

[50] P. Boisse. *Composite Reinforcements for Optimum Performance*. Woodhead Publishing, 1st edition, 2011. 38

[51] R. A. Saunders, C. Lekakou, and M. G. Bader. Compression and microstructure of fibre plain woven cloths in the processing of polymer composites. *Composites Part A*, 29(4): 443 – 454, 1998. 39

[52] R. G. Owens and T. N. Phillips. *Computational Rheology*. Imperial College Press, 2002. 45, 48, 61

[53] R. B. Bird, R. C. Armstrong, and O. Hassager. *Dynamics of Polymeric Liquids Vol. 1 (Fluid Mechanics)*. Wiley-Interscience, 1987. 45

[54] R. B. Bird, C. F. Curtiss, R. C. Armstrong, and O. Hassager. *Dynamics of Polymeric Liquids Vol. 2 (Kinetic Theory)*. Wiley-Interscience, 1987. 45, 50

[55] R. Keunings. Micro-macro methods for the multiscale simulation of viscoelastic flow using molecular models of kinetic theory. *Rheology Reviews (British Society of Rheology)*, pages 67–98, 2004. 45, 46

[56] M. Laso and H. C. Öttinger. Calculation of viscoelastic flow using molecular models: the CONNFFESSIT approach. *J. Non-Newt. Fluid Mech.*, 47(0):1–20, 1993. 45

[57] B. Jourdain, C. Le Bris, and T. Lelièvre. On a variance reduction technique for micro-macro simulations of polymeric fluids. *J. Non-Newt. Fluid Mech.*, 122(1-3):91–106, 2004. 45

[58] M. A. Hulsen, A. P. G. van Heel, and B. H. A. A. van den Brule. Simulation of viscoelastic flows using Brownian configuration fields. *J. Non-Newt. Fluid Mech.*, 70(1-2):79–101, 1997. 46

[59] A. Lozinski and C. Chauvière. A fast solver for Fokker-Planck equation applied to viscoelastic flows calculations: 2D FENE model. *J. Comp. Phys.*, 189(2):607–625, 2003. 46, 49

[60] D. Moroni, B. Rotenberg, J. P. Hansen, S. Succi, and S. Melchionna. Solving the Fokker-Planck kinetic equation on a lattice. *Phys. Rev. E*, 73:066707, 2006. 46

[61] A. Ammar, B. Mokdad, F. Chinesta, and R. Keunings. A new family of solvers for some classes of multidimensional partial differential equations encountered in kinetic theory modeling of complex fluids. *J. Non-Newt. Fluid Mech.*, 139(3):153 – 176, 2006. 46

[62] D. J. Knezevic and A. T. Patera. A certified reduced basis method for the Fokker–Planck equation of dilute polymeric fluids: FENE dumbbells in extensional flow. *SIAM J. Scientific Computing*, 32(2):793–817, 2010. 46

[63] A. Ammar. Lattice Boltzmann method for polymer kinetic theory. *J. Non-Newt. Fluid Mech.*, 165(19-20):1082–1092, 2010. 46, 53, 58, 60

[64] F. Wu, W. Shi, and F. Liu. A lattice Boltzmann model for the Fokker-Planck equation. *Commun. Nonlinear Sci. Numer. Simul.*, 17(7):2776 – 2790, 2012. 46

[65] A. Majumder, V. Kariwala, S. Ansumali, and A. Rajendran. Lattice Boltzmann method for multi-dimensional population balance models in crystallization. *Chem. Eng. Sci.*, 70 (0):121 – 134, 2012. 46

[66] S. Singh, G. Subramanian, and S. Ansumali. A lattice Boltzmann method for dilute polymer solutions. *Philos. T. Roy. A*, 369(1944):2301–2310, 2011. 46, 60, 69

[67] T. Li. Mathematical analysis of multi-scale models of complex fluids. *Commun. Math. Sci.*, 5(1):1–51, 2007. 48

[68] A. Onuki. *Phase Transition Dynamics.* Cambridge University Press, 1st edition, 2002. 48

[69] H. R. Warner. Kinetic theory and rheology of dilute suspensions of finitely extendible dumbbells. *Ind. Eng. Chem. Fund.*, 11(3):379–387, 1972. 48

[70] J. Barrett and E. Süli. Existence of global weak solutions to some regularized kinetic models for dilute polymers. *Multiscale Model. Simul.*, 6(2):506–546, 2007. 49

[71] R. O. Vargas, O. Manero, and T. N. Phillips. Viscoelastic flow past confined objects using a micro-macro approach. *Rheol. Acta*, 48:373–395, 2009. 51, 61

[72] H. Versteeg and W. Malalasekra. *An Introduction to Computational Fluid Dynamics: The Finite Volume Method Approach.* Prentice Hall, 1996. 52

[73] S. Succi. *The Lattice Boltzmann Equation for Fluid Dynamics and Beyond.* Oxford University Press, 2001. 52

[74] S. Chen and G. D. Doolen. Lattice Boltzmann method for fluid flows. *Annu. Rev. Fluid Mech.*, 30(1):329–364, 1998. 53

[75] T. D. Papathanasiou. On the effective permeability of square arrays of permeable fiber tows. *Int. J. Multiph. Flow*, 23(1):81 – 92, 1997. 71

[76] T. D. Papathanasiou. Flow across structured fiber bundles: a dimensionless correlation. *Int. J. Multiph. Flow*, 27(8):1451 – 1461, 2001. 71

[77] B. Markicevic and T. D. Papathanasiou. On the apparent permeability of regular arrays of nonuniform fibers. *Phys. Fluids*, 14(9):3347–3349, 2002. 71

[78] T. D. Papathanasiou, E. M. Gravel, S. C. Barwick, and E. D. Dendy. Non-isotropic structured fibrous media: The permeability of arrays of fiber bundles of elliptical cross section. *Polym. Composite*, 23(4):520–529, 2002. 71

[79] A. Endruweit, F. Gommer, and A. C. Long. Stochastic analysis of fibre volume fraction and permeability in fibre bundles with random filament arrangement. *Composites Part A*, 49(0):109 – 118, 2013. 71

[80] P. Soltani, M. S. Johari, and M. Zarrebini. Effect of 3D fiber orientation on permeability of realistic fibrous porous networks. *Powder Technol.*, 254(0):44 – 56, 2014. 71

[81] X. Chen and T. D. Papathanasiou. The transverse permeability of disordered fiber arrays: a statistical correlation in terms of the mean nearest interfiber spacing. *Transport Porous Med.*, 71(2):233–251, 2008. 71

[82] K. Yazdchi, S. Srivastava, and S. Luding. Micro–macro relations for flow through random arrays of cylinders. *Composites Part A*, 43(11):2007 – 2020, 2012. 71

[83] K. Yazdchi, S. Srivastava, and S. Luding. Microstructural effects on the permeability of periodic fibrous porous media. *Int. J. Multiph. Flow*, 37(8):956 – 966, 2011. 71

[84] K. Yazdchi and S. Luding. Upscaling and microstructural analysis of the flow-structure relation perpendicular to random, parallel fiber arrays. *Chem. Eng. Sci.*, 98(0):173 – 185, 2013. 71

[85] C. Scholz, F. Wirner, J. Götz, U. Rüde, G. E. Schröder-Turk, K. Mecke, and C. Bechinger. Permeability of porous materials determined from the Euler characteristic. *Phys. Rev. Lett.*, 109:264504, 2012. 72, 76, 83

[86] K. Mecke and C. H. Arns. Fluids in porous media: a morphometric approach. *J. Phys.: Condens. Matter.*, 17(9):S503, 2005. 72

[87] F. A. Howes and S. Whitaker. The spatial averaging theorem revisited. *Chem. Eng. Sci.*, 40(8):1387 – 1392, 1985. 75

[88] S. Whitaker. Flow in porous media I: A theoretical derivation of Darcy's law. *Transport Porous Med.*, 1(1):3–25, 1986. 75

[89] J. A. Ochoa-Tapia and S. Whitaker. Momentum transfer at the boundary between a porous medium and a homogeneous fluid – I Theoretical development. *Int. J. Heat Mass Transfer*, 38:2635–2646, 1995. 75

[90] F. J. Valdés-Parada, B. Goyeau, and J. A. Ochoa-Tapia. Jump momentum boundary condition at a fluid-porous dividing surface: derivation of the closure problem. *Chem. Eng. Sci.*, 62:4025–4039, 2007. 75

[91] W.-P. Breugem. The effective viscosity of a channel-type porous medium. *Phys. Fluids*, 19(10):–, 2007. 76

[92] D. L. Marchisio and R. O. Fox. *Computational Models for Polydisperse Particulate and Multiphase Systems*. Cambridge University Press, 2013. 77

[93] A. T. Chwang and T. Y. Wu. Hydromechanics of low-Reynolds-number flow. Part 4. Translation of spheroids. *J. Fluid Mech.*, 75:677–689, 1976. 77, 79

[94] J. N. Israelachvili. *Intermolecular and Surface Forces.* Academic Press, 3rd edition, 2011. 78

[95] H. C. Öttinger. *Stochastic Processes in Polymeric Fluids.* Springer, 1996. 78

[96] W. Young, R. Budynas, and A. Sadegh. *Roark's Formulas for Stress and Strain.* McGraw-Hill Professional, 8th edition, 2011. 78

[97] P. Jop, Y. Forterre, and O. Pouliquen. A constitutive law for dense granular flows. *Nature*, 441(7094):727–730, 2006. 80, 88

[98] F. Boyer, É. Guazzelli, and O. Pouliquen. Unifying suspension and granular rheology. *Phys. Rev. Lett.*, 107:188301, 2011. 80, 88, 95, 98

[99] H. Bruus. *Theoretical Microfluidics.* Oxford University Press, USA, 2007. 83

[100] Nvidia Developer Zone, 2012. URL `https://developer.nvidia.com/`. 84, 101

[101] B. Andreotti, Y. Forterre, and O. Pouliquen. *Granular Media: Between Fluid and Solid.* Cambridge University Press, 1st edition, 2013. 95, 98

[102] K. Thornton, J. Ågren, and P. W. Voorhees. Modelling the evolution of phase boundaries in solids at the meso- and nano-scales. *Acta Mater.*, 51(19):5675 – 5710, 2003. 95, 98

[103] M. F. Russo Jr. and A. C. T. van Duin. Atomistic-scale simulations of chemical reactions: Bridging from quantum chemistry to engineering. *Nucl. Instr. Meth. Phys. B*, 269(14): 1549 – 1554, 2011. 95, 99

[104] Sailfish CFD, 2012. URL `http://sailfish.us.edu.pl/`. 101

[105] CUDA Downloads, 2012. URL `https://developer.nvidia.com/cuda-downloads`. 101, 102, 103

[106] J. Tölke. Implementation of a lattice Boltzmann kernel using the Compute Unified Device Architecture developed by nVIDIA. *Comput. Vis. Sci.*, 13(1):29–39, 2010. 103

[107] F. Kuznik, C. Obrecht, G. Rusaouen, and J. J. Roux. LBM based flow simulation using GPU computing processor. *Comput. Math. Appl.*, 59(7):2380–2392, 2010. 103

[108] CUDA Performance analysis and profiling tools: NVIDIA Visual Profiler, 2012. URL `https://developer.nvidia.com/nvidia-visual-profiler`. 103